Faculty of Engineering and Information Technology

An Investigation into the Roll Control of Vehicles with Hydraulically Interconnected Suspensions

A thesis submitted for the degree of

Doctor of Philosophy

Sangzhi Zhu

(2016)

Title of the thesis:
An Investigation into the Roll Control of Vehicles with Hydraulically Interconnected Suspensions

Ph.D. candidate:
Sangzhi Zhu
E-mail: [redacted]

Supervisor:
Prof Nong Zhang
E-mail: Nong.Zhang@uts.edu.au

Co-Supervisor:
Dr. Holger Roser
E-mail: Holger.Roser@uts.edu.au

Address:
School of Electrical, Mechanical and Mechatronic Systems
The University of Technology, Sydney, NSW 2007, Australia

Certificate of Original Authorship

I certify that the work in this thesis has not previously been submitted for a degree nor has it been submitted as part of requirements for a degree except as fully acknowledged within the text.

I also certify that the thesis has been written by me. Any help that I have received in my research work and the preparation of the thesis itself has been acknowledged. In addition, I certify that all information sources and literature used are indicated in the thesis.

Signed:

_____

Sangzhi Zhu

Acknowledgments

The following people have provided me with tremendous assistance, encouragement and support throughout my candidature and I would like to take the opportunity to express my gratitude towards them.

First and foremost, I am profoundly grateful to my supervisor, Professor Nong Zhang for his outstanding guidance, caring encouragement and patience throughout the duration of this project. His knowledge, hard-working and research attitude fostered my development in various aspects. I would also express my deep gratitude to Professor Haiping Du for his guidance and support on control theory over these years. I also would like to thank my co-supervisor, Dr Holger Roser, for his expertise and assistance regarding all the laboratory work, and for always being willing to bounce an idea around.

I would like to thank Dr Paul Walker and Dr Zhuojie Liang for all their help and insightful input. Dr Lifu Wang's assistance at the initial stage of this project and consistent support and guidance was a tremendous asset to the project, and I greatly appreciate his help. I deeply appreciate Guangzhong Xu and Anton Takachev for their assistance in setting up and conducting the experiments. The constructive arguments have been very useful. I also would like to thank Xinxin Shao for her help on the delay-dependent control algorithm. And I would like to thank all the capstone students that worked with me on this project: Matthias Wong, Quang Lam, Heip Pham, Tamas Bykerk. Without their hard work and help, I would not have been able to complete this project.

I also would like to thank my colleagues, Xingxing Zhou, Yu Wang, Jinglai Wu, Tianxiao Zhang, Jiageng Ruan, Li Sun, Bo Zhu, Yuhong Fang for their support, especially Jinglai's support on MATLAB.

I also wish to gratefully acknowledge the financial support of this work by the China Scholarship Council (CSC) and the University of Technology, Sydney (UTS).

Many thanks to my family, words cannot express what I owe them for their support and understanding over the years and whose consistent encouragement has quite literally sustained me throughout my endeavours.

Sangzhi Zhu

Sydney, January 2016

Publications and Conference Contributions

The following publications are part of the thesis

Peer reviewed international scientific journal publications

[1] **Zhu, S.,** Wang, L., Zhang, N., & Du, H., H∞ Control of a Novel Low-Cost Roll-Plane Active Hydraulically Interconnected Suspension: An Experimental Investigation of Roll Control under Ground Excitation. ***SAE International Journal of Passenger Cars-Mechanical Systems***, 6(2013-01-1238), 882-893, 2013.

[2] **Zhu, S.,** Du, H., Zhang, N., & Wang, L., Development of A New Model for Roll-Plane Active Hydraulically Interconnected Suspension. ***SAE International Journal of Passenger Cars-Mechanical Systems***, *7*(2014-01-0053), 447-457, 2014.

[3] **Zhu, S.,** Xu, G., Tkachev, A., Wang, L., & Zhang, N., Road Holding Ability Comparison of a Roll-Plane Hydraulically Interconnected Suspension and Anti-Roll Bars. ***Proceedings of the Institution of Mechanical Engineers, Part D: Journal of Automobile Engineering***, (Major revision, Manuscript ID JAUTO-15-0463).

[4] Liang, J., Wu, J., Zhang, N., Luo, Z. & **Zhu, S.,** Interval uncertain analysis of active hydraulically interconnected suspension system. ***Advances in Mechanical Engineering.*** 8(5), 2016: 1687814016646331.

Peer reviewed international scientific conference publications

[1] **Zhu, S.,** Du, H., & Zhang, N. (2014, July). Development and Implementation of Fuzzy, Fuzzy PID and LQR Controllers for a Roll-plane Active Hydraulically Interconnected Suspension. In *2014 IEEE International Conference on Fuzzy Systems (FUZZ-IEEE),* (pp. 2017-2024). IEEE.

[2] Zhang, N., **Zhu, S.** & Liang, J., (2015, November). Experimental Investigation of a Roll-plane Hydraulically Interconnected Suspension and Anti-roll Bars in Warp Mode. In *16th Asia Pacific Vibration Conference* (pp.566-570), Hanoi, Vietnam.

Abstract

This thesis presents the investigation into a roll-plane hydraulically interconnected suspension (HIS), which is safety-oriented and designed for the vehicle with a high centre of gravity (CG) and a low rollover threshold.

As a potential replacement of anti-roll bars, the HIS possesses the ability to resist the roll motion of the vehicle body during cornering or sharp turning by improving the vehicle roll stiffness. The previous research has concluded that the HIS is superior to the anti-roll bars in terms of the anti-roll performance, but its road holding performance has not been thoroughly studied. In this research, the modelling, modal analysis and simulations are conducted to compare the road holding ability of the HIS and anti-roll bars. A multi-function HIS test rig is developed and mounted on a typical Sports Utility Vehicle (SUV). The related experiments are implemented on a four-post test rig. Both the simulation and experiment results confirmed that the HIS is better than anti-roll bars from the perspective of the road holding performance.

To overcome the drawback of the HIS that it is unable to handle the large roll motion and the vehicle roll caused by uneven roads, the HIS is then developed to be actively controlled by a control unit. Only one servo valve is included in the control unit of the active HIS so that the system's cost and energy consumption are much lower in comparison with the conventional active suspensions with four independent motor-actuators. An output feedback H∞ controller is developed based on an empirically estimated active HIS model at a half-car level. The active HIS controlled by the designed H∞ controller is experimentally validated on the test rig with considerable roll angle reductions.

For further verifying the controllability of the active HIS and also comparing the effect of different categories of control methods on the active HIS, other three representative control algorithms are also applied to the active HIS equipped vehicle. They are the classic control methods: proportional-integral-derivative (PID) control, the optimal control algorithm: linear-quadratic regulator (LQR) control and the intelligent control algorithm: fuzzy logic control. The obtained fuzzy, fuzzy-PID and LQR controllers are implemented in simulations. The experiments of the fuzzy and fuzzy-PID controllers are also conducted. The fuzzy-PID controller presents the most promising and stable control performance among these three controllers.

After that, an attempt is made to improve the control performance of the model-based controllers to enhance the roll resistance ability of the active HIS further. A nine-degrees-of-freedom (nine-DOF) model that can capture the physical characteristics of the active HIS more accurately is developed. The new system model that addresses the relation between the flow change and pressure variation of the hydraulic system, and the viscous resistance of the fluid is also included. Then an H∞ controller and an LQR controller are designed based on the new model and validated in simulations. The experiment of the H∞ controller is also performed on the test rig and the H∞ controller derived from the new model is compared with the H∞ controller derived from the old model. The results show that the H∞ controller based on the new model improves the control performance slightly.

Lastly, an effort is made to reduce the effects of the time delay caused by the fluid system by considering the system time delay when developing the controller. Delay-independent and delay-dependent H∞ state feedback controllers are designed and applied to the half car

model. The simulation validations of the obtained controllers are carried out in MATLAB. It is found that the developed delay-dependent H∞ controller can provide stable and acceptably good control performance even with system time delay.

Keywords: Interconnected suspension, active suspension, vehicle handling, warp mode, roll mode, H∞ control.

Contents

List of Tables

List of Figures

Nomenclature

Global abbreviations used in this thesis

ADAMS	=	Automatic Dynamic Analysis of Mechanical Systems
ARE	=	Algebraic Riccati equation
ASCA	=	Active suspension via control arm
Bar	=	Unit of pressure equal to 100 kPa
CAD	=	Computer-aided design
CG	=	Centre of gravity
DDAS	=	Demand Dependent Active Suspension
DOF	=	Degrees of freedom
DRC	=	Dynamic Ride Control
ESP	=	Electronic Stability Program
HBMC	=	Hydraulic Body Motion Control Suspension
HIS	=	Hydraulically Interconnected Suspension
H∞	=	H infinity
LABView	=	Data logging and analysis software by National Instruments
LMI	=	Linear matrix inequality
LQR	=	Linear-quadratic regulator
LQG	=	Linear-quadratic-Gaussian

LVDT	=	Linear variable displacement transducer
MD	=	Medium
NI	=	National Instruments
NL	=	Negative large
NM	=	Negative medium
NS	=	Negative small
NVL	=	Negative very large
PID	=	Proportional-integral-derivative
PL	=	Positive large
PM	=	Positive medium
PS	=	Positive small
PVL	=	Positive very large
SUV	=	Sports utility vehicle
T-S	=	Takagi-Sugeno
UTS	=	University of Technology Sydney
ZS	=	Zero
3D	=	Three dimensional
4WDs	=	Four-wheel drive vehicles

1 Introduction

1.1 Overview of the research

Traffic safety is a worldwide problem that concerns public health and safety. Only about 3% of all crashes are rollovers, but they account for 33% of crash-related deaths [1]. There are 340 deaths, 6000 injuries caused directly by rollover accidents annually in Australia and many times those numbers internationally [2]. Generally, the vehicle roll stability can be improved by increasing the suspension roll stiffness and damping.

The vehicle suspension connecting the wheels of a vehicle to its body is pivotal to the isolation of ground excitations, prevention of vehicle roll, and maintenance of tire/ground contact. Conventional passive vehicle suspensions achieve the road-induced vibration isolation through passive means such as springs and dampers or shock absorbers. The parameters of passive suspensions are fixed and generally non-adjustable after production. Vehicle handling and ride comfort commonly have conflicting requirements on the suspension system design. For example, a stiffer suspension improves handling, whereas a softer suspension enhances ride comfort [3]. Therefore, a compromise is required for conventional passive suspensions.

One solution to overcoming the ride-handling compromise is the passive interconnected suspension, in which a displacement at one wheel station can produce forces at other wheel stations [4]. The hydraulically interconnected suspension (HIS) has been investigated intensively recently, and has been verified to be superior to anti-roll bars in the anti-roll

performance during cornering and sharp turning. However, by means of adding roll stiffness to the vehicle, neither the HIS nor anti-roll bars can handle the vehicle roll motion caused by ground excitations.

Active suspensions, typically with four independently controlled linear motors and numerous control objectives, can govern the vehicle body roll motion caused by both lateral accelerations and road excitations. However, although several active suspension systems are available in the market [5, 6], their applications are strictly limited to luxury vehicles, owing to high manufacturing cost and excessive energy consumption. Thus, an active suspension with low cost and energy consumption is required for vulnerable vehicles in rollover accidents.

In recent years, an active HIS, which evolved from the HIS system, possessing the advantages of low cost and low energy consumption, has been proposed by Zhang [7]. This thesis focuses on the HIS and active HIS systems. The investigation into the road holding ability of the HIS as a complement to the previous studies is presented firstly. Then the focus is concentrated on realising and improving the vehicle roll motion control with the active HIS.

1.2 Research objectives and contribution to knowledge

The specific objectives and contributions of this research are as follows.

1. To review the literature regarding various categories of vehicle suspension systems to show their advantages and disadvantages and the gaps in current knowledge; to introduce the HIS and active HIS; to briefly review the history of the control theories.

2. To validate that the HIS equipped vehicle performs better than the anti-roll bars equipped vehicle in the field of road holding ability through modal analysis, simulations and experiments.

3. To experimentally validate the feasibility of the proposed novel active HIS at the full-car level and apply different categories of control methods to the active HIS to improve the performance of the roll motion control.

4. To develop a more sophisticated system model including the pressure and flow of the hydraulic system for (1) more accurate description of the whole system of the active HIS equipped vehicle; (2) more reliable simulation study; (3) better roll control performance with the model-based control algorithms.

5. To validate the new model and the performance of the controller based on the new model.

6. To apply the delay-dependent control algorithm to reduce the negative effects of the system time delay.

1.3 Scope of thesis

1.3.1 Areas that are addressed

The following areas are within the scope of this thesis:

- the investigation into the road holding performance of the HIS
- the experimental validation of the active HIS in a real car application
- the application of control algorithms in the active HIS

- detailed modelling and the experimentation of model verification
- the application of model-based control methods in the new model
- delay-dependent state feedback H∞ control

1.3.2 Areas that are not addressed

The following areas are beyond the scope of this thesis:

- vehicle lateral dynamics
- the bounce and pitch motion control
- delay-dependent output feedback H∞ control
- a real car application of the delay-dependent control

1.4 Outline of thesis

The thesis will consist of eight chapters, organised as follows:

Chapter 2: some background information and a literature review on conventional suspensions and interconnected suspensions are presented in Chapter 2. The emphasis is laid on the hydraulic interconnection, active suspensions and control theories. The gaps in the current knowledge are revealed. The chapter also produces the conceptions of the HIS and active HIS.

Chapter 3: the road holding ability of the HIS and anti-roll bars are compared in Chapter 3. A full car vertical-dynamics vehicle model is provided. The anti-roll bar model and the HIS model are integrated with the vehicle model. The details of the modal analysis are presented. The simulations and experiments with warp and bump road excitations are conducted.

Chapter 4: the experimental validation of the active HIS is carried out in Chapter 4. A half car model is integrated with a simple active HIS model obtained in a previous study. Because of the use of a simple half-car model, both the mechanical and the fluid system models are linear. An output feedback H∞ controller is designed based on the obtained system model and applied on the active HIS. The experiments of the vehicle roll motion control are implemented on a four-post test rig.

Chapter 5: different categories of control methods are applied to the active HIS in Chapter 5. Fuzzy, fuzzy-PID and LQR controllers are developed. The simulations and their experimental verifications of the fuzzy and fuzzy-PID controllers are also conducted.

Chapter 6: a detailed modelling of the active HIS including pressure, flow and the fluid system damping are presented in Chapter 6 to improve the model accuracy. A series of simulations and tests are carried out for model verification. The responses of the old and new models in simulations are compared with the test results. Then the H∞ control is applied in the new model.

Chapter 7: an attempt is made to reduce the effects of the fluid system time delay in the vehicle roll motion control by the active HIS in Chapter 7. The delay-dependent H∞ control algorithm is applied. A state feedback controller is designed, and the simulations are carried out.

Chapter 8: this thesis is concluded in Chapter 8. The recommendations for further work are given, and the contributions are summarised.

2 Background and Literature Review

2.1 Introduction and rationale

This chapter introduces the background knowledge of the research in this thesis such as the development of vehicle suspensions and control theory. It begins with brief background information on vehicle suspensions. More detailed review of vehicle suspensions goes in two paths. The development history of interconnected suspensions gives rise to an introduction to the HIS system, and the summary of active suspensions brings on an introduction to the active HIS system. A brief literature review on the control theory and its applications to the active suspensions is then provided.

2.2 Vehicle suspension systems

The advent of suspension systems that are employed in horse-drawn vehicles in the form of leaf springs is far earlier than the appearance of the automobiles by 1886 [8]. After more than one century development, the most basic form of the most widely used modern suspensions comprises three fundamental elements, restoring and damping media and location of the wheels [9]. In general, this is realised by springs, which act against any relative displacement between the vehicle body and road wheels from some neutral position, and shock absorbers, which are used to dissipate the vibrational energy [10].

For a road vehicle, the suspension system serves mainly two purposes. One is to isolate the occupants or cargoes from severe levels of shock and vibration induced by the road surface. The other is to enable the wheels to maintain contact with the ground, assuring the stability

of the vehicle. However, apart from the basic requirements of the ride and handling performance, there are more factors that need to be considered by designers, such as the manufacturing cost, energy consumption, reliability, space and weight, noise generation and transmission [11].

The efforts made for achieving the complex objectives brought about the advancement of vehicle suspension systems in the last century. The earliest vehicle dynamics studies of suspension systems [12, 13] laid emphasis mainly on providing adequate ride performance, that is, the isolation of the vehicle body from excitation sources. After the 1950s, with growing attention to dynamic performance and safety, the handling and stability became major topics of investigation [14, 15]. However, the vehicle ride and handling performance commonly have conflicting requirements for suspension system design, so if one of them is improved, the other would be compromised.

For understanding the reason of the conflict between the ride and handling performance, the vehicle motion modes need to be investigated. There are seven main motion modes for the vibration of a four-wheel vehicle, and they can be divided into two categories. The one is the rigid body vehicle modes, which describes the motions of the vehicle body (sprung mass) relative to the ground, namely the body-dominated bounce, pitch and roll modes. The other category is called suspension modes, which describes the vertical motions of the road wheels (unsprung masses) relative to the sprung mass [16]. They are the wheel-dominated bounce, pitch, roll and warp modes.

Four of these motion modes, the body-dominated bounce, pitch and roll and the wheel-dominated warp, are the main concern of the vehicle ride and handling performance. It is noted that they are simply called bounce, roll, pitch and warp in this thesis. Bounce, pitch and roll are body-dominated motion modes that can be excited by steering, accelerating or braking, and ground disturbances, respectively. Warp occurs when only diagonally-opposed wheels move in phase relative to the vehicle body. However, different modes do not share the same preference concerning suspension stiffness and damping. For instance, relatively large roll and pitch stiffness is desired for inhibiting vehicle attitude during steering, braking, and acceleration, while relatively small bounce stiffness is beneficial for ride comfort. A soft warp mode is preferred to enhance vehicle road holding performance [9].

The parameters of the conventional passive suspensions are fixed and generally non-adjustable after production, and therefore a compromise has to be made. The conflicting requirements between the ride and handling have become the main challenge in the suspension design, and the two main trends to break this compromise are interconnected suspensions and active suspensions.

2.3 Interconnected Suspensions

An interconnected suspension system is one in which the force generated by the motion of one wheel station can be transmitted to the other stations. For a two-axle vehicle, the suspension interconnection can be realised by two-wheel interconnection or four-wheel interconnection. Interconnected suspensions can decouple different vehicle vibration modes easily in a passive manner through a wide variety of means, such as mechanical, hydraulic and pneumatic, or hydro-pneumatic.

2.3.1 Development of interconnected suspensions

The anti-roll bar is a most widely used interconnected mechanism currently, which increases vehicle roll stability by additional roll stiffness through connecting left and right wheel pairs mechanically. However, along with the increased roll stability, the warp mode is also unfavourably stiffened, and the ride performance is also compromised by the increased stiffness in single-wheel [17].

More sophisticated interconnected suspensions with good comprehensive performance have been pursued for almost a century since the early proposed concept [18]. In the 1920s, conceptions of roll- and pitch-plane hydraulic interconnection arrangements were proposed, but fluid system transmission characteristics were not considered in the research. In 1949, a pitch-plane interconnected arrangement was realised on the Citroën 2CV [19], which is the first application of mechanically interconnected suspension in the mass production of a vehicle.

In the 1950s to 1970s, the Hydragas system introduced by Moulton [20, 21] attracted researchers' attention because compact vehicles that have higher pitch frequencies were increasingly used. An experimental study was done by Moulton. In his study, a simplified model was provided, but no model validation and simulation were given. A passive hydraulically interconnected suspension system for increasing roll stiffness was studied by simulations in the middle 1990s [22, 23]. The results suggested that the roll-plane interconnected suspension can increase the roll stiffness and improve the ride performance of the vehicle simultaneously.

However, the above-presented interconnected suspensions were based on two-wheel interconnections, and they inevitably increased the stiffness of two suspension modes. Hence, to fully decouple the vehicle motion modes, some efforts were made for the interconnection suspensions with four wheel stations interconnected recently [24, 25].

A four-wheel interconnection arrangement was presented for full modal decoupling in the late 1990s [26], but it was only on the conceptual level, and there was no theoretical or experimental study provided. Another interconnected suspension that achieved full modal decoupling with springing was proposed by the year 2000 [27, 28], but the damping decoupling was not discussed. Smith [4] studied a new concept for complete modal decoupling, but the actual vehicle system dynamics was not investigated. Mavroudakis [29] proposed a four-wheel interconnection based hydraulic scheme what is fully decoupled and controlled by a central unit. The simulation illustrated the interconnected suspension out-performed the conventional suspension easily. An experimental investigation of a novel four-wheel interconnection arrangement was published in 2002. Even though promising results were provided, no theoretical model was included in the research.

In recent years, Cao [30-35] investigated the dynamics of interconnected hydro-pneumatic suspensions at a full car level, particularly heavy vehicle applications. The fluidic couplings are realised through hydro-pneumatic struts [36], which have a compact design and are claimed to have larger effective working area than normal hydraulic cylinders. The struts provide considerable flexibility for various interconnection configurations among the hydraulic and pneumatic chambers, either hydraulically or pneumatically. A general

framework for the model designing and tuning is included. The simulation results confirmed the general benefits of having the freedom to independently specify modal characteristics.

2.3.2 Hydraulically interconnected suspension

An Australian company, Kinetic Pty Ltd., developed a series of hydraulically interconnected suspensions such as the RFS, H2 and X systems and achieved commercial success. Some of their products have been applied in Lexus GX 470 and 200 Series Toyota Land Cruiser. One of the focuses of this research will be on the H2 system, which is a roll-plane hydraulically interconnected suspension, and it is often referred to as HIS in the thesis.

The HIS system is right-left symmetry in structure, as shown in Figure 2.1. In the fluid system, it includes four double-acting hydraulic cylinders, two nitrogen-filled diaphragm-type accumulators, interconnecting pipelines, fittings and flexible hoses. The HIS system includes two identical fluid circuits, denoted as A and B respectively in the figure. In the HIS system, the main function of the accumulators is providing roll stiffness through their 'air spring' effect. Two interconnecting fluid circuits are pre-charged with a certain pressure. The piston rods are fixed to the wheel stations, with the cylinder bodies being mounted to the vehicle chassis. They couple the mechanical and hydraulic subsystems, ensuring that a specific suspension motion creates a desirable flow into the HIS pipelines [16]. When the vehicle is equipped with the HIS, the vehicles existing springs and shock absorbers are retained, but its front and rear anti-roll bars were removed.

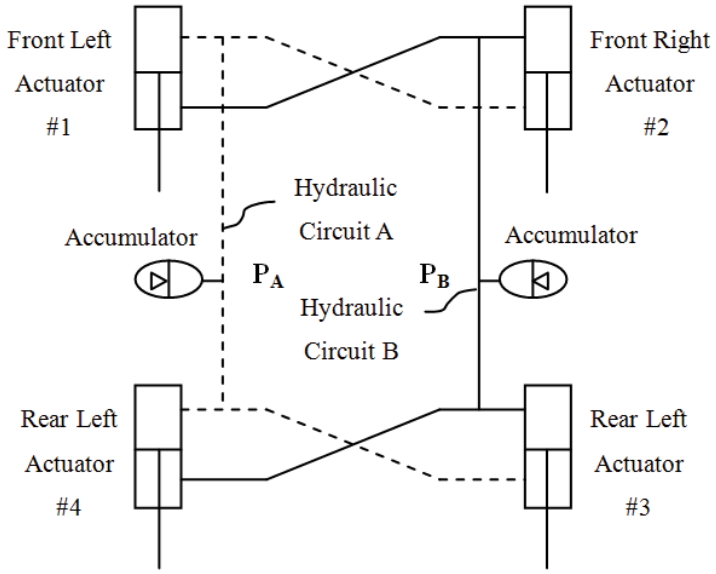

Figure 2.1 Schematic diagram of the roll-plane HIS system

In the roll mode, one hydraulic circuit is compressed, and the other is extended. In the compressed hydraulic circuit, the fluid is flowing from its cylinder chambers to its accumulators, and vice versa. Thus, the pressure in the compressed circuit increases while the pressure in the extended circuit decreases. The generated hydraulic forces from the pressure difference are acting against the vehicle body roll motion.

In the warp mode, two diagonally-opposed cylinders are in compression, and the other two are in extension. Fluid goes out of the upper chamber of the compressed cylinder, which can properly compensate the bottom chamber of the expanded cylinder on the same side, and vice versa. So theoretically there is no fluid flow into or out of the accumulators, and the HIS should have no effect on the warp mode.

In the bounce and pitch modes, there is a small amount or even no fluid flow into or out of the accumulators, so effects on those modes by the HIS are negligible. Therefore, the HIS has the capability to decouple the four vehicle motion modes.

The handling performance of the HIS equipped vehicles was investigated very recently by simulations with the software of ADAMS [37] and experiments with fishhook manoeuvre [38, 39]. The studies verified that the HIS with relatively high additional roll stiffness provided better rollover resistance, and the HIS did not change the roll moment distribution on the vehicle body, which is different from anti-roll bars.

Zhang & Smith [10, 16, 40] recently studied the modelling and dynamics of vehicles fitted with the HIS system with a focus on the roll stability and fluid circuit dynamics. In [41], ride comfort of the vehicle with the HIS system is analysed. Experimental studies also confirmed the roll resistance performance of the HIS system in [24, 42]. The results demonstrated the HIS is superior to anti-roll bars on anti-roll capacity. Theoretically, the HIS system can decouple roll mode from all other modes and enhance vehicle roll stability without compromising road holding ability. However, the road holding performance of the HIS system as a major advantage has not been thoroughly investigated.

The limitations are also clear that the HIS is not compatible to cope with large vehicle roll motions that exceed its limitation. Moreover, the HIS cannot handle the roll caused by the road excitations. When the road-excited roll motion is at a high frequency level, the HIS compromises the ride comfort slightly the same as anti-roll bars; and when the roll motion is at a low frequency level, the HIS can do little. It is because the passive HIS only responds to

the relative displacement between sprung and unsprung mass, but the vehicle body's roll motion is not necessarily associated with this relative displacement. When a scenario is without much relative suspension travel, the HIS cannot provide enough force to stabilise the vehicle roll. For example, if the sprung mass and unsprung mass move in phase with similar speed, such as low frequency roll caused by uneven or left-right leaning road surfaces, larger roll angle over critical point is likely to cause rollover. This kind of situation is beyond the capability of the HIS system.

2.4 Active suspension system

2.4.1 Conventional active suspension

Apart from the interconnected suspensions, active suspension is also an effective method to eliminate the compromise of the conventional passive suspensions. Furthermore, the active suspension is potential to deal with the vehicle roll motions caused by both the lateral accelerations and road excitations. Conventional active suspensions can be grouped into two classifications, semi-active suspensions and active suspensions. Semi-active suspensions usually have variable or adjustable parameters, such as stiffness and damping. Active suspensions require an external power source to provide external forces directly. The active suspensions have been widely studied in the last decades due to their viability in enhancing the conflicting performance objectives (such as ride comfort and drive handling) simultaneously.

After the first semi-active concept's appearance in the 1970s [43, 44], semi-active suspensions started to gain popularity [45-47]. In the proposed semi-active suspensions,

passive dampers are mostly replaced with variable dampers, such as dampers with controllable orifices, dampers with controllable damping, or magnetorheological dampers.

The advantages of semi-actives are that the vehicle suspension damping can be changed quickly with a very limited energy input. Thus, the simple structure and fast reaction characters enable the semi-active suspensions to be integrated with other vehicle systems such as Electronic Stability Program (ESP) to improve the whole vehicle performance. The limitations are also clear that semi-actives are not suitable to cope with larger vehicle motions. It is because the semi-active suspensions are similar to the passive suspensions that only respond to the relative velocity between sprung and unsprung mass. Their adjustable dampers only change the energy dissipation efficiency of suspensions, but cannot provide the control force to the vehicle. Obviously, the widely researched and applied semi-active suspensions that win their popularity are not because of their super function or performance but owing to their low initial cost and power consumption.

Active suspensions directly supply forces to the vehicle chassis, different from semi-active suspensions that only vary the viscous damping coefficient of the shock absorber to consume the vehicle vibration energy passively. If at least a portion of suspension force generation is provided through active power sources, the suspension is called active suspension [48].

To trace the origins of the development of the active suspensions, it is necessary to go back to 1950s and 1960s. They were applied in the aerospace industry, and the optimal control algorithms were also applied to the research of active suspensions [49]. The study of active

suspensions started from one degree of freedom (DOF), quarter car models [50, 51]. Although the earliest investigations were simple, they had profound effects on the practical implementation ten to twenty years later. After this, the studies of the active suspensions were developed into two-dimension, half car models [52] and they were followed by their three-dimension, full car counterparts [53-55].

With the advent and advancement of the electronics and microprocessors, the design and manufacturing techniques of the actuator and the sensor obtained significant progress, which enabled the practical application of the active suspensions. As a result, the active suspensions attracted increasing attention in the mid-1980s with the Lotus Esprit experimental vehicle. The vehicle obtained a substantial improvement in handling under customised and severe manoeuvres but the ride comfort was not demonstrated [48].

In 2004, Bose exhibited a prototype application of the technology that ideally eliminated the compromise between ride and handling performance after more than twenty years of research. Some related investigations of this active suspension were carried out in the 1990s [56, 57]. The system uses electromagnetic linear motors to replace the conventional automotive suspension system, as show in Figure 2.2, which can raise or lower the wheels in response to uneven bumps or potholes in the road. This active suspension adopts independently controlled actuators to control vehicle motions, so the system is able to provide an ideal control solution to a vehicle, adapting to various driving situations (e.g. braking, accelerating and cornering), and continuously compensating for road roughness. However, such a controlled actuator has to be a servo-valve driven, precision-made, super-clean, energy-hungry hydraulic strut, which brought about high cost in manufacturing and

maintaining [58]. Even after three decades development and a large amount of cost, it is suitable only for use in a luxury vehicle.

Figure 2.2 Bose Suspension Front Module [59]

Due to the demerits of the existing active suspensions (e.g. high manufacturing cost, uncertain reliability, excessive power consumption and inherent complexity), the development of the active suspension is following two trends.

The one is the frequency-based active suspensions with low-bandwidth or limited-bandwidth active systems [60, 61]. Due to narrowing down the control tasks assigned to active suspensions with vehicle motions at a certain frequency range, less energy will be consumed. One commonly used method is the slow-active suspensions, which only focus on suspension vibrations in the lower frequency range [62, 63], wherein the actuators only operate in a limited low bandwidth.

The other trend is to focus on the vehicle body main mode to narrow down control objectives. For example, the interconnected suspension schemes are applied to decouple the vehicle motion modes and concentrate the control objective on certain a motion mode. The benefits of this method are even lower power requirements than the frequency-based active suspensions, much lower cost and less control effort than the full-mode control by the independently controlled actuators, and also increased reliability [64, 65].

2.4.2 Active interconnected suspensions

The semi-active and active features are applied to interconnected suspensions in the last few decades. A semi-active pneumatically interconnected suspension with variable pressure was proposed in 2004 [66]. In 2010, the H2 system has been further developed by Tenneco Automotive with semi-active damping control. Investigation with modelling and simulation were carried out [67]. Hydraulic Body Motion Control Suspension (HBMC), a further development of the Kinetic's hydraulic suspension, was equipped in Nissan Patrol [68].

The increasing need for vehicle roll control brought about the appearance of the active interconnected suspensions [69]. In 1982, an active Hydragas system was introduced by Rideout [70]. The study concluded that even the more sophisticated model could not be accurately applied under the excitation with a frequency of 1-8 Hz. In the late 1990s, Rosam and Darling [64] developed the existing Hydragas system to a sealed low bandwidth suspension to actively control the roll motion. The results showed the active interconnected suspension had superior performance than the passive one.

In the 1980s and 90s, Nissan and Toyota developed hydraulic and pneumatic interconnections based active suspensions respectively [6, 71]. Their researches focused on control system development and experimentation, but the fluid system modelling was not given in detail. In the industry practice, interconnected active suspension technology through pure hydraulic means, which possesses faster response and powerful force, was also employed. Diagonally interconnected active suspensions, called Dynamic Ride Control (DRC) suspension, were applied on the Audi RS6. In this system, shock absorbers are diagonally linked and a pump was used to provide additional pressure to counteract rolling and pitching [72].

Active anti-roll bars can be treated as one of the active controlled mechanically interconnected suspensions for vehicle roll control. Active anti-roll bar system for large trucks has been developed in the 1990s [73-77]. The active interconnected suspension only for pitch control can also be found in [78, 79].

However, the aforementioned active interconnected suspensions were based on two-wheel interconnections, so the vehicle motion modes were not fully decoupled and negatively affected the control efficiency. Hence, a four-wheel interconnection based active suspension is necessary for better control performance and efficiency.

2.4.3 Active hydraulically interconnected suspension (active HIS)

In recent years, the concept of reconfigurable hydraulically interconnected suspensions has been proposed by Zhang [11] for the first time. The developed novel active interconnected

suspension is called Demand Dependent Active Suspension (DDAS), from which the interconnected circuits are reconfigurable in real time according to the motion the vehicle is experiencing. The particular focus of this research is on the roll-plane branch of the DDAS and referred to as active HIS in the thesis. A schematic drawing of Figure 2.3 shows that the active HIS, evolving from the HIS, also includes four hydraulic actuators that are interconnected to form two hydraulic circuits, denoted as A and B in the figure. The pressures in the two circuits are then controlled by a pressure control unit comprising a tank, a pressure pump, an accumulator, and a servo-valve. This way, the whole active suspension can be controlled by only one servo valve, which brings about substantial cost reduction compared to conventional active suspensions that use four valves for individual cylinder control.

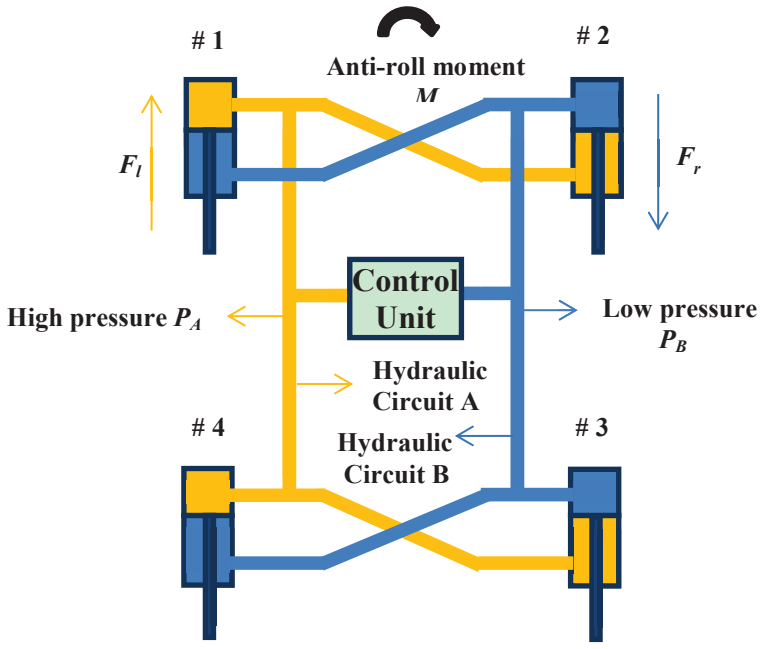

Figure 2.3 Diagram of the active HIS in roll configuration

The CAD model of the power unit is shown in Figure 2.4. The cylinders are mounted between the wheels and chassis. The vehicles' original springs and shock absorbers are retained when the vehicle is equipped with active HIS.

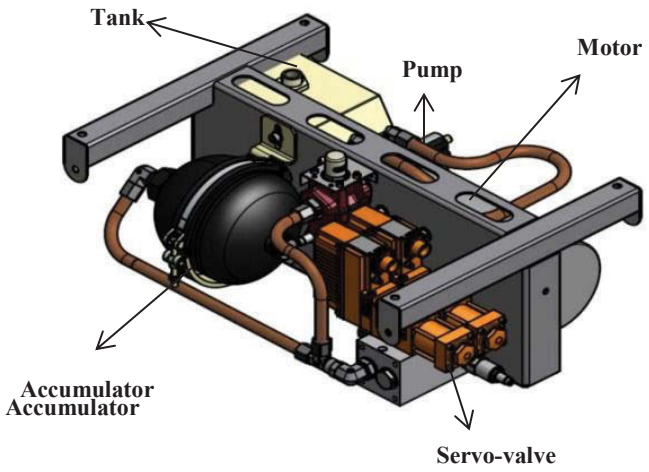

Figure 2.4 Designed pressure control unit of the active HIS suspension

The controller acquires data from the sensors to measure the roll angle of the vehicle body and sends a pressure command to the active HIS. In the roll control, one side (e.g., left) of the suspension needs to extend while another side (e.g., right) needs to compress to maintain the levelling of the vehicle body. In this circumstance, the pressure control unit pumps oil into circuit A to increase its pressure, while reducing the pressure (if not tank pressure) in circuit B, as shown in Figure 2.3.

The pressure difference between circuits A and B forms an anti-roll moment on the vehicle body through four cylinders. The control forces and moment are presented in Equation (2.1), (2.2) and (2.3).

$$F_l = 2a(P_A - P_B) \tag{2.1}$$

$$F_r = 2a(P_A - P_B) \tag{2.2}$$

$$M = F_l l / 2 + F_r l / 2 \tag{2.3}$$

where F_l and F_r are the forces acting on the vehicle body through the left and right actuators, respectively; P_A and P_B are the pressures inside the two hydraulic circuits; a is the piston area; M is the anti-roll moment and l is the distance between the left and right actuators.

2.5 Control theory

Control systems have been known and used for more than 2000 years. Bennett divided the history of automatic control into four main periods: Early Control (to 1900), the Pre-Classical Period (1900-1940), the Classical Period (1935-1960) and Modern Control (post-1955) [80].

The most significant control development in the 18th century was the steam engine governor. It was developed by James Watt for the need of governing the speed of the rotary steam engine. In the early 20th century, the feedback control developed rapidly. In 1922, Minorsky presented a very clear analysis of the PID control [81]. In the early 1920s, Black began to realise the significance of the negative feedback and work on it. The electronic negative feedback amplifier was the outcome of work on industrial problems. Nyquist proposed the Nyquist analysis that was published in 1932 [82].

In the 1940s and 1950s, the advent and growing availability of digital computers brought the control theory into a new era, and Athans placed the origin of the modern control theory

in 1956 [83]. The Moscow Conference held in 1960 was an important symbol of the establishment of the modern control theory, where Kalman presented a new treatment of the optimal control problem [84]. After the conference, the state-space approach dominated the subject for almost two decades [80]. Researchers rapidly realised that the powerful optimal control methods could hardly be used in general industrial practice for the reason that accurate plant models were not available and generally not achievable. This realistic problem has led to the development of parameter estimation and related techniques [85].

From the mid-1950s to mid-1960s, the adaptive control developed rapidly. A number of useful ideas on adaptive control were proposed: the model reference adaptive system, the self-tuning regulator, external control, dual control, and neural networks [86]. In the 1980s research began, and continues today, with making optimal feedback logic more robust to variations in the plant and disturbance models. One element of this research is worst-case and H∞ control, which developed out of differential game theory [87].

The investigation of intelligent control theory commenced from the 1960s while the automatic control was well established as a discipline. Fu [88-90] introduced the heuristic inference rules of the artificial intelligence into the learning control system. As a widely studied intelligent control algorithm, neural networks theory attempted to simulate the human brain function in many ways and did not rely on precise mathematical models, thus showing an adaptive and self-learning function. A number of achievements in robotics studies showed its broad application prospects. Fuzzy control is another representative intelligent control form. The fuzzy set theory proposed by Zadeh [91] in 1965 laid a solid

foundation for fuzzy control. In the subsequent twenty years, it has been successfully applied in practice [92].

In the recent half century, various control theories were applied to improve active suspension performance, including root locus [93], linear and fuzzy control [94], neural networks [95], LQG and LQR [96], H∞ control [97], skyhook, learning automata [98], non-linear control [99], and preview control [100]. Some of them are briefly introduced below. The reader is referred to the literature [9, 48, 101] for a more detailed review.

By 1974, skyhook control was proposed for semi-active suspensions [102]. Initially the absolute velocity of the sprung mass and the relative velocity between the sprung and unsprung mass were used to determine the control force in the skyhook control. Many years later, other system states, such as the displacement [103], and even other sensory inputs , such as the steering input [104], were also used to make the skyhook control more adaptable. Similar to other control methods (e.g. PID control, LQR control), one of the challenges for the skyhook control to be implemented successfully is the controller tuning. In addition, the clipped semi-active control and adaptation of semi-active control method were also applied to semi-active suspension systems [9].

As a typical optimal control method, the LQR control is for a linear plant with a quadratic cost function to be minimised by the control. The state of the plant must be available for feedback, the optimal control being in full-state-feedback form, and cost function terms may be frequency weighted [105]. Automotive applications usually presume time-invariance and white-noise excitation with the optimisation extending over infinite time and concerning

expected values. LQR solutions automatically produce controllers that are stable and somewhat robust, and they can be utilised straightforwardly.

Robust control is a form of optimal control prioritising low sensitivities to variations in the controlled plant and any disturbances. It applies to linear uncertain systems and involves minimising the maximum gain of the closed-loop system. Frequency response functions relate inputs to outputs. Plant modelling errors are addressed directly and worst-case conditions are presumed in the control design [58]. Recognised as one of the most robust and effective optimal control strategies, H∞ has long been employed in active suspension control, but the majority of the studies are based on quarter-car models [106, 107]. Several active H∞ control studies based on half-car [108] or full-car models [3, 109] showed promising results but require four independent actuators on each wheel station. The studies mentioned above were predominately conducted in a computer-based simulation environment [97, 110].

However, because the active HIS system is a newly developed suspension system, the above-mentioned control algorithms have not been applied to it yet. With the consideration of experimental implementation, several widely applied control methods are adopted in this study and realised in relatively basic forms. The optimal and robust H∞ control is adopted as the main control algorithm of this thesis. In addition, the representative classic control algorithm (PID control), optimal control algorithm (LQR control) and intelligent control algorithms (fuzzy logic control) are also applied to the active HIS.

3 The Investigation into the Road Holding Ability of the HIS

3.1 Introduction and rationale

This chapter focuses on comparing the road holding ability of anti-roll bars and the HIS. Vehicle dynamic analysis is carried out with three different configurations:

- vehicle with spring-damper only as a benchmark
- vehicle with spring-damper in conjunction with anti-roll bars
- vehicle with spring-damper in conjunction with the roll-plane HIS.

The models of the vehicle with the three different suspension configurations are developed. The modal analysis is conducted to investigate the effects of the stiffness change on different vehicle motion modes. The tyre loads of the anti-roll bars equipped vehicle and the HIS equipped vehicle are then compared in simulations. Three sets of different sinusoidal warp excitations and one set of single bump excitation are used to stimulate the vehicle motion. A typical sports utility vehicle (SUV) is tested on a full-scale, 4-post test rig that is able to provide the ground excitations to represent an uneven road surface. Experiments are implemented under the same ground excitations as the simulations.

The test setup used in this study, specially designed at the University of Technology Sydney (UTS), includes the interactions between multiple wheel stations in a simple manner. To the author's knowledge, it is the only known experimental facilities with the specific purpose of testing both the HIS and active HIS systems installed on an actual vehicle.

3.2 Background

Warp is also known as the articulation in which wheels diagonally-opposed move in phase while vehicle body motion is negligible. For two factors, the warp mode is quite distinct from the other three wheel dominant motion modes. Firstly, warp is the only non-planar mode, allowing the vehicle to travel on spatial surfaces. Furthermore, it is controlled entirely by surface geometry, with no sprung mass inertial component. It means the pure warp excitation by the road surface would not directly affect sprung mass stability, but rather influences handling performance through its effect on the tyre-ground contact force [16]. The tyre-ground load variation is therefore essential in off-road driving, where the warp mode is most obvious and inescapable. Under extreme circumstances, excessive tyre load transfer would lead to wheel-spin when tyres lose contact with the ground, which directly affects the trafficability and stability of the vehicle. However, such a motion mode has, until quite recently, received little attention in the academic literature.

Anti-roll bar system is one of the typical examples of mechanical interconnection that is able to decouple the roll mode from bounce and pitch [111]. Anti-roll bars have been widely adopted as standard configurations for increasing roll stiffness in road vehicles, but the disadvantage is that they cannot decouple the warp mode from other modes. That is, they can stiffen the roll mode without affecting bounce and pitch mode, but the warp mode is stiffened unfavourably. Consequently, the variations of tyre-ground contact forces are increased in the warp mode. Under some circumstances, it is necessary to disengage anti-roll bars from vehicles before the off-road driving. Active suspensions have been investigated intensively recently, but passive suspensions remain dominant in the vehicles

on the market because of their reliability and low cost. Although road holding performance improvements can be realised by adopting certain active suspensions [112] or some other active anti-roll equipment [113, 114], the associated structure complexity, high developing cost and energy consumption hampered their wider applications. Theoretically, the HIS system has the capability to decouple the roll mode from all other modes, so that it not only can overcome the compromise brought about by anti-roll bars but eliminates the high cost of the active equipment.

As mentioned in Chapter 2, the system modelling, ride dynamics and the roll resistance performance of the HIS equipped vehicles have been investigated intensively, but there is a lack of literature about the road holding ability study. This chapter focuses on the investigation into the road holding performance of the HIS system in comparison with anti-roll bars.

3.3 Model description

Models of the vehicle with three different suspension configurations have been drawn from multi-body vibration theory and fluid dynamics. The test vehicle is treated as a lumped-mass multi-body system and a seven degrees-of-freedom (DOF) model has been developed. The anti-roll bars are treated as massless torsional springs, and the HIS is simplified and linearized. Then the obtained subsystem models of the HIS and anti-roll bars are integrated with the vehicle model respectively.

3.3.1 Seven degrees-of-freedom model of full vehicle

A two-axle vehicle can be modelled as a system with seven DOFs as shown in Figure 3.1. It consists of a rigid sprung mass supported by four independent suspensions, which includes wheel assemblies as four unsprung masses.

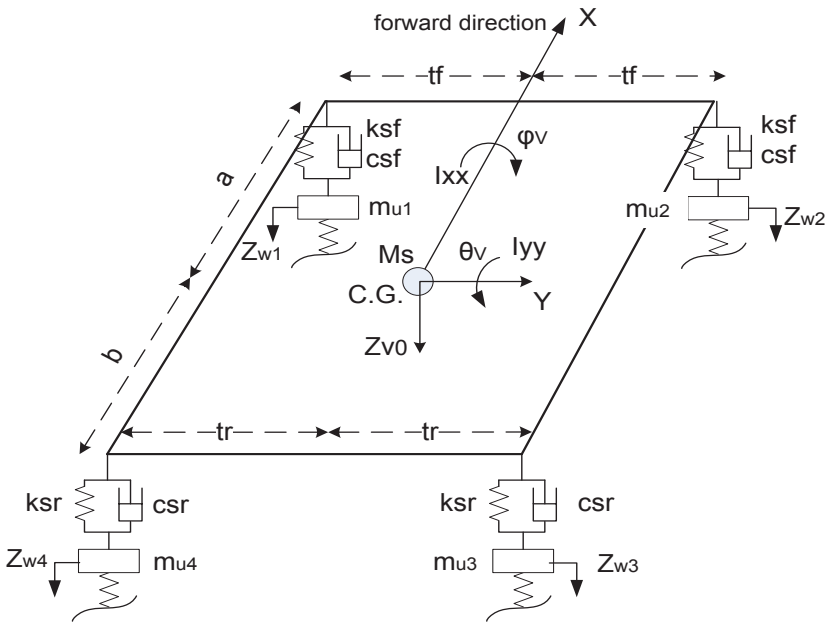

Figure 3.1 Seven-DOFs vehicle model

The sprung mass has inertial properties of mass (*Ms*), roll moment of inertia I_{xx}, and pitch moment of inertia I_{yy}. The roll and pitch rotations are restricted only to the sprung mass. The seven DOFs of the vehicle model includes sprung mass vertical centre-of-mass movement Z_{v0}, pitch angle θ_V and roll angle φ_V, four vertical centre-of-mass movements of unsprung masses:Z_{W1} Z_{W2} Z_{W3} Z_{W4}. The origin of coordinates is fixed in the CG of the sprung mass. It is assumed in this section linear behaviour of the suspension springs and shock absorbers. The parameters of the vehicle model are presented in Table 3.1.

Table 3.1 Vehicle parameters

Parameters	Character	Value
Sprung mass	M_s	1800 kg
Unsprung masses	m_u	42 kg
Spring stiffness of the front suspension	K_{sf}	40 kN/m
Spring stiffness of the rear suspension	K_{sr}	46.5 kN/m
Damping coefficient of front and rear suspension	C_{sf}, C_{sr}	2000 Ns/m
Vertical stiffness of tyres	K_t	200 kN/m
Front anti-roll bar stiffness	K_{af}	35 kNm/rad
Rear anti-roll bar stiffness	K_{ar}	6 kNm/rad
Pitch moment inertia of the sprung mass	I_{yy}	3700 kgm^2
Roll moment inertia of the sprung mass	I_{xx}	870 kgm^2
Distance from the sprung mass CG to the front axle	a	1.37 m
Distance from the sprung mass CG to the rear axle	b	1.48 m
Half width of the front axle	tf	0.575 m
Half width of the rear axle	tr	0.575 m
Front anti-roll bar length	lf	1.25 m
Rear anti-roll bar length	lr	0.65 m

By applying Newton's second law, the full vehicle suspension equations of motion are derived and written in the matrix form

$$\mathbf{M}\ddot{\mathbf{Z}} + \mathbf{C}\dot{\mathbf{Z}} + \mathbf{K}\mathbf{Z} = \mathbf{F}, \tag{3.1}$$

where **M, C, K** $\in R^{7\times7}$ are the mass, damping and stiffness matrices; **Z** is the displacement vector at continuous time *t*; **F** is the road input matrix.

Equation (3.1) can be converted to a continuous-time state space model as

$$\mathbf{T}\dot{\mathbf{X}} = \mathbf{S}\mathbf{X} + \mathbf{F}_{ex}, \text{ or} \tag{3.2}$$

$$\begin{bmatrix} \mathbf{I}_7 & \mathbf{0} \\ \mathbf{0} & \mathbf{M} \end{bmatrix} \begin{bmatrix} \dot{\mathbf{Z}} \\ \ddot{\mathbf{Z}} \end{bmatrix} = \begin{bmatrix} \mathbf{0} & \mathbf{I}_7 \\ -\mathbf{K} & -\mathbf{C} \end{bmatrix} \begin{bmatrix} \mathbf{Z} \\ \dot{\mathbf{Z}} \end{bmatrix} + \begin{bmatrix} \mathbf{0} \\ \mathbf{F}_{ex} \end{bmatrix}. \tag{3.3}$$

The state vector describing the motion of the sprung and unsprung lumped suspension system is defined as

$$\mathbf{X}_M = \begin{bmatrix} \mathbf{Z} & \dot{\mathbf{Z}} \end{bmatrix}^T, \tag{3.4}$$

where the displacement vector is $\mathbf{Z} = \begin{bmatrix} Z_{W1} & Z_{W2} & Z_{W3} & Z_{W4} & Z_{V0} & \theta_V & \varphi_V \end{bmatrix}$ and the velocity vector is $\dot{\mathbf{Z}} = \begin{bmatrix} \dot{Z}_{W1} & \dot{Z}_{W2} & \dot{Z}_{W3} & \dot{Z}_{W4} & \dot{Z}_{V0} & \dot{\theta}_V & \dot{\varphi}_V \end{bmatrix}$.

3.3.2 Anti-roll bars model

Anti-roll bars connecting the left and right wheels are commonly used components to increase a vehicle's roll stiffness. Anti-roll bars may have simple or complicated irregular shapes for convenient packaging on the vehicle chassis. The anti-roll bars are modelled as massless torsional springs and integrated into the seven-DOF vehicle model.

There are generally two anti-roll bars on the two-axle vehicle. The torsional stiffness of the front and rear anti-roll bars is represented as k_{af} and k_{ar}, and the length of the front and rear anti-roll bars are l_f and l_r respectively. Due to the anti-roll bar only working when the suspension travel between the left and right is different, the additional stiffness $\mathbf{K}_A$ caused by anti-roll bars is therefore calculated in the matrix form as

$$\mathbf{K}_A = \begin{bmatrix} \frac{k_{af}}{l_f^2} & -\frac{k_{af}}{l_f^2} & 0 & 0 & 0 & 0 & -\frac{k_{af}}{l_f} \\ -\frac{k_{af}}{l_f^2} & \frac{k_{af}}{l_f^2} & 0 & 0 & 0 & 0 & \frac{k_{af}}{l_f} \\ 0 & 0 & \frac{k_{ar}}{l_r^2} & -\frac{k_{ar}}{l_r^2} & 0 & 0 & \frac{k_{ar}}{l_r} \\ 0 & 0 & -\frac{k_{ar}}{l_r^2} & \frac{k_{ar}}{l_r^2} & 0 & 0 & -\frac{k_{ar}}{l_r} \\ 0 & 0 & 0 & 0 & 0 & 0 & 0 \\ 0 & 0 & 0 & 0 & 0 & 0 & 0 \\ -\frac{k_{af}}{l_f} & \frac{k_{af}}{l_f} & \frac{k_{ar}}{l_r} & -\frac{k_{ar}}{l_r} & 0 & 0 & k_{af}+k_{ar} \end{bmatrix}. \quad (3.5)$$

If the stiffness coefficient matrix of the original springs is denoted as $\mathbf{K}_S$, then in Equation (3.1) the stiffness coefficient matrix $\mathbf{K}$ is replaced as

$$\mathbf{K} = \mathbf{K}_S + \mathbf{K}_A . \quad (3.6)$$

3.3.3 Vehicle fitted with HIS

3.3.3.1 Mechanical system equations

The model of the vehicle fitted with the roll-plane HIS system includes two subsystems. One is hydraulic and one is mechanical. The equation of motion for the vehicle of the integrated HIS-vehicle system can be written in the form as

$$\mathbf{M}\ddot{\mathbf{Z}} + \mathbf{C}\dot{\mathbf{Z}} + \mathbf{K}\mathbf{Z} + \mathbf{D}_1\mathbf{A}\mathbf{P} = \mathbf{F}_{ext}, \text{ [40]} \quad (3.7)$$

where the mass matrix $\mathbf{M}$, damping matrix $\mathbf{C}$, stiffness matrix $\mathbf{K}$, displacement vector $\mathbf{Z}$, and excitation forces $\mathbf{F}_{ext}$ are as defined previously; $\mathbf{D}_1\mathbf{A}\mathbf{P}$ represents the forces of the

hydraulic actuators caused by the hydraulic pressure; $\mathbf{D}_1$ is linear transformation matrix. The pressure vector **P** and area matrix **A**, related to the corresponding cylinder chambers (T-top, B-bottom), are defined as

$$\mathbf{P} = \begin{bmatrix} \mathbf{P}_T^1 & \mathbf{P}_B^1 & \mathbf{P}_T^2 & \mathbf{P}_B^2 & \mathbf{P}_T^3 & \mathbf{P}_B^3 & \mathbf{P}_T^4 & \mathbf{P}_B^4 \end{bmatrix}^T, \text{ and} \tag{3.8}$$

$$\mathbf{A} = diag\begin{bmatrix} \mathbf{A}_T^1 & \mathbf{A}_B^1 & \mathbf{A}_T^2 & \mathbf{A}_B^2 & \mathbf{A}_T^3 & \mathbf{A}_B^3 & \mathbf{A}_T^4 & \mathbf{A}_B^4 \end{bmatrix}. \tag{3.9}$$

3.3.3.2 Fluidic equations

As in developing the model of the hydraulic system, some assumptions are made in this section: (a) piston friction is not considered; (b) the fluid is incompressible compared with nitrogen gas in the accumulator; (c) the oil density is constant; (d) the viscous resistance of the fluid in the whole system is simplified as a linear damping, which is used to represent the damping effects of the fluid system. The fluidic parameters of the HIS are shown in Table 3.2. The method in [40] is used for the fluid system modelling.

Table 3.2 Hydraulic parameters of the HIS

Parameters	Character	Value
Hydraulic fluid density	ρ	870 kg/m^3
Bulk modulus	β	1400 Mpa
Accumulator pre-charge gas volume	Vp	3.2 $\times 10^{-4}$ m^3
Accumulator pre-charge pressure	Pp	1 Mpa
Diameter of cylinder piston	Dp	0.032 m
Diameter of cylinder piston rod	Dr	0.016 m
Mean system pressure	$\bar{P}$	3 Mpa

As shown in Figure 2.1, the cylinder chambers form the boundary between the mechanical and hydraulic subsystems. The compressibility of the hydraulic fluid in each of the cylinder chambers is shown as

$$Q_{comp} = \frac{V}{\beta}\frac{dP}{dt}, \tag{3.10}$$

where V and β are the volume and effective bulk modulus of the cylinder chamber, P is the pressure. Thus, the fluid compressibility in the cylinder chamber is given by

$$Q_{comp} = \dot{Z}_{s-u}(t)A - Q(t) = \frac{V_0 - Z_{s-u}(t)A}{\beta}\dot{P}(t), \tag{3.11}$$

where $Q(t)$ denotes the volume flow rate where the pipeline meets the cylinder chamber; $\dot{P}$ is the rate of the change of in-chamber pressure; V_0 is the initial volume of the cylinder chamber; and Z_{s-u} is the relative displacement between the unsprung mass and the point of strut contact at the corner of the sprung mass.

When applied to all eight chambers in the fluid system in Figure 2.1, Equation (3.11) can be re-written as

$$\mathbf{Q}(t) = \mathbf{A}\cdot\mathbf{D}_1^T\cdot\dot{\mathbf{Z}}(t) + \mathbf{V}(t)\cdot\dot{\mathbf{P}}(t), \tag{3.12}$$

in which $\mathbf{Q}$ is the flow vector as $\mathbf{Q} = \begin{bmatrix} Q_T^1 & Q_B^1 & Q_T^2 & Q_B^2 & Q_T^3 & Q_B^3 & Q_T^4 & Q_B^4 \end{bmatrix}^T$; $\mathbf{V}(t)$ is a time-variant matrix of the cylinder volume and bulk modulus terms, and $\mathbf{D}_1^T$ is a constant linear transformation matrix.

The accumulators are modelled by assuming an adiabatic process. The pressure and volume at any time in the accumulator P_a and V_a are related to the pre-charged values, P_p and V_p , as follows

$$P_a V_a^{\gamma} = P_p V_p^{\gamma} = cons, \tag{3.13}$$

where γ is the ratio of the specific heats for the gas. The adiabatic gas law is used to model the accumulator pressure as a function of gas volume at the pre-charged pressure. Taking the partial time derivative of Equation (3.13), and noting that the flow into the accumulator is given by $Q_a = -\partial V_a / \partial t$, the pressure gradient of the accumulator is written as a nonlinear function of the pressure, i.e.

$$\dot{P}_a = \frac{\gamma Q_a P_a}{V_p} \left(\frac{P_a}{P_p} \right)^{1/\gamma} . \tag{3.14}$$

By assuming no fluid resistance in the pipelines, by the arrangement of the interconnection, we have

$$P_T^1 = P_A + R_C Q_T^1 \ , \ P_B^2 = P_A + R_C Q_B^2 , \ P_B^3 = P_A + R_C Q_B^3 , \ P_T^4 = P_A + R_C Q_T^4 , \tag{3.15}$$

$$P_B^1 = P_B + R_C Q_B^1 \ , \ P_T^2 = P_B + R_C Q_T^2 , \ P_T^3 = P_B + R_C Q_T^3 , \ P_B^4 = P_B + R_C Q_B^4 , \tag{3.16}$$

$$Q_A = Q_T^1 + Q_B^2 + Q_B^3 + Q_T^4 \ , \ Q_B = Q_B^1 + Q_T^2 + Q_T^3 + Q_B^4 , \tag{3.17}$$

where R_C is the damping coefficient; P_A , Q_A are the pressure and flow rate of the accumulator in the hydraulic circuit A; P_B, Q_B are the pressure and the flow rate of the

accumulator in the hydraulic circuit B; Q_T^1 and P_T^1 are the flow and pressure of the top chamber of the cylinder one; Q_B^2 and P_B^2 are the flow and pressure of the bottom chamber of the cylinder two and so on. Cylinders one to four are on the front-left, front-right, rear right, rear left respectively as show in Figure 2.1.

The fluid subsystem equations are in the following form:

$$\mathbf{T}_H \dot{\mathbf{X}}_H = \mathbf{S}_H \mathbf{X}_H + \mathbf{F}_H , \tag{3.18}$$

where the hydraulic subsystem state vector $\mathbf{X}_H$ includes the two pressure terms P_A and P_B; $\mathbf{F}_H$ refers to the forces exerted on the fluid subsystem.

3.3.3.3 Integrated system equations

The state vector describing the dynamic states of the hydraulic subsystem is defined as

$$\mathbf{X}_H = \begin{bmatrix} P_A & P_B \end{bmatrix}^T . \tag{3.19}$$

Through integrating the Equation (3.7) and Equation (3.20), the state vector of the full vehicle fitted with a roll-plane HIS is obtained

$$\mathbf{X} = \begin{bmatrix} \mathbf{X}_M^T & \mathbf{X}_H^T \end{bmatrix}^T \text{ (14+2=16 elements).} \tag{3.21}$$

By combining Equation (3.7) and Equation (3.12) - (3.18), the full vehicle system state space equation is derived as

$$\mathbf{T}\dot{\mathbf{X}} = \mathbf{S}\mathbf{X} + \mathbf{F} \text{ , or} \tag{3.22}$$

$$\begin{bmatrix} \mathbf{I}_7 & \mathbf{0} & \mathbf{0} \\ \mathbf{0} & \mathbf{M}_7 & \mathbf{0} \\ \mathbf{0} & \mathbf{0} & (\mathbf{T}_H)_2 \end{bmatrix} \begin{bmatrix} \dot{\mathbf{Z}} \\ \ddot{\mathbf{Z}} \\ \dot{\mathbf{X}}_H \end{bmatrix} = \begin{bmatrix} \mathbf{0} & \mathbf{I}_7 & \mathbf{0} \\ -\mathbf{K} & -\mathbf{C}-\mathbf{C}_H & -\mathbf{D}_1\mathbf{A}\mathbf{D}_2 \\ \mathbf{K}_H & \mathbf{D}_2^T\mathbf{A}\mathbf{D}_1^T & \mathbf{S}_H \end{bmatrix}_{16\times 16} \begin{bmatrix} \mathbf{Z} \\ \dot{\mathbf{Z}} \\ \mathbf{X}_H \end{bmatrix}_{16} + \begin{bmatrix} \mathbf{0} \\ \mathbf{F}_M \\ \mathbf{0} \end{bmatrix}_{16}, \quad (3.23)$$

where $\mathbf{K}_H$ is the stiffness matrix of the hydraulic system; $\mathbf{C}_H$ is the coefficient matrix of the fluid subsystem; $\mathbf{D}_2$ is a linear transformation matrix.

3.4 Modal analysis

To perform the modal analysis using the vehicle model derived before, equation (3.22) need to be written as the following standard state space equation

$$\dot{\mathbf{X}} = \mathbf{A}\mathbf{X} + \mathbf{B}\mathbf{F}, \quad (3.24)$$

where **A** and **X** represent the system matrix and the state variable vector respectively. With solving the eigen problem of the system matrix **A**, seven pairs of conjugate eigenvalues and eigenvectors of the structural system can be obtained.

Table 3.3 shows the natural frequencies and modal shapes of the vehicle without anti-roll bars. From the table, it can be seen that the first three columns are body predominant modes: body roll, body bounce and body pitch. The last four columns are wheel predominant modes: wheel pitch, wheel roll, wheel bounce and warp. Bounce and pitch modes both involve body vertical movement and pitch angular movement that illustrates the deep coupling between these two modes. In warp mode, the vehicle body motion is very small compared to wheel motions. As the inertia properties of the vehicle are kept the same, so the natural frequency indicates the overall stiffness of each motion mode. The increased natural frequency means increased stiffness of this mode.

Table 3.3 Modal analysis of vehicle with spring-damper only

Modes	1st Body roll	2nd Body bounce	3rd Body pitch	4th Wheel pitch	5th Wheel roll	6th Wheel bounce	7th Warp
Natural Frequency (Hz)	1.27	1.38	1.53	13.09	13.16	13.23	13.33
Damping ratio	0.156	0.186	0.174	0.296	0.292	0.294	0.285
Modal shapes							
Wheel 1 (front left)	1	1	1	1	1	1	1
Wheel 2 (front right)	-1	1	1	1	-1	1	-1
Wheel 3 (rear right)	-0.811	0.081	-10.29	-0.025	-0.911	40.588	1.087
Wheel 4 (rear left)	0.811	0.081	-10.29	-0.025	0.911	40.588	-1.087
CG vertical displacement	0	-3.23	32.29	0.062	0	2.44	0
Pitch angle	0	-2.191	-24.16	0.043	0	-1.798	0
Roll angle	-10.20	0	0	0	0.099	0	-0.067

Table 3.4 is the summary of the natural frequencies of three different vehicle configurations. They are 1) vehicle with spring-damper only, 2) vehicle with anti-roll bars, and 3) vehicle with roll-plane HIS. From the comparison it can be seen that the vehicle roll mode natural frequency increases from 1.27 Hz to 1.56 Hz with the anti-roll bars and to 1.82 Hz with the roll-plane HIS. The warp mode natural frequency with anti-roll bars rises from 13.33 Hz to 14.18 Hz, but the roll-plane HIS system remained with almost no change. The results illustrate that anti-roll bars can improve the roll stiffness while bounce mode maintained the same, but the effect on warp mode is negative. The stiffened warp mode implies decreases in road holding ability. The roll-plane HIS can provide even stiffer roll mode than anti-roll bars, which agrees well with the testing results in the reference [42]. More important is that both bounce and warp modes are kept very much the same. It clearly demonstrated the advantage of the mode decoupling property of the HIS system over anti-roll bars.

Table 3.4 Natural frequency comparisons of three configurations

Natural Frequency (Hz)	Body roll	Body bounce	Body pitch	Wheel pitch	Wheel roll	Wheel bounce	Warp
Without anti-roll bars	1.27	1.38	1.53	13.09	13.16	13.23	13.33
anti-roll bars	**1.56**	1.38	1.53	13.09	**13.97**	13.23	**14.18**
Roll-plane HIS	**1.68**	1.39	1.53	13.10	**14.04**	13.24	13.30

3.5 Simulations

3.5.1 Simulation conditions

Tyre force variation is also called load transfer, and it is studied here to understand how the road holding ability is affected. The aforementioned three different vehicle configurations are compared. The vehicle with spring-damper only is used as a benchmark. To compare the effects of anti-roll bars and the HIS on the road holding ability under different road conditions, three sets of warp excitations and a set of single wheel hop excitations are adopted in both simulations and experiments. For simplifying and normalizing the test conditions, the excitations for warp motion mode are chosen to be sinusoidal. An example of the warp excitations with 50 mm amplitude and 0.2 Hz frequency are presented. As shown in Figure 3.2, two in-phase ground inputs act on the front left and rear left wheels and two out-of-phase ground inputs act on the front right and rear right wheels. The other two sets of road excitations are similar but with 10 mm and 3 mm amplitude, and 1 Hz and 10 Hz frequencies respectively. As shown in Figure 3.3, the ground input of the single wheel hop is used to simulate a 50 mm bump on the road. These test scenarios represent typical driving conditions, although larger displacement would be experienced during extreme off-road driving.

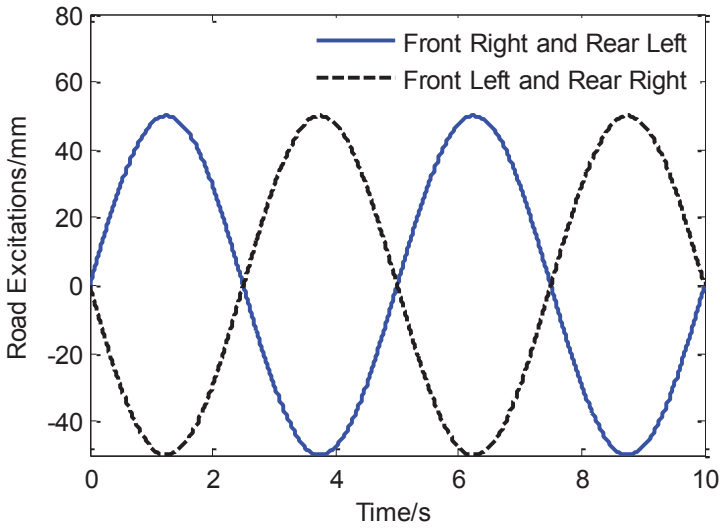

Figure 3.2 Excitation signal example (50 mm amplitude and 0.2 Hz frequency)

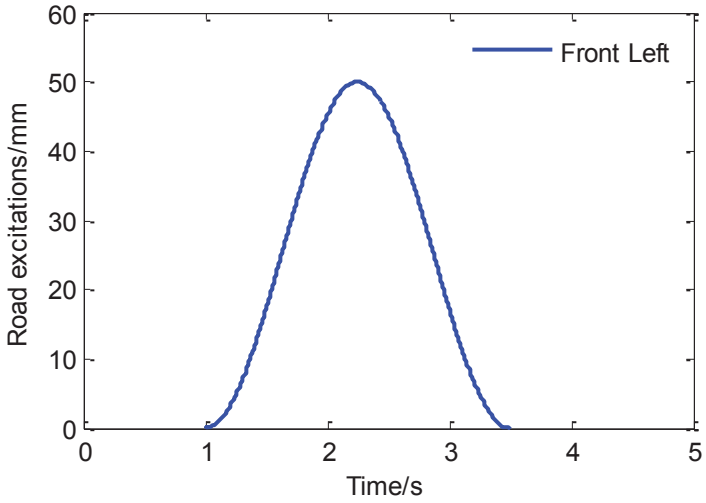

Figure 3.3 Single wheel hop

3.5.2 Simulation results

3.5.2.1 Sinusoidal warp road excitations with 50 mm amplitude and 0.2 Hz frequency

Since the effects of the warp motion mode on vehicle handling are more pronounced at lower frequencies, for instance when the vehicle is running on an uneven surface at

relatively low speed, the frequency of the road excitations is chosen as 0.2 Hz in agreement with the signal in Figure 3.4. The ground excitations simulate the vehicle running on a sinusoidal road surface with left and right track 180 degrees of phase shift. The frequency of 0.2 Hz is equivalent to a speed of 5 kilometres per hour if the wavelength of the road surface is 6 metres and the wheelbase of the vehicle is 3 metres.

Due to the system symmetry, only the force variations of the front right and rear left tyres are presented here in Figure 3.4 and Figure 3.5. From the results, a larger force variation is observed for the anti-roll bars, but that of the conventional suspension and HIS are almost the same. It seems that the change of the warp mode natural frequency from 13.33 Hz to 14.18 Hz by the anti-roll bars is not significant, but the tyre force variations have increased substantially by 56% at the front and 57% at the rear.

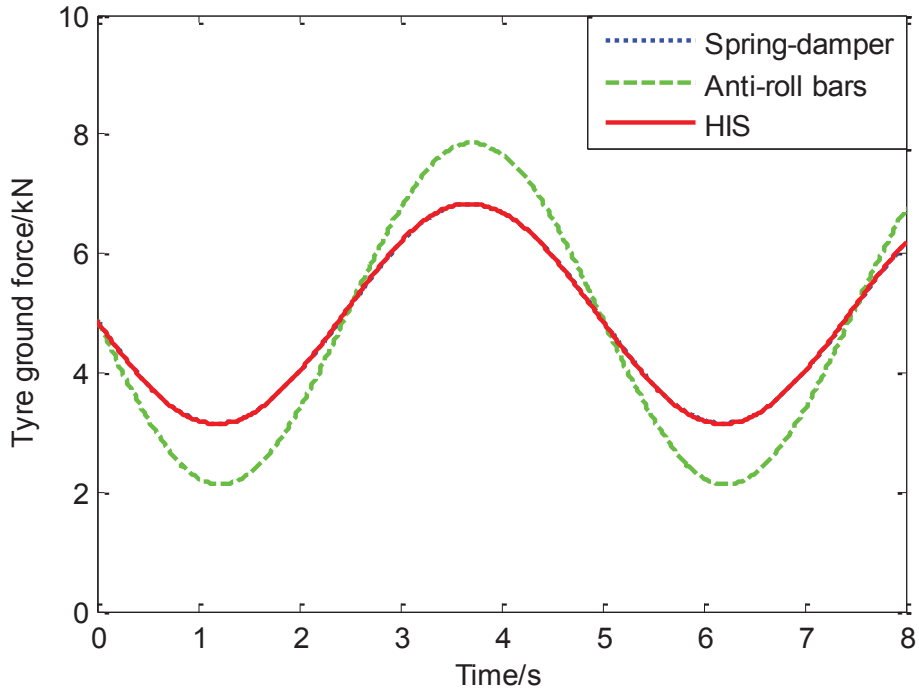

Figure 3.4 Tyre force at front right in simulation under 50 mm and 0.2 Hz road input

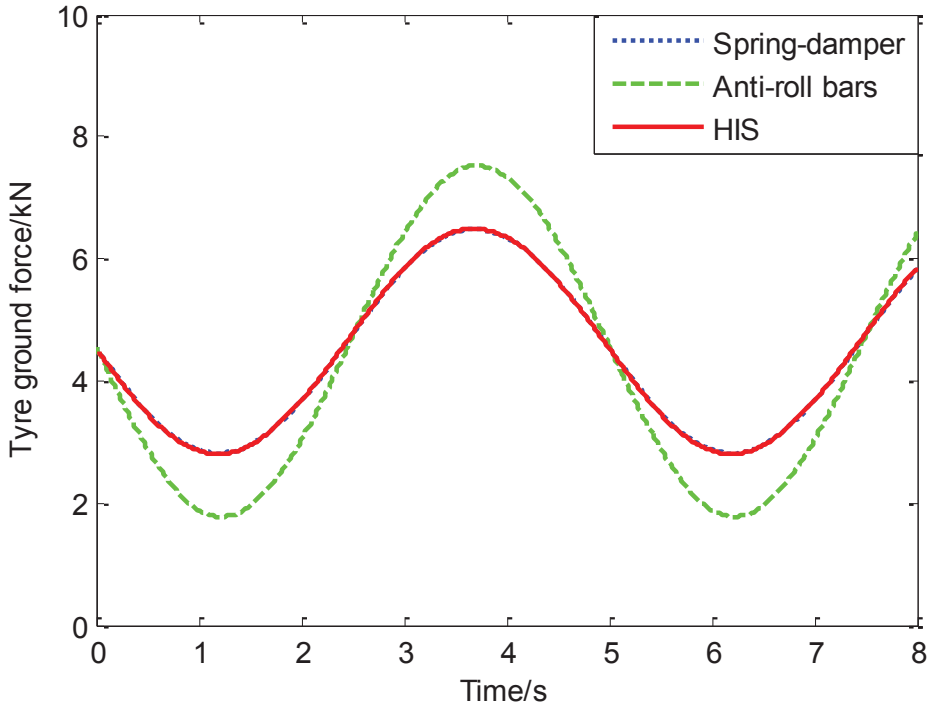

Figure 3.5 Tyre force at rear left in simulation under 50 mm and 0.2 Hz road input

Figure 3.4 and Figure 3.5 indicate that when the vehicle speed is low, the vehicle with anti-roll bars shows much worse road holding performance than the other two configurations.

The roll and pitch angular velocities at the CG of the vehicle body are shown in Figure 3.6 and Figure 3.7. In Figure 3.6, the employment of the roll-plane HIS reduces the roll angular velocity of the vehicle by 68%, while the anti-roll bars causes an increase of 35%. It is noticed that the roll angular velocity of the vehicle with anti-roll bars is out of phase with the other two curves, which is induced by the anti-roll bars adding more roll stiffness at the front of the vehicle and less at the rear. The distributions of the roll stiffness of the vehicle body have been changed. Thus, roll motions of front and rear of the vehicle body are different with anti-roll bars.

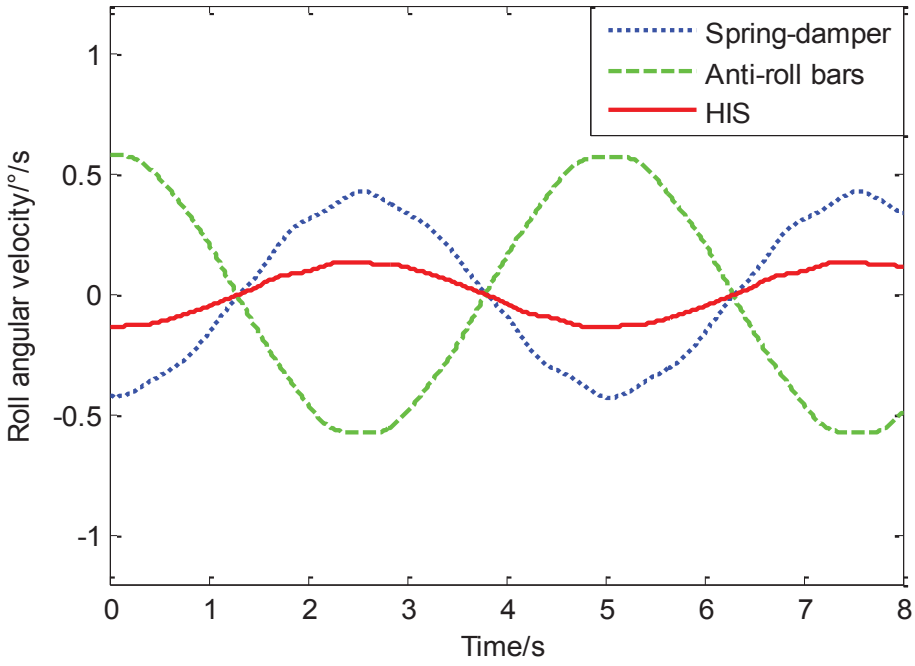

Figure 3.6 Roll angular velocity at centre of gravity in simulation

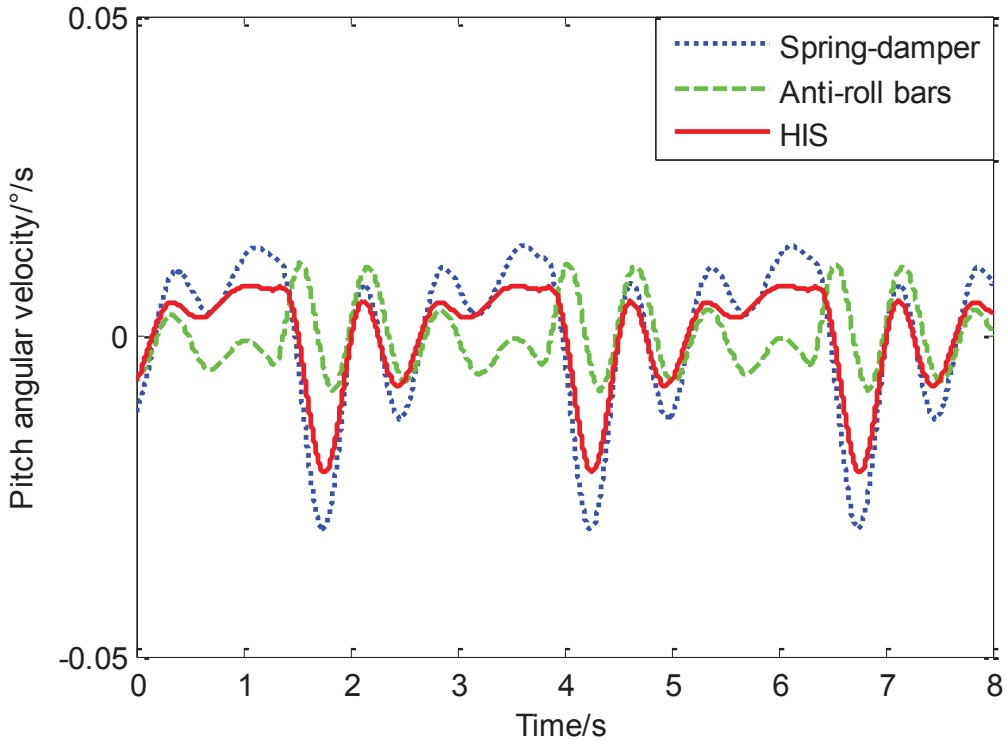

Figure 3.7 Pitch angular velocity at centre of gravity in simulation

It can be seen from Figure 3.6 that the anti-roll bars do not reduce the roll angular velocity. It is because that under the warp mode, the vehicle body can only move slightly and the motion of the vehicle body is not a standard roll motion. Furthermore, as mentioned in Chapter2, both the anti-roll bars and the passive HIS can reduce the roll angle of the vehicle by adding roll stiffness to the vehicle, so they are able to handle the roll motion caused by lateral excitations but cannot deal with the roll motion caused by ground excitations. The roll and pitch angular velocities are adopted here to compare the effect of the anti-roll bars and the HIS on the ride comfort of the vehicle. The obtained different roll angular velocities are mainly caused by the different structures, mass and stiffness distributions of the anti-rollbars and the HIS as well as the additional damping introduced by the HIS.

The pitch angular velocities reduce to 66% and 45% of the benchmark with the mounting of the HIS and anti-roll bars in simulations as shown in Figure 3.7. However, in consideration of the order of magnitude, the pitch rates are much smaller than the roll rates. Hence, they are insignificant when considering the ride comfort. As indicated in Figure 3.6 and Figure 3.7, the HIS improves the ride comfort but anti-roll bars worsen it.

It can be seen form Figure 3.7 that the anti-roll bars reduce the pitch angular velocity more than the HIS. The reason is that in the warp mode, the pitch angular velocity is even smaller than the roll angular velocity on the centre of gravity. As same as the roll motion, the pitch motion is influenced by the different structures, mass and stiffness distributions of the anti-rollbars and the HIS.

3.5.2.2 Sinusoidal warp road excitations with 10 mm amplitude and 1 Hz frequency

For investigating the effects of anti-roll bars and the HIS on the tyre force variations at relatively high frequencies and small amplitudes, the warp excitations with 10 mm and 1 Hz, 3 mm and 10 Hz are adopted. In this simulation, the amplitude of the excitations is 10 mm, and the frequency is 1 Hz.

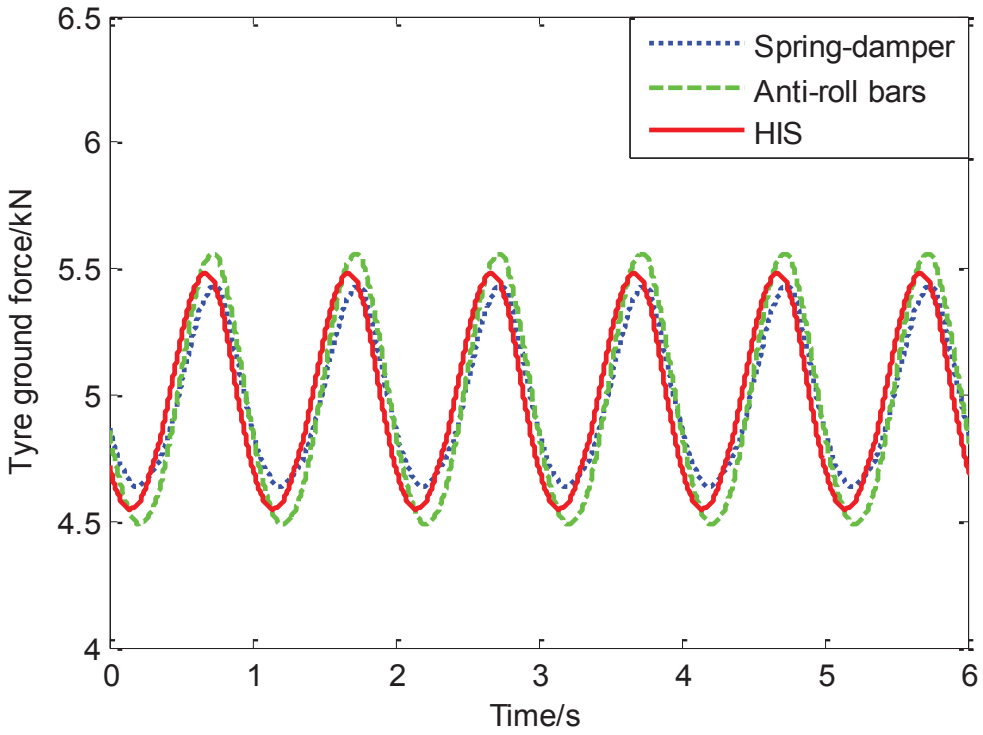

Figure 3.8 Tyre force at front right in simulation under 10 mm and 1 Hz road input

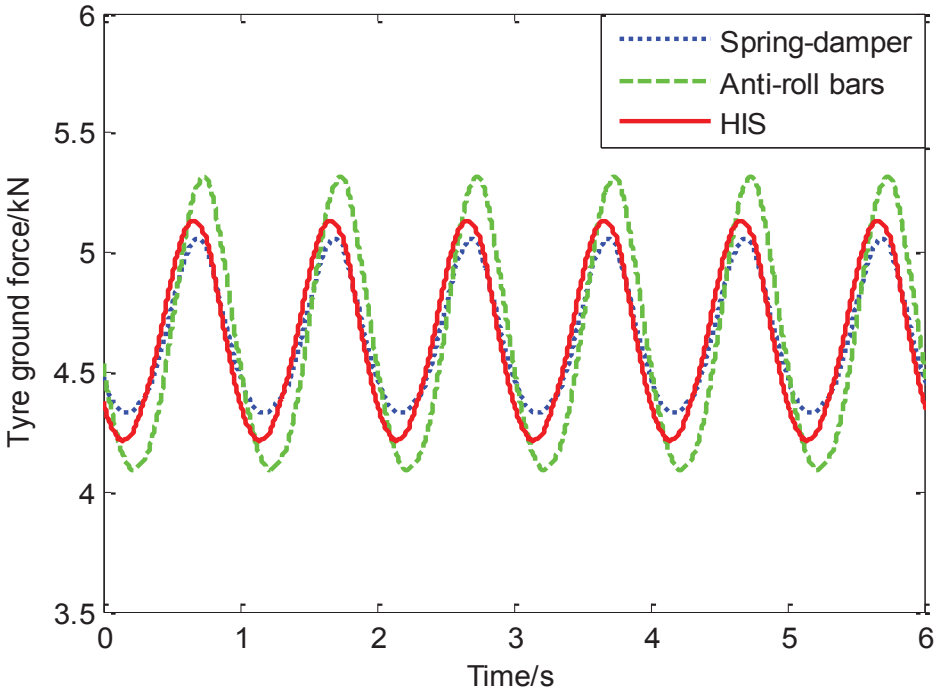

Figure 3.9 Tyre force at rear left in simulation under 10 mm and 1 Hz road input

The frequency of 1 Hz is equivalent to a speed of 22 kilometres per hour if the wavelength of the road surface is 6 metres and the wheelbase of the vehicle is 3 metres. The front right and rear left tyre forces are shown in Figure 3.8 and Figure 3.9, from which it can be seen that the tyre load variations of the test vehicle are also in coincidence with the modal analysis results, but the data with the HIS increase slightly by 26% at the rear and 18% at the front due to the system damping of the HIS. However, they are still better than that of the anti-roll bars (increase by 67% at the front and 36% at the rear).

3.5.2.3 Sinusoidal warp road excitations with 3 mm amplitude and 10 Hz frequency

With the frequency of road excitations increasing to 10 Hz, the results describe a different tendency in Figure 3.10 and Figure 3.11.

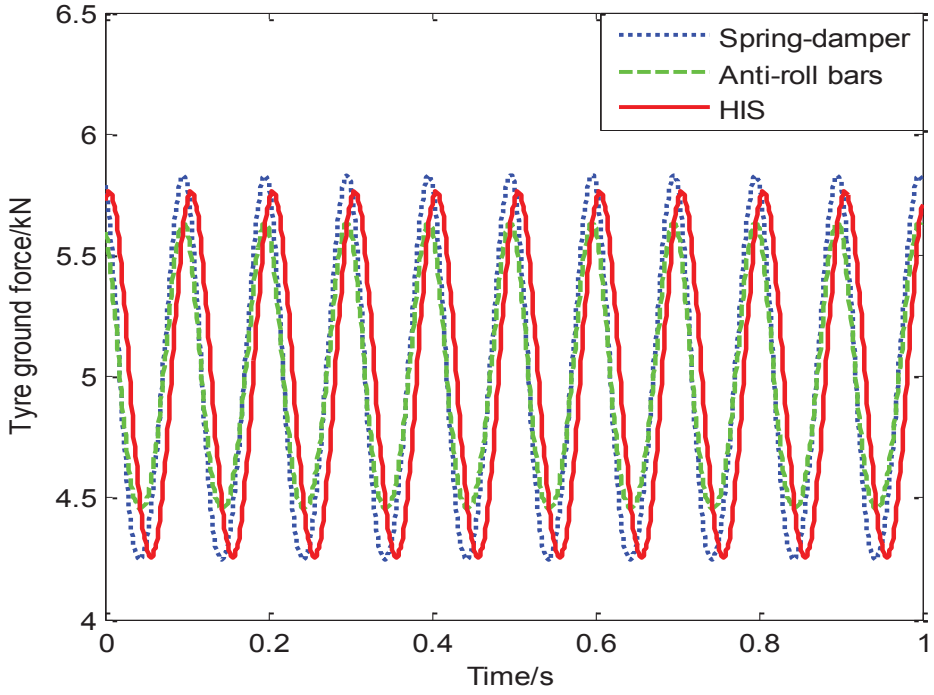

Figure 3.10 Tyre force at front right in simulation under 3 mm and 10 Hz road input

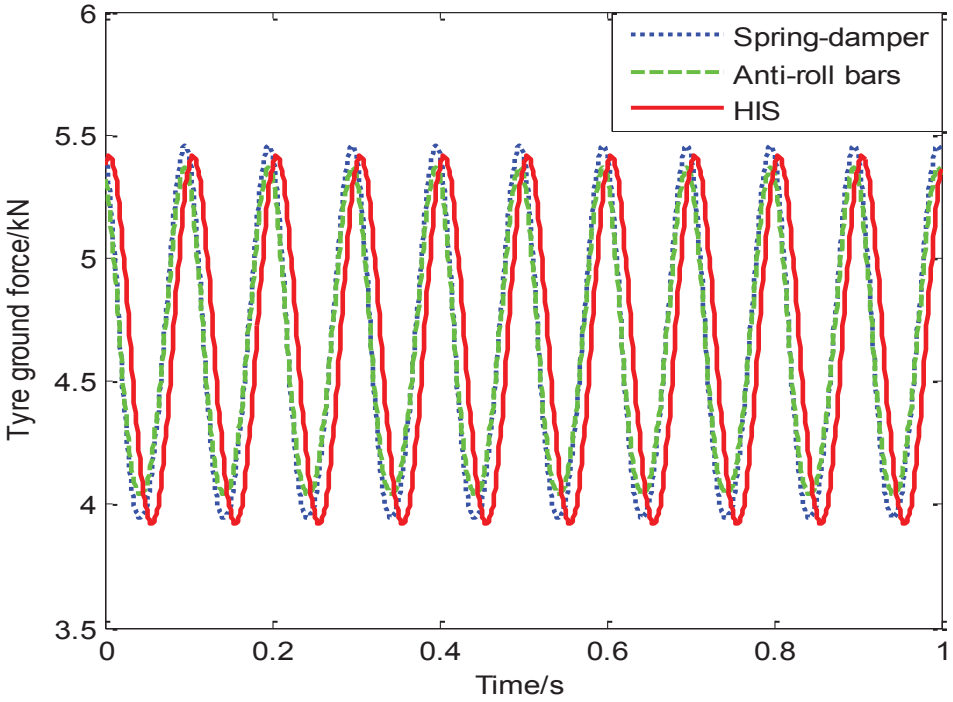

Figure 3.11 Tyre force at rear left in simulation under 3 mm and 10 Hz road input

The frequency of 10 Hz is equivalent to a speed of 43 kilometres per hour if the wavelength of the road surface is 1.2 metres and the wheelbase of the vehicle is 3 metres. When equipped with anti-roll bars, the tyre force variations decrease by 26% at the front and 12% at the rear. The tyre force variations of the test vehicle with the HIS are similar with the benchmark, with reductions of 5% and 1% at the front and rear respectively. As can be seen from the simulation results, when the vehicle speed is relatively high, the vehicle with anti-roll bars shows slightly better road holding performance than the other two configurations.

3.5.2.4 Single wheel hop with a 50 mm bump

In the simulation of the single wheel hop, the front left wheel is forced to move up and down with a 50 mm bump, as shown in Figure 3.3.

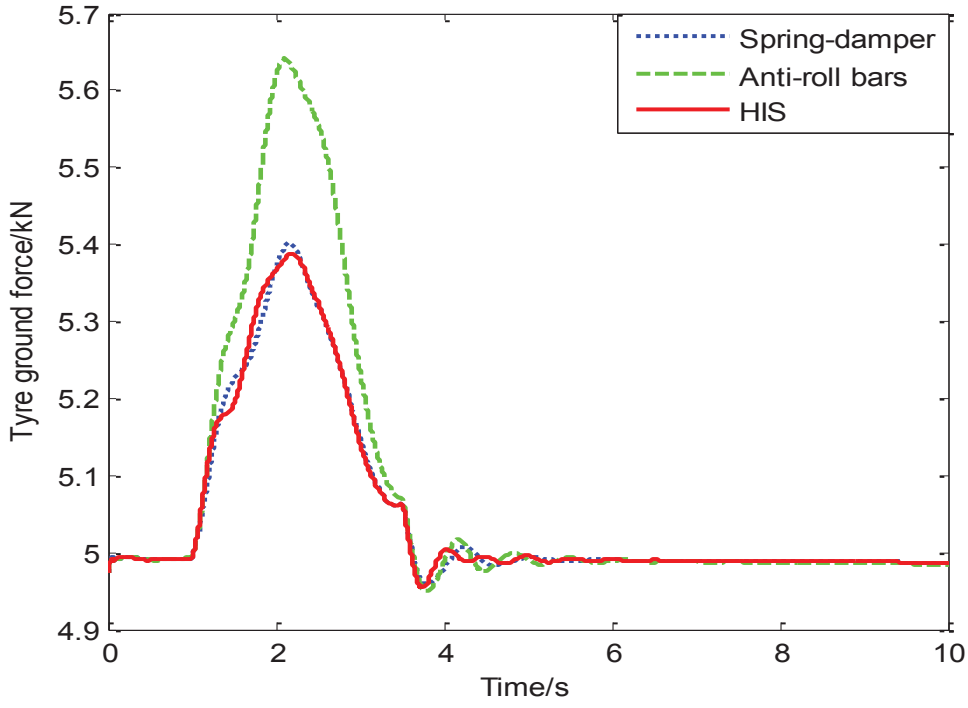

Figure 3.12 Bump response of the tyre force at the front left in the simulation

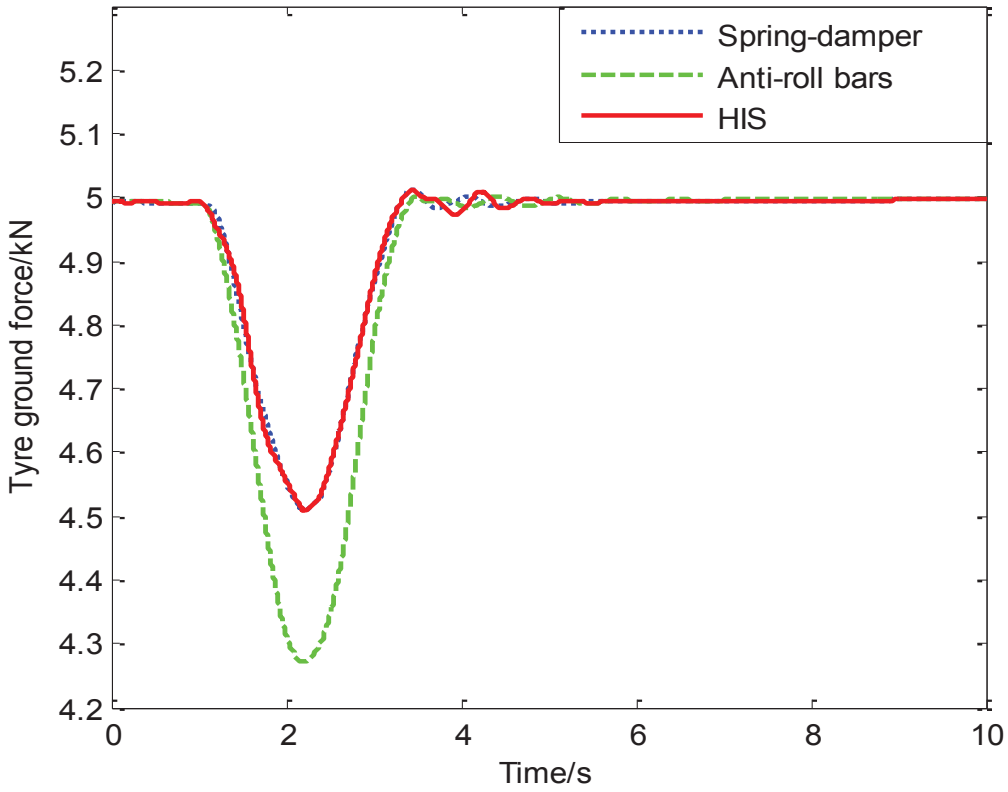

Figure 3.13 Bump response of the tyre force at the front right in the simulation

The frequency is equivalent to a speed of 5 kilometres per hour if the width of the bump is 3 metres. The other wheels are freely standing on the ground with no external inputs. The bump responses of the front left and front right tyres are compared in Figure 3.12 and Figure 3.13. As can be seen from the results, the tyre force variations substantially increase with the anti-roll bars (56% and 45% raises at the front left and rear right than the benchmark), but the HIS shows almost the same performance as the conventional suspension. The results indicate that when vehicles are under single wheel hop excitations, the tyre-ground force distributions of the vehicle with anti-roll bars are more uneven than those of other two configurations.

3.6 Experiments

3.6.1 Test conditions and setup

For the validation of the simulation results, a set of tests has been done on a four-post test rig with a typical SUV. Experimental implementations need to remove the anti-roll bars from the vehicle and then install the specifically designed HIS system on the SUV. The hydraulic accumulators of the HIS system need to be pre-charged with nitrogen to a specific working pressure. The higher the pre-charged pressure, the greater the roll stiffness induced by the HIS system, and vice versa. In this test, the accumulators are pre-charged with 1 Mpa pressure and the system working pressure is set as 3 Mpa when carrying out the test.

The vehicle responses have been obtained under four sets of different road excitations, which are in agreement with the road excitations in the simulations. Tyre loads are measured by the four load cells mounted on the four wheel plates of the four-post test rig. Moreover, a two-axis gyroscope is installed at the vehicle's CG between the two front seats to measure roll and pitch angular velocity. The data from sensors are logged by a National Instruments acquisition system (USB-6343 X-series) in conjunction with LABView.

3.6.2 Test rig

The suspension test rig consists of four independently controlled servo actuators powered by a large hydraulic power unit. The photo of the 4-post test rig with the testing vehicle is shown in Figure 3.14 and the motor-pump power unit of the test rig is shown in Figure 3.15. The actuators are positioned and fixed according to the vehicle's wheelbase and track. Each wheel sits on a suitable wheel plate that is mounted to the actuator's piston rod. The wheel

plates feature guard rails to restrain the wheels laterally, but the wheels are not restrained in the vertical direction. These constraint conditions are suitable for the data logging of the tyre load variations.

Figure 3.14 Four-post test rig and test vehicle

Figure 3.15 Motor-pump power unit of the test rig

The four-post system's operating limitations are as follows:

Table 3.5 Four-post test rig specifications

Vehicle weight (max.)	3000kg
Wheel base adjustment range	2450 - 2890 mm
Tack width adjustment range	1460 – 1720 mm
Actuator:	
Amplitude (max.)	± 80 mm
Frequency (max.)	35 Hz
Force (rated max.)	± 40 kN
Acceleration (max.)	20 g
Velocity (max.)	0.8 m/s
Typical unsprung mass(per actuator)	75kg
Base mount	independent x-y positioning mechanism for easy adjustment of track width and wheel base
Wheel pan	rectangular design for easy roll-on; safety skirt to prevent vehicle roll-off; provision for load cell
Control system:	
Servo controller	Roll and bounce modes; independent excitation

3.6.3 HIS mounting

Both the HIS and the active HIS systems are mounted on the test vehicle for this research. The details of the HIS mounting are shown in Figure 3.16, where Figure 3.16(a)-(d) illustrated the mounted front and rear hydraulic cylinders, left and right accumulators respectively. The active HIS mounting and the details of the control unit will be introduced in Chapter 4. The hydraulic cylinders of the HIS are mounted between the wheels and chassis of the test vehicle, and they are parallel with the original coil springs. At the front wheel stations, the cylinder bodies are mounted to the vehicle chassis at the top and hinge jointed to the control arm at the bottom, as shown in Figure 3.16(a). The overall stroke of

the cylinders matches the suspension travel, and the mounting location of the cylinder does not affect the wheel turning. At the rear wheel stations, the cylinders pivot the vehicle body, while the cylinder rod ends hinge joint to the lower control arm of the wishbone suspension, as shown in Figure 3.16(b).

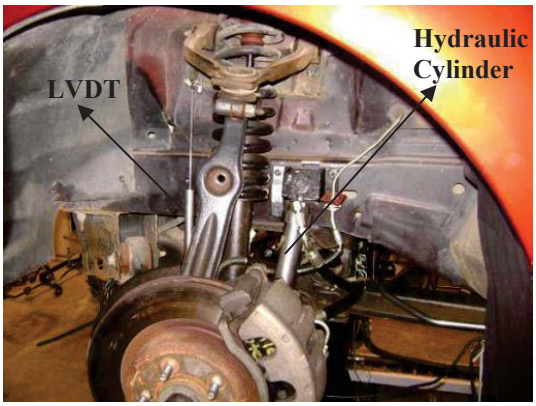

(a) Front wheel hydraulic cylinder

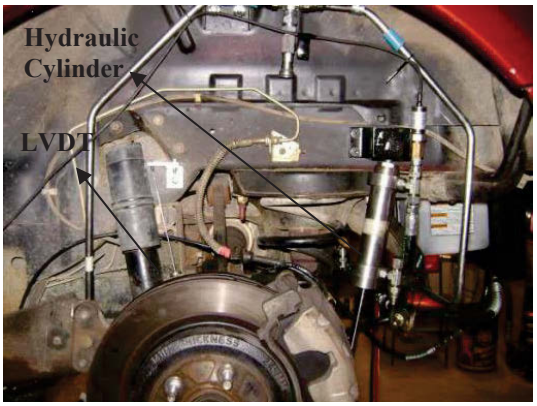

(b) Rear wheel hydraulic cylinder

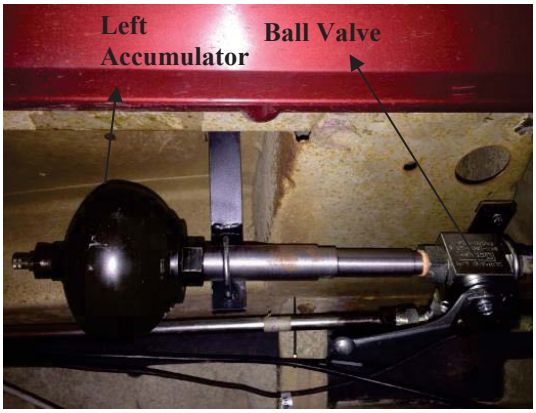

(c) Left accumulator

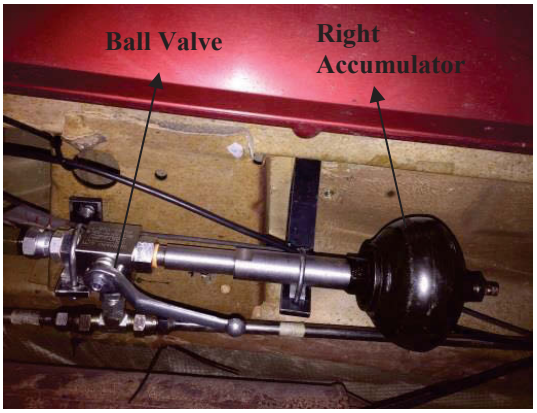

(d) Right accumulator

Figure 3.16 HIS installation

Flexible hoses are used to connect the inlets/outlets of the four cylinders to the rigid piping system to allow free movement of the cylinders. The hydraulic piping system is placed underneath the vehicle chassis, interconnecting the hydraulic cylinders into two circuits according to the schematic diagram in Figure 2.1. Each circuit employs a hydraulic

accumulator for adjusting the roll stiffness [115]. Two hydraulic accumulators are placed at the left and right side underneath the vehicle body and supported by brackets, as show in Figure 3.16(c) and Figure 3.16(d). As can been seen from Figure 3.16(c) and Figure 3.16(d), two three-way ball valves are employed in the test rig, which enable the switching between the HIS and the active HIS. When the hydraulic circuits are connected to the accumulators, the HIS is ready for working. While they are connected to the control unit, the active HIS is ready to run.

3.6.4 Sensors and data acquisition system

The data are acquired from 14 mounted sensors that can cover most aspects of the vehicle dynamics. Low-cost load cells are adopted in this experiment. As mentioned before, they are mounted on the wheel plates of the four-post test rig, as shown in Figure 3.17.

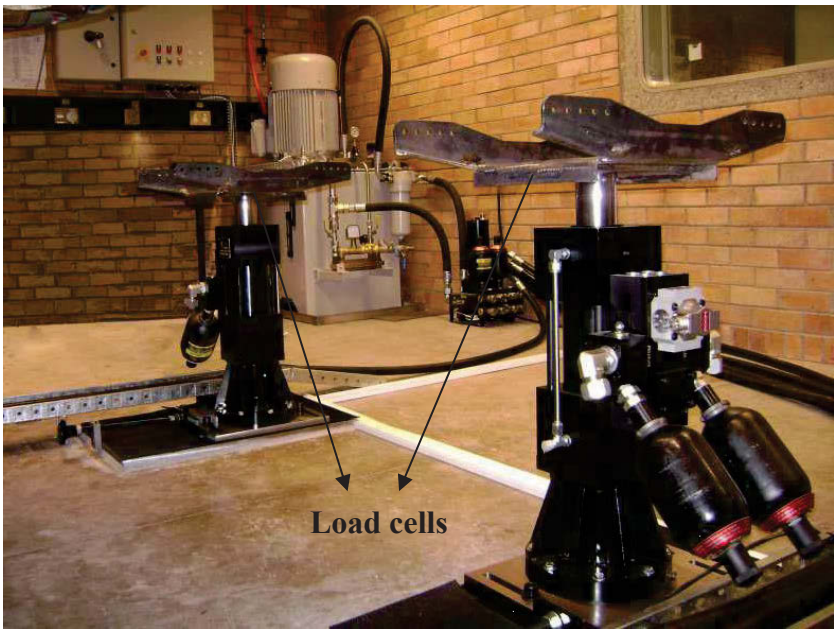

Figure 3.17 Mounted load cells

The specifications of all the mounted sensors are shown in Table 3.6. NI data acquisition system and Labview are used to log the data. The sensor power board is able to power up to 20 sensors, and the NI data acquisition board can host 32 analogy input channels.

Table 3.6 Specifications of the mounted sensors

Code	Category	Mounted position	Quantity
500Kg*4	Load cell	Test rig plates	4
HP_24DCTC	LVDT	Rear wheels	2
HP_7DCTC	LVDT	Front wheels	2
AST4000C	Pressure transducer	Inside cylinders	2
MMA7361L	Acceleration sensor	Mass center	2
LPY503AL	Two-axis Gyrometer	Mass center	2

3.6.5 Experimental results

3.6.5.1 Sinusoidal warp road excitations with 50 mm amplitude and 0.2 Hz frequency

The experimental results in the first set of tests agree well with the simulation results. As illustrated in Figure 3.18 and Figure 3.19, the tyre-ground forces of the conventional spring-damper suspension and the HIS are almost the same. The amplitude is around 4 kN at the front and 3 kN at the rear. The difference between the front and rear tyre force variations is mainly due to the difference of the spring stiffness and load distributions at the front and rear of the vehicle. Normally the front coil spring is softer than the rear spring, and the CG of the vehicle is closer to the front axle. When the car is installed with anti-roll bars and tested with the same ground input, the variations of the tire forces are raised by 49% and 50% compared to those of the vehicle with spring-damper only at the front and rear respectively.

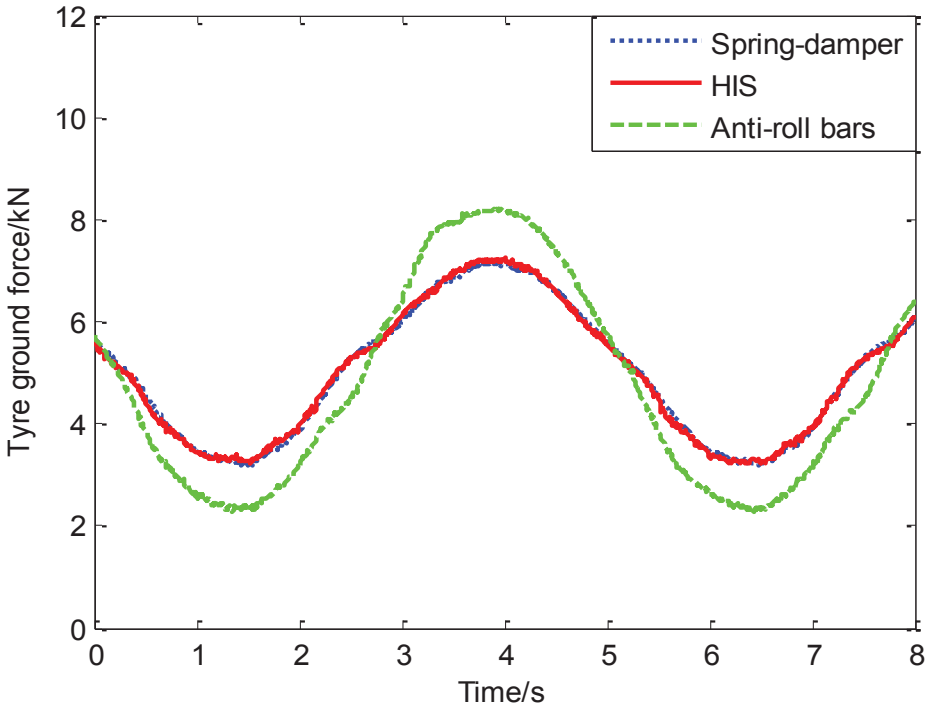

Figure 3.18 Measured tyre force at front right under 50mm and 0.2Hz road input

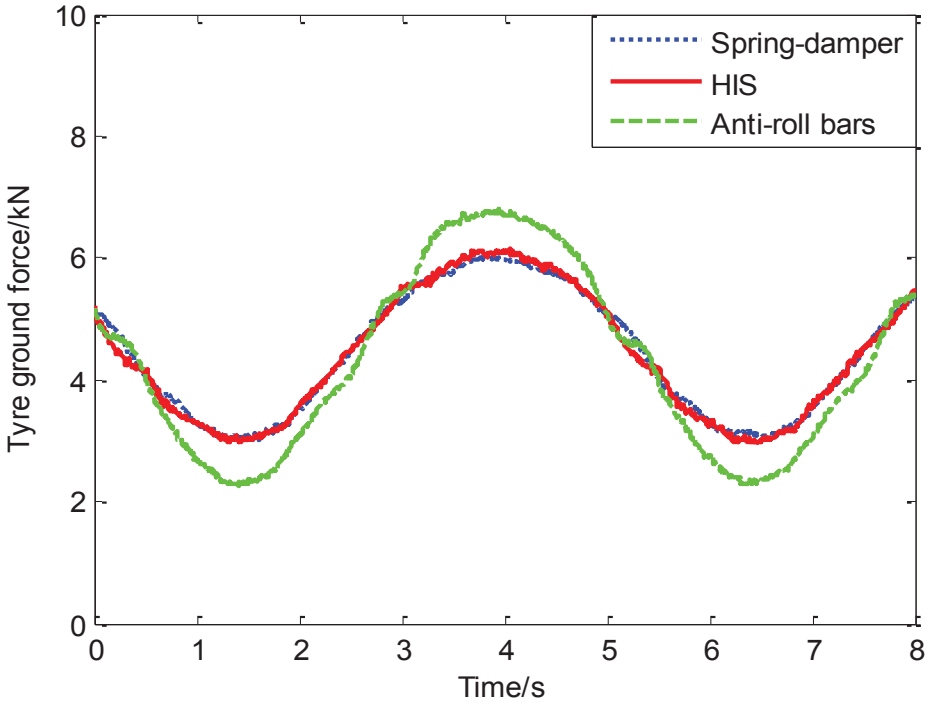

Figure 3.19 Measured tyre force at rear left under 50mm and 0.2Hz road input

From the well-matched simulation and experiment results in the first set of tests, it is demonstrated that under ground excitations with low frequency, the anti-roll bars weaken the road holding ability of the vehicle, but the HIS has almost no influence. It can be also seen that when the vehicle speed is low, the damping effect of the HIS is almost negligible, so the vehicle with the HIS behaves almost the same as the vehicle without additional roll stiffness, i.e. with neither anti-roll bars nor the HIS.

The test results of the roll and pitch angular velocities of the vehicle body are shown in Figure 3.20 and Figure 3.21. It can be seen from Figure 3.20 that the tendency of the roll rate is similar to the simulation results, the curve of the HIS is in phase with that of the conventional suspension, but the curve of the anti-roll bars is out of phase with them.

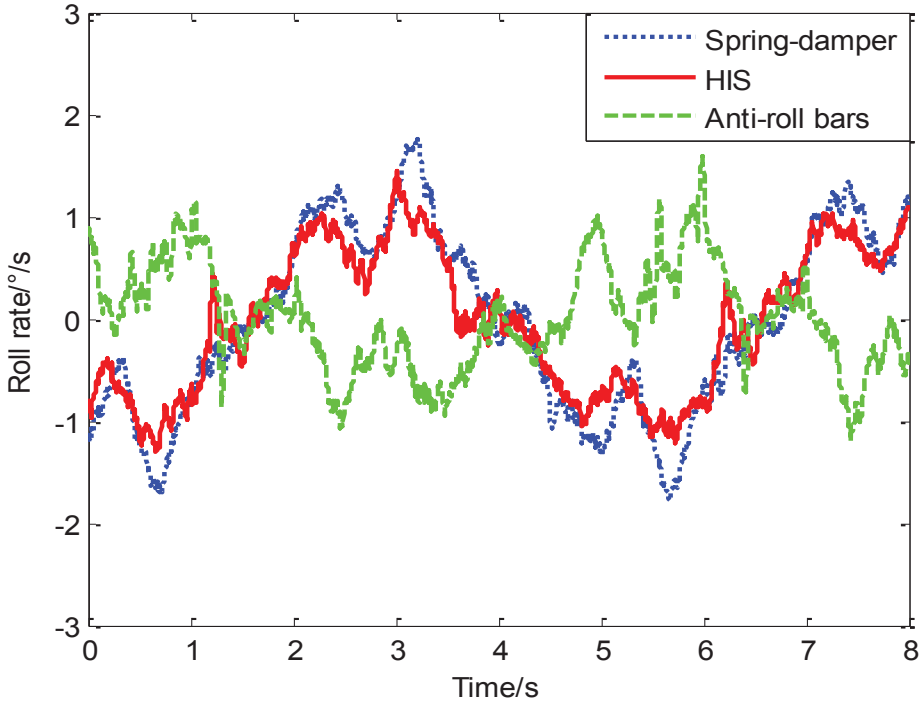

Figure 3.20 Measured roll angular velocity at centre of gravity

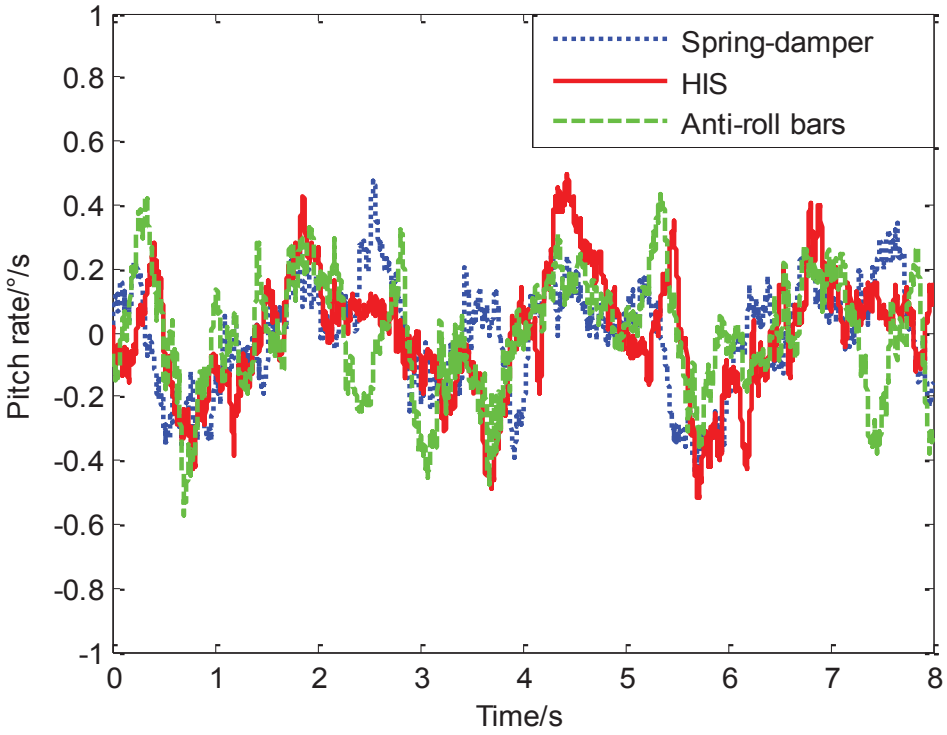

Figure 3.21 Measured pitch angular velocity at CG

As mentioned before, it is caused by the employment of the front and rear anti-roll bars with different stiffness. However, due to the system simplification in the modelling, the test results show obvious distinguishing features from simulation results. From Figure 3.20, it can be seen that there are two peaks at each wave trough and crest of the data curves caused by motion interference while the curves are smoother in the simulation. The reason is that the vehicle body is regarded as a rigid body in the simulation so that the stiffness effect of the chassis is ignored. This is also the reason that the amplitudes of the roll and pitch angular velocities in the experiment are larger than in the simulation.

In Figure 3.20, the responses of the vehicle with the HIS are smaller than for the vehicle with conventional suspension, with a reduction of 22% at the peak. When the test vehicle

was equipped with anti-roll bars, the roll rate also decreases by 21%. The pitch rates of the three configurations are similar as shown in Figure 3.21. As discussed before, the pitch rates are ignorable because their amplitudes are much smaller than those of the roll rates when considering the ride comfort. From both the simulation and experiment results, it can be seen that the HIS does not worsen the ride comfort of the test vehicle.

3.6.5.2 Sinusoidal warp road excitations with 10 mm amplitude and 1 Hz frequency

The comparison of the tyre loads under the warp with 10 mm amplitude and 1 Hz frequency are presented in Figure 3.22 and Figure 3.23. It can be seen that the test results are similar to the simulation results. With the anti-roll bars, the tyre forces increase by 63% and 30% at the front and rear wheels respectively, but the employment of the roll-plan HIS does not affect the tire variations much, with 35% and 17% increase at the front and rear. From the simulation and experiment results, it can be seen that as the frequency of the road excitations rise to 1 Hz, the road holding ability of the test vehicle with the HIS is still better than that of the vehicle with anti-roll bars. When the vehicle speed is not low, the damping effect of the HIS is obvious. It brings negative impact to the vehicle's road holding ability although less than that brought by the anti-roll bars. However, since the inlets/outlets of the hydraulic cylinders are designed with a very small size (with a diameter of 8 mm only), which bring about the majority of the damping effect, the performance of the HIS can be improved by redesigning the inlets/outlets of the hydraulic cylinders.

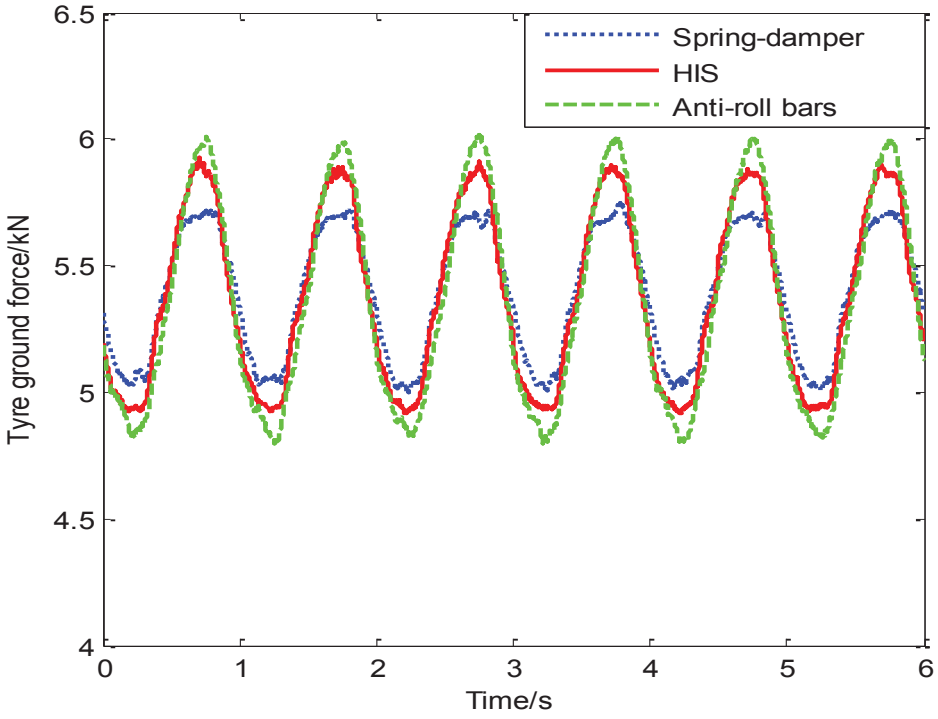

Figure 3.22 Measured tyre force at front right under 10 mm and 1Hz road input

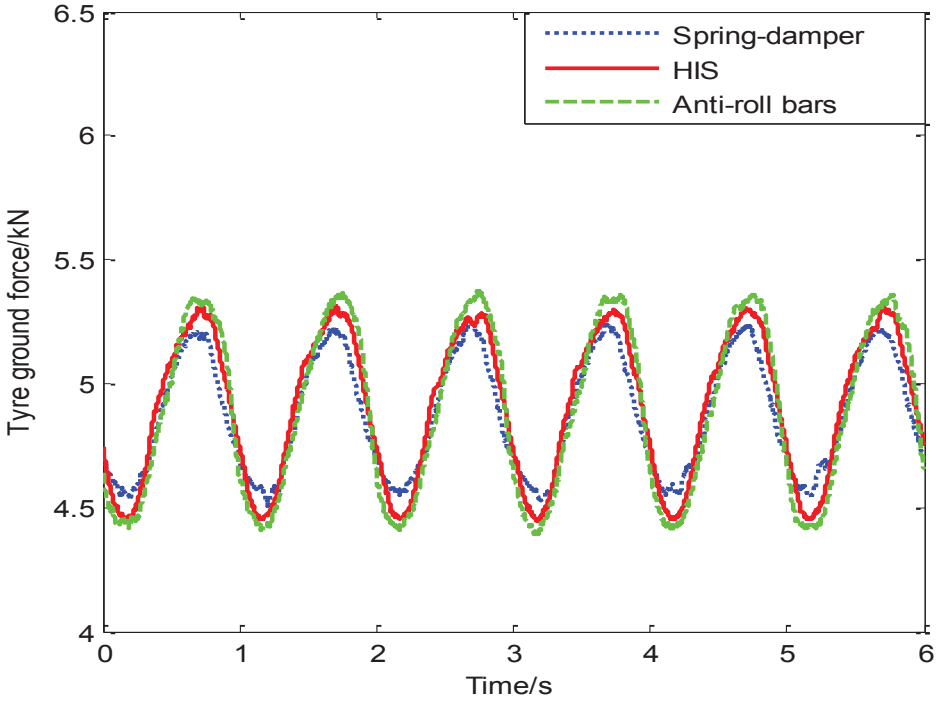

Figure 3.23 Measured tyre force at rear left under 10 mm and 1Hz road input

3.6.5.3 Sinusoidal warp road excitations with 3 mm amplitude and 10 Hz frequency

The experimental comparison of the tyre forces under 10 Hz and 3 mm warp excitations are shown in Figure 3.24 and Figure 3.25. It can be seen that the responses of the anti-roll bars are similar to the simulation, with 15% and 9% reductions compared to the vehicle with spring-damper only at the front and rear respectively. However, the responses of the HIS are different from the simulation, with an increase of 34% at the front but with a decrease of 9% at the rear compared with the benchmark. This difference is mainly induced by the linearized HIS system model, which is not able to accurately describe the nonlinear factors of the hydraulic system, such as piston frictions and nonlinear damping. When the vehicle speed is relatively high, the damping effect of the HIS is very obvious.

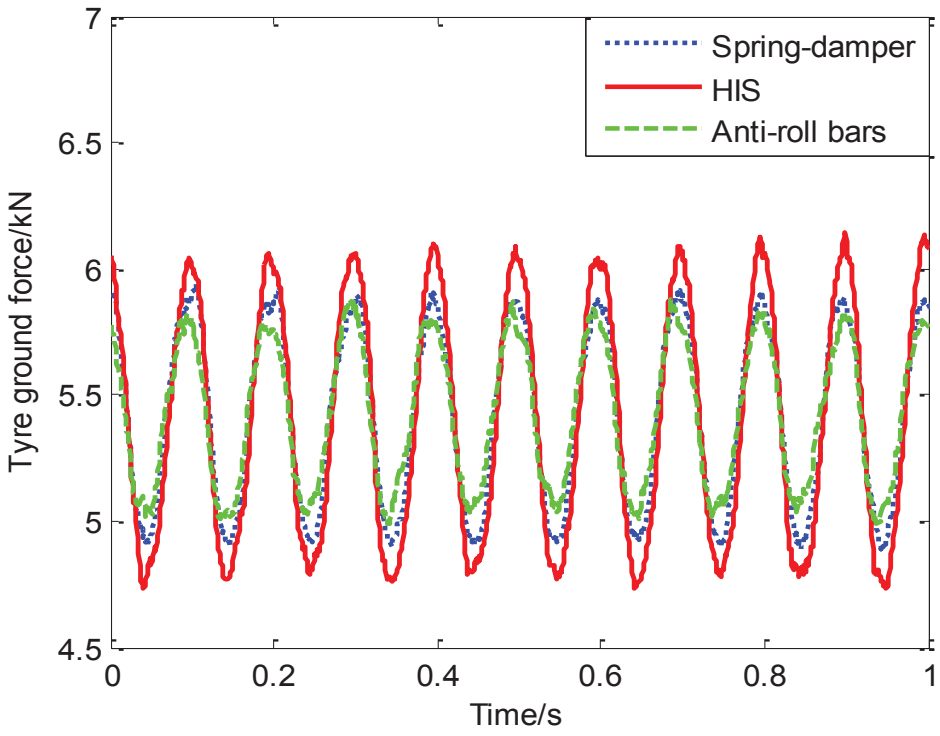

Figure 3.24 Measured tyre force at front right with 3mm and 10Hz road input

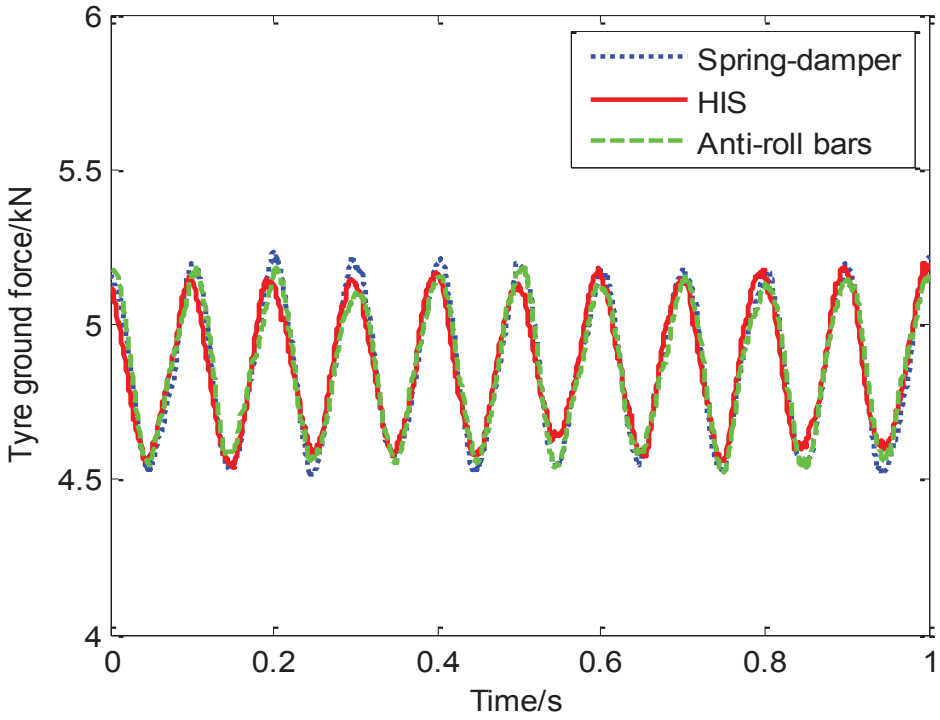

Figure 3.25 Measured tyre force at rear left with 3mm and 10Hz road input

However, since the tyre force variations are not large under this kind of road excitations, the wheels of the vehicle are not vulnerable to losing contact with the ground. As mentioned above, the performance of the HIS can be improved by enlarging the inlets/outlets of the hydraulic cylinders. It also can be seen that because of the flexibility of the vehicle body, the differences between the front and rear tyre force variations become more obvious at relatively high frequency.

The experimental results show that under 10 Hz warp excitations, the front tyre load variations of the test vehicle increase slightly with the roll-plane HIS. However, because generally the variations of the tyre load at high frequencies are much smaller than those at low frequencies (e.g. approximately 1kN at 10 Hz and 6kN at 0.2 HZ). Moreover, the off-

road driving is always along with a relatively low speed. Hence, the influence of the roll-plan HIS at high frequency is ignorable when considering the road holding ability of the vehicle.

3.6.5.4 Single wheel hop with a 50mm bump

The experimental bump responses of the front left and front right tyres are compared in Figure 24 and Figure 25. It can be seen that the HIS raises the tyre load variations gently with 23% and 22% at the front left and front right tyres respectively. However, in comparison with the benchmark, the tyre forces of the vehicle with anti-roll bars increase significantly by 115% and 85% at the front left and front right.

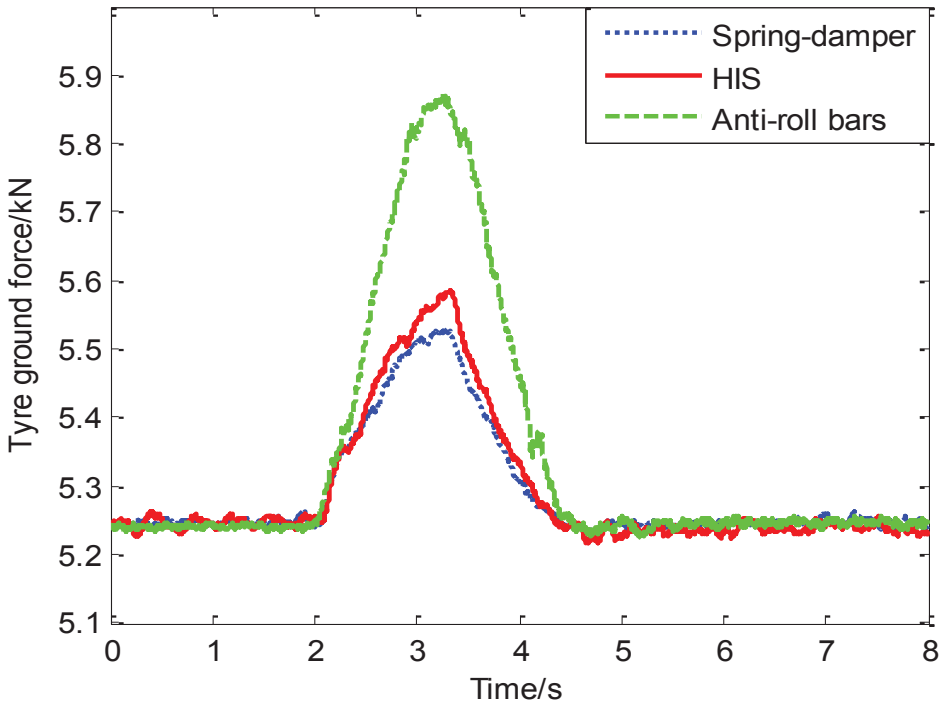

Figure 3.26 Measured tyre force at the front left with a bump road input

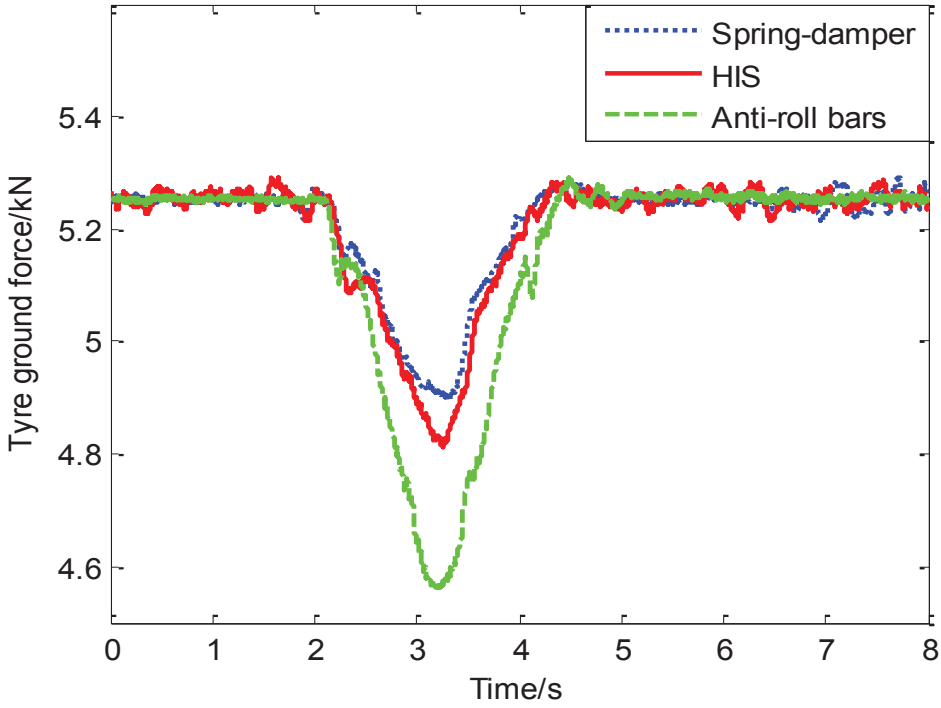

Figure 3.27 Measured tyre force at the front right with a bump road input

As the bump is not an excitation with the pure warp mode, the HIS will provide additional roll stiffness when the vehicle encounter a bump, which leads to the change of the tyre forces compared with the benchmark. However, the road holding performance of the HIS is still better than the anti-roll bars. In other words, when one wheel of the vehicle with anti-roll bars is excited by a large bump, the wheel on the other side is more likely to lose contact with the ground, which will result in loss of the traction and stability of the vehicle.

3.7 Summary

This section presents an investigation into the road holding performance of the vehicles fitted with conventional anti-roll bars and the HIS respectively. Based on a typical SUV, the modelling and modal analysis are carried out, which are used to analyse the effects of the

HIS and anti-roll bars on different motion modes. The simulations of vehicles with the HIS and anti-roll bars are implemented under four specific sets of ground excitations. Their experimental validations are implemented on a four-post test rig.

Both the simulation and experiment results show that when the car is running under warp ground excitations with a low frequency and a large amplitude (e.g. 0.2 Hz and 50 mm), which is the usual situation of off-road driving, anti-roll bars significantly weaken the road holding ability of the vehicle. By contrast, the HIS system has a negligible effect on the road holding ability of the vehicle. From the comparison of the roll and pitch rates, it can be seen that the roll-plane HIS does not worsen the ride comfort of the vehicle. When the frequency of the road excitations is not very low (e.g. 1 Hz), anti-roll bars have an even large negative effect on the vehicle's road holding ability and the HIS also has an obvious negative damping effect on the vehicle's road holding ability, but the road holding performance of the test vehicle with the HIS is still better than that with the anti-roll bars. Although under warp excitations with a high frequency and a small amplitude (e.g. 10 Hz and 3 mm), the road holding performance of the HIS is not as good as anti-roll bars, it is not a typical off-road driving and the tyre load variations are small, so that the negative damping effect of the HIS at high frequency is negligible. Furthermore, the inlets/outlets of the hydraulic cylinders can be redesigned to be larger to reduce the damping effect. Under a ground excitation with complex motion modes, single wheel hop, the additional stiffness of the HIS has a small negative effect on the road holding performance, but it is much better than the anti-roll bars.

In summary, for vehicles in need of an enhanced roll stability to compensate for the high CG, as well as a strong off-road passage capability (e.g. military vehicle, large commercial vehicles, off-road vehicles, SUV and so forth), the roll-plane HIS system, as a potential replacement of anti-roll bars, is a very promising option.

4 The Study of the Active HIS with H∞ Control

4.1 Introduction and rationale

The ride and roll resistance performance of the HIS has been studied in previous research found in the literature and the road holding performance of the HIS has also been presented in Chapter 3. For further investigating the HIS system, development has advanced in this study to the active HIS system with a control unit added. The exploration of the active HIS for better anti-roll performance is presented in subsequent chapters. In this chapter, an attempt is made to validate the active HIS with an output feedback H∞ Controller experimentally.

As the H∞ control is a model-based control method, this chapter begins with system modelling. An empirical model of the active HIS equipped vehicle is adopted for the development of the H∞ controller. Then the designed controller is validated on a real car. The SUV that appeared in Chapter 3 is also used as the test vehicle and assembled with the developed active HIS system. Based on a real-time communication board, the control force is applied through the active HIS to stabilise the roll motion of the test vehicle. The test is performed on the full-scale 4-post test rig introduced in Chapter 3. Ground roll excitation is described as two out-of-phase displacement inputs acting on the left and right wheels. In this Chapter, three sets of ground excitations are used to stimulate the roll motion of the vehicle body.

4.2 Background

The active HIS, evolved from passive HIS systems, directly supplies restoring forces to the vehicle chassis. It differs itself from semi-active suspension, which can only consume the vehicle vibration energy passively by adjusting the viscous damping coefficient of the shock absorbers.

To counteract the vehicle body's roll motion induced by cornering, the active HIS needs to provide sufficient forces to the vehicle body, in order to negate the roll moment generated by the centrifugal force. From a mechanical point of view, the control to minimise roll angle during cornering (e.g., roll-free cornering) does not consume much energy of the active HIS, because only vertical forces vary while suspension deflection remains unchanged [116] and not much work has been done during this process.

The passive HIS system or anti-roll bars are also adequate in reducing vehicle roll angle during cornering. However, due to the increased roll stiffness, a vehicle's ride comfort is slightly compromised under ground excitations, in particular, the coherence of the excitations along the left and right tracks. In contrast, the active HIS is able to compensate for the road unevenness and minimise the vehicle body roll angle in a way that is superior to passive HIS. For the vehicle body levelling control under ground excitation, since the active HIS needs to do work to expand or compress actuators to achieve the desired suspension deflection, there will be energy consumption from its operation.

From the above discussion of the two control scenarios, the active suspension system can be very energy efficient in achieving the handling and safety-related objectives, but for

achieving a better ride performance (body levelling control), a certain amount of energy is required. So the overall energy management strategy for active suspension depends on how to balance ride comfort and handling related control objectives.

As discussed in Chapter 2, various control approaches have been applied to improve the performance of active suspensions. H∞ is recognised as one of the most robust and effective optimal control strategies. It was employed in active suspension control from the quarter-car model based, half-car based to full-car model based applications, but most of them were only studied by simulations. The experimental H∞ control implementation on a full-car level with a practical active suspension system is of great interest to extend the research on active suspensions into engineering practice. For the implementation of the controller on the real SUV, a primary H∞ output feedback controller is designed in this chapter.

4.3 Model description

The effectiveness and performance of the H∞ controller are largely determined by the mathematical modelling of the physical plant; thus an appropriate model and correct parameters of the active suspension (mainly the pressure control unit) are essential for this model-based optimal controller. The modelling has to be simple enough for the controller design and also has to capture the system dynamic characteristics.

4.3.1 Model estimation of active HIS

The pressure control unit includes a motor-pump set, an accumulator and a pressure control servo-valve, as well as a tank, a filter and other hydraulic fittings. The modelling and

parameter estimation of the active system are vital to the control performance of the model-based controllers, e.g., LQR and H∞ in this case. The way of individually modelling each element could be theoretically accurate and ideal, but nevertheless, the parameter values for this ideal model are very hard to be derived and the estimation method for these physical parameters is very much limited by available testing methods.

Without correct parameters, a complex model with a larger number of degrees of freedom makes less sense. Hence, an empirical modelling method [117] is used to estimate the hydraulic model and corresponding parameter values by testing the assembled active pressure control unit separately from the vehicle system. The setup for the testing is illustrated in Figure 4.1 and described as follows.

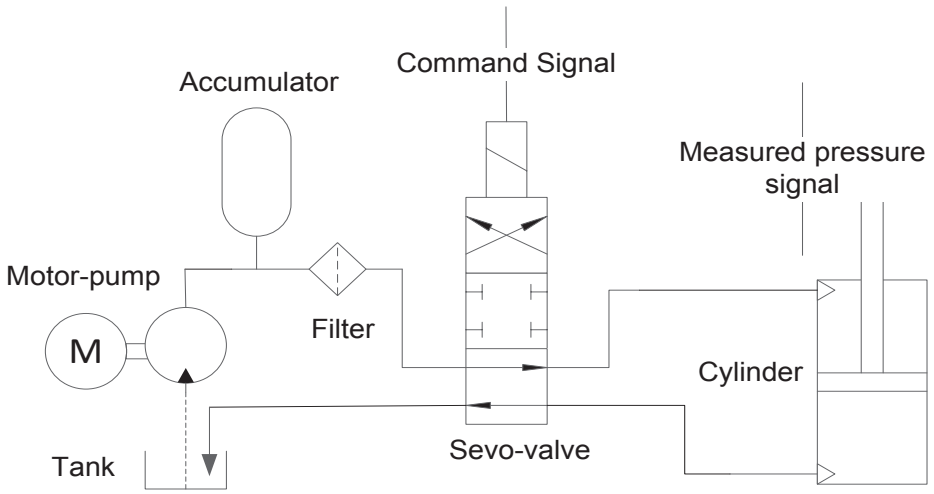

Figure 4.1 Schematic drawing of the testing setup

The output ports of the pressure control unit are connected to a double acting cylinder that is locked in a middle position. A pressure transducer is located at the port of the upper

cylinder chamber. The pressure command signal sent to the servo-valve is a sinusoidal signal at different frequencies, and the actual pressure measured at the cylinder port is acquired for comparison.

Both the command and measured signals are collected by a National Instruments data acquisition board. The differences between these signals regarding the magnitude and phase delay are calculated from the obtained results and plotted against the frequency, shown in Figure 4.2.

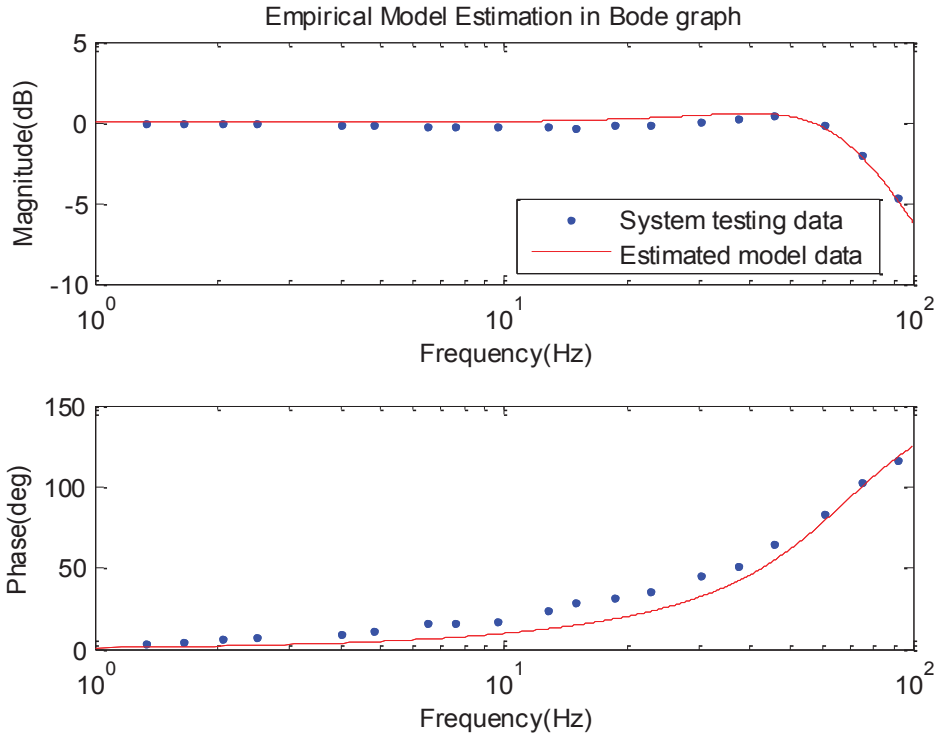

Figure 4.2 Empirical model estimation in Bode graph

From the plotted Bode graph in Figure 4.2, a second order system is considered sufficient to cover the main dynamic characteristics of the system, shown in Equation (4.1),

$$\frac{P(s)}{I(s)} = \frac{1}{1+(2\xi / w_n)s + s^2 / w_n^2}, \tag{4.1}$$

where P(s) represents the measured pressure signal, and *I(s)* is the input command signal. w_n is the natural frequency, ξ is the damping ratio; by curve fitting, the optimised value of w_n and ξ are estimated as 68 Hz, and 0.57,respectively. The estimated system frequency response is also shown by the solid line in Figure 4.2.

To be consistent with the vehicle modelling from previous work [118], the hydraulic system's transfer function needs to be converted into state-space form. The resulting state-space equation and system matrices are presented as

$$\begin{aligned} \dot{\mathbf{X}}_p &= \mathbf{A}_p \mathbf{X}_p + \mathbf{B}_p \mathbf{inp} \\ \mathbf{Y}_p &= \mathbf{C}_p \mathbf{X}_p + \mathbf{D}_p \mathbf{inp} \end{aligned}, \tag{4.2}$$

where

$$\mathbf{A}_p = \begin{bmatrix} -487.1 & -356.5 \\ 512 & 0 \end{bmatrix} \qquad \mathbf{B}_p = \begin{bmatrix} 16 \\ 0 \end{bmatrix}; \tag{4.3}$$
$$\mathbf{C}_p = \begin{bmatrix} 0 & 22.28 \end{bmatrix} \qquad \mathbf{D}_p = \begin{bmatrix} 0 \end{bmatrix}$$

inp is the pressure signal command to the pressure control unit; and $\mathbf{Y}_P$ is the actual pressure in the actuator.

4.3.2 Model integration

A model of smaller dimensions is preferable in the designing of advanced controllers, so the obtained hydraulic model is combined with a 4-DOF half-car model shown in Figure 4.3.

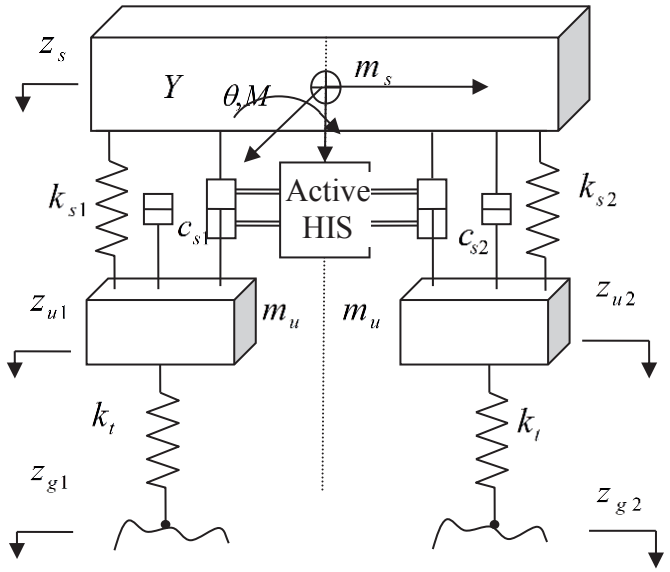

Figure 4.3 Half-car model integrated with active HIS

By defining the vehicle state vector $\mathbf{X}_c = \begin{bmatrix} \dot{\theta} & \dot{z}_s & \dot{z}_{u1} & \dot{z}_{u2} & \theta & z_s & z_{u1} & z_{u2} \end{bmatrix}^T$ and force vector $\mathbf{F} = \begin{bmatrix} w_1 & w_2 & f_1 & f_2 \end{bmatrix}^T$, where $w_{1,2}$ are the road input, and $f_{1,2}$ are the control forces applied by the two actuators shown in the half-car model, we have system equations of the half-car model in the state-space form

$$\dot{\mathbf{X}}_c = \mathbf{A}_c \mathbf{X}_c + \mathbf{B}_c \mathbf{F}, \tag{4.4}$$

and the system matrices are defined as

$$\mathbf{A}_c = \begin{bmatrix} \mathbf{0} & \mathbf{I} \\ -\mathbf{M}^{-1}\mathbf{K} & -\mathbf{M}^{-1}\mathbf{C} \end{bmatrix}_{8\times 8} \qquad \mathbf{B}_c = \begin{bmatrix} 0 & 0 \\ \mathbf{B}_{road} & \mathbf{B}_{contr} \end{bmatrix}_{8\times 4}^T, \tag{4.5}$$

where

$$\mathbf{M}=\begin{bmatrix} I & 0 & 0 & 0 \\ 0 & m_s & 0 & 0 \\ 0 & 0 & m_u & 0 \\ 0 & 0 & 0 & m_u \end{bmatrix} \qquad \mathbf{C}=\begin{bmatrix} 2l^2c_s & 0 & -lc_s & lc_s \\ 0 & 2c_s & -c_s & -c_s \\ -lc_s & -c_s & c_s & 0 \\ lc_s & -c_s & 0 & c_s \end{bmatrix}$$

$$\mathbf{K}=\begin{bmatrix} 2l^2k_s & 0 & -lk_s & lk_s \\ 0 & 2k_s & -k_s & -k_s \\ -lk_s & -k_s & k_s+k_t & 0 \\ lk_s & -k_s & 0 & k_s+k_t \end{bmatrix} \quad . \qquad (4.6)$$

$$\mathbf{B}_{road}=\begin{bmatrix} 0 & 0 \\ 0 & 0 \\ k_t/m_u & 0 \\ 0 & k_t/m_u \end{bmatrix}_{4\times 2} \qquad \mathbf{B}_{contr}=\begin{bmatrix} l/I & -l/I \\ 1/m & 1/m \\ -1/m_u & 0 \\ 0 & -1/m_u \end{bmatrix}_{4\times 2}$$

Now we can integrate the derived hydraulic model with this half-car model and derive the combined system model in state-space by defining the state vector as $\mathbf{X}=\begin{bmatrix}\dot{\theta} & \dot{z}_s & \dot{z}_{u1} & \dot{z}_{u2} & \theta & z_s & z_{u1} & z_{u2} & x_{p1} & x_{p2}\end{bmatrix}^T$, and input vector as $\mathbf{u}=\begin{bmatrix}w_1 & w_2 & p\end{bmatrix}^T$,

$$\dot{\mathbf{X}}=\mathbf{A}\mathbf{X}+\mathbf{B}\mathbf{u}\,. \qquad (4.7)$$

The system metrics are defined as follow

$$\mathbf{A}=\begin{bmatrix} -\mathbf{M}^{-1}\mathbf{C} & -\mathbf{M}^{-1}\mathbf{K} & \mathbf{B}_{contr}\begin{bmatrix}\mathbf{C}_p a \\ -\mathbf{C}_p a\end{bmatrix} \\ \mathbf{I} & \mathbf{0} & \mathbf{0} \\ \mathbf{0} & \mathbf{0} & \mathbf{A}_p \end{bmatrix}_{10\times 10} \qquad \mathbf{B}=\begin{bmatrix} \mathbf{B}_{road} & 0 \\ 0 & 0 \\ 0 & \mathbf{B}_p \end{bmatrix}_{10\times 3}, \qquad (4.8)$$

$\mathbf{B}_p$ is the excitation form the bump, please refers to Equation (4.9); $\mathbf{B}_{road}$ is the excitation from ground; a is the piston area with the assumption that the cylinder has equal piston area in both chambers to simplify the system model.

4.4 Output feedback H∞ controller design

A basic H∞ controller is designed based on the combined system model that contains the dynamics of the active suspension. The sprung mass roll angle is set as the feedback signal and also the control target. As shown in the control diagram in Figure 4.4, road excitation *d* is the external input to the vehicle fitted with the active suspension; body roll angle *y* is the feedback signal for the H∞ controller; and pressure control command signal P_a is the output signal from the controller.

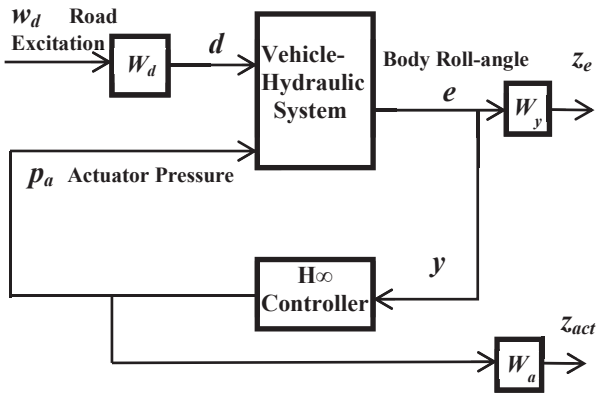

Figure 4.4 Block diagram of the designed H∞ control

The objective of the H∞ algorithm is to minimise the roll angle of the vehicle body *e*. If **V** represents the system matrix of the integrated model and **K** represents the controller, the system can be expressed as

$$\begin{bmatrix} e \\ y \end{bmatrix} = \mathbf{V}(s)\begin{bmatrix} d \\ p_a \end{bmatrix} = \begin{bmatrix} \mathbf{V}_{ed}(s) & \mathbf{V}_{eF}(s) \\ \mathbf{V}_{yd}(s) & \mathbf{V}_{yF}(s) \end{bmatrix}\begin{bmatrix} d \\ p_a \end{bmatrix}, \tag{4.10}$$

$$p_a = \mathbf{K}(s)y\,. \tag{4.11}$$

The H∞ controller can minimise the H∞ norm of the transfer function matrix $\mathbf{H}_{ed}$ to stabilise the system,

$$\min_{K \in K_S} \left\| \mathbf{H}_{ed} \right\|_{\infty} . \tag{4.12}$$

From Equations (4.10) and (4.11), we obtain

$$e = \mathbf{H}_{ed}(\mathbf{V}, \mathbf{K}) d , \tag{4.13}$$

where [119]

$$\mathbf{H}_{ed}(\mathbf{V}, \mathbf{K}) = \mathbf{V}_{ed} + \mathbf{V}_{eF}\mathbf{K}(\mathbf{I} - \mathbf{V}_{yF}\mathbf{K})^{-1}\mathbf{V}_{yd} . \tag{4.14}$$

In H∞ derivation, weighting functions are necessary to be employed to optimise the distribution of the control resource over the excitations. W_{d1} and W_{d2} are weighting functions of the ground excitation to the left and right wheels. The low-frequency contents are more significant than the high-frequency signals. In this design, a 10Hz low-pass filter is obtained and tuned from the model-based simulation in MATLAB and is verified in experiments. It is described by Equation (4.15) and (4.16), and its Bode graph is shown in Figure 4.5.

$$W_{d1} = 0.01\left(\frac{62.83}{s + 62.83} \right) \tag{4.15}$$

$$W_{d2} = 0.01\left(\frac{62.83}{s + 62.83} \right) \tag{4.16}$$

$$W_d = \begin{bmatrix} W_{d1} \\ W_{d2} \end{bmatrix} \tag{4.17}$$

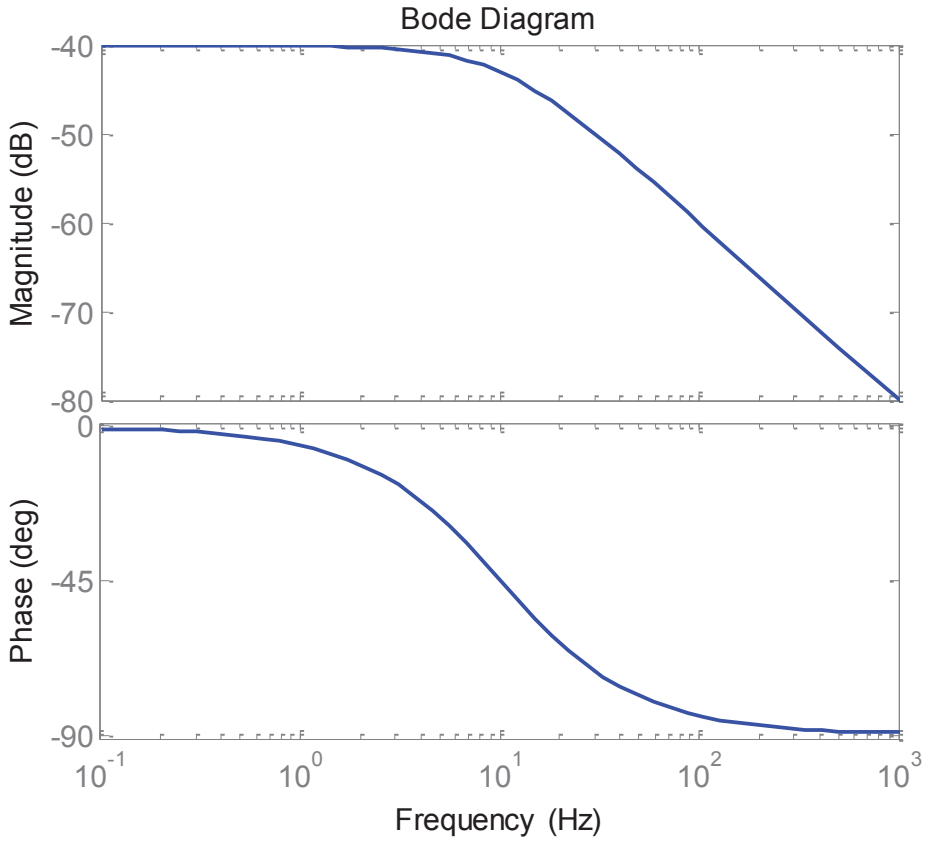

Figure 4.5 Weighting functions of the ground excitation W_{d1} and W_{d2}

W_y is the measured output weighting function determined by the control strategy that highlights the controlled frequency range of the vehicle motions. Since the active HIS is targeting the large motions associated with the vehicle body that are in the low-frequency range, the W_y in Equation (4.18) is applied to roll angle measurement. The Bode graph of the W_y is presented in Figure 4.6.

$$W_y = 30\left(\frac{31.42}{s+31.42}\right) \tag{4.18}$$

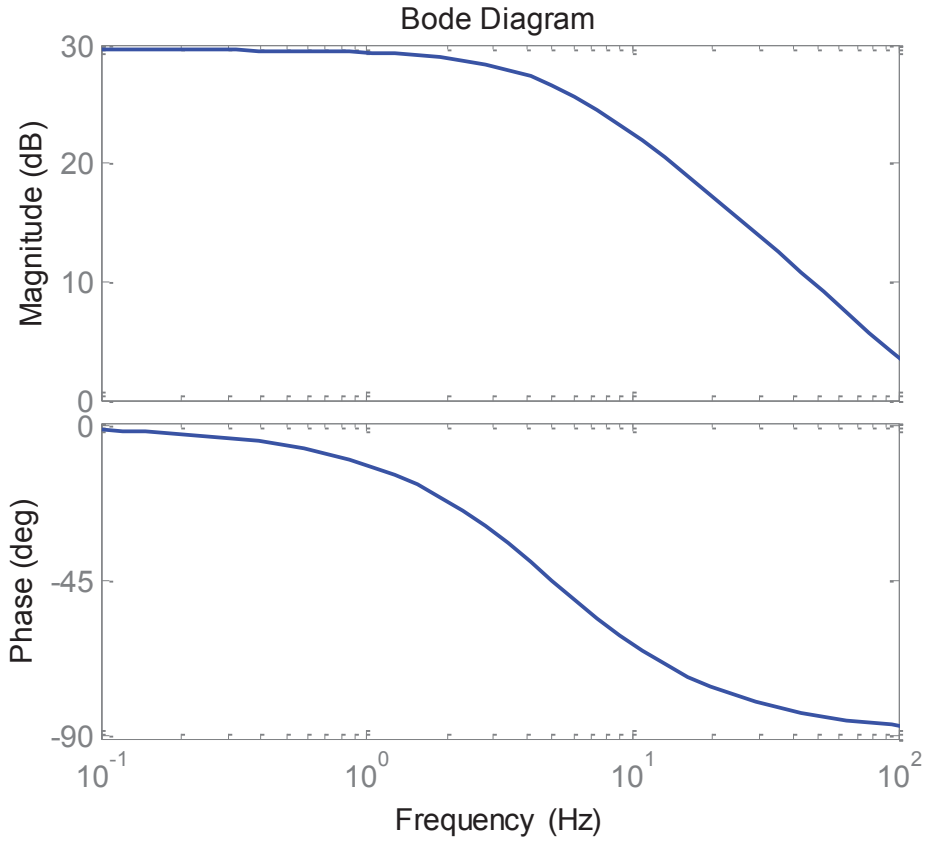

Figure 4.6 Weighting functions of measurement output W_y

W_{act} is the measured output weighting function, which is related to actuator response frequency. Due to the electrohydraulic system employed in the active suspension, the expected working frequency band is limited by the servo-valve response frequency, which is approximately 80Hz in this case. Command signal in higher frequency range will induce larger phases shift and may cause oscillation or even instability. Hence, the control forces have to be decreased in the higher frequency range. W_{act} in Equation (4.19) can reduce the effect of the control force in a high-frequency domain, and is derived in simulation, tuned and verified in testing. The Bode graph of the W_{act} is presented in Figure 4.7.

$$W_{act} = \frac{0.05}{13}\left(\frac{s+50}{s+500}\right) \tag{4.19}$$

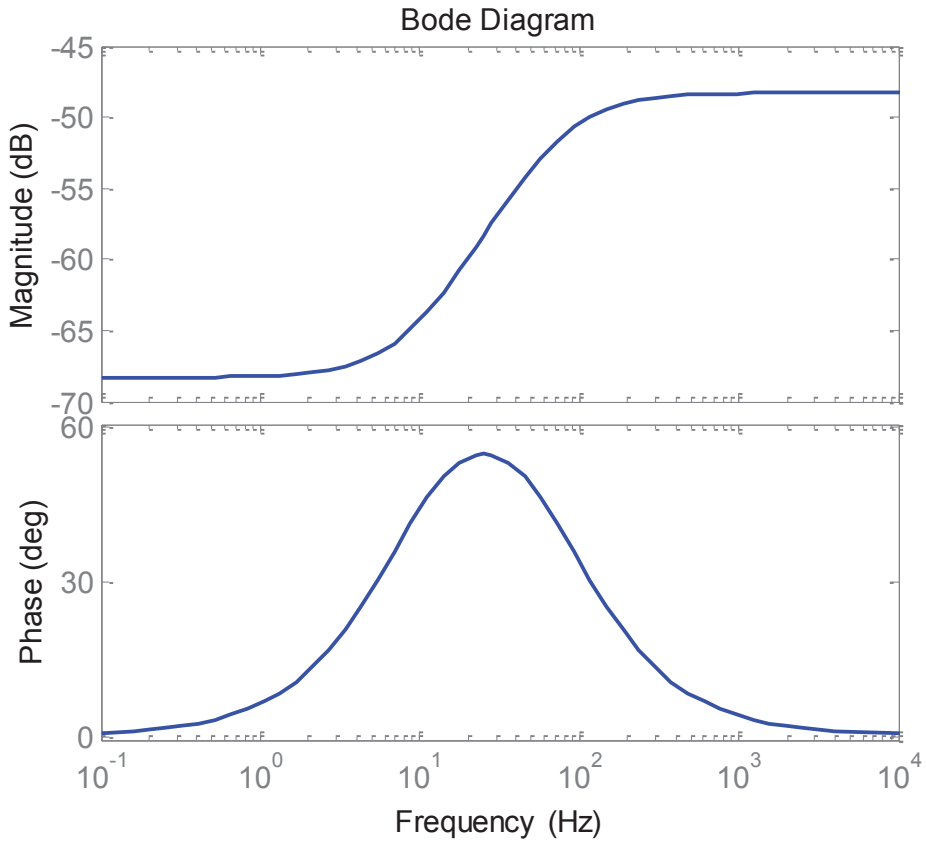

Figure 4.7 Variation of weighting functions of the actuator control force W_{act}

4.5 Experiments

4.5.1 Experimental instrument and conditions

The pressure control unit mentioned in Chapter 2 is assembled and mounted underneath the vehicle chassis, as shown in Figure 4.8. The obtained H∞ controller in MATLAB is applied to the test vehicle that is fitted with active HIS through a real-time communication board shown in Figure 4.9. The board conveys communication between Simulink on a computer

and the hardware of the test rig. This setup saves the time of controller tuning and accelerates the controller development cycle. The experiments are also conducted on the full-scale 4-post test rig, which is shown in Figure 3.14(a).

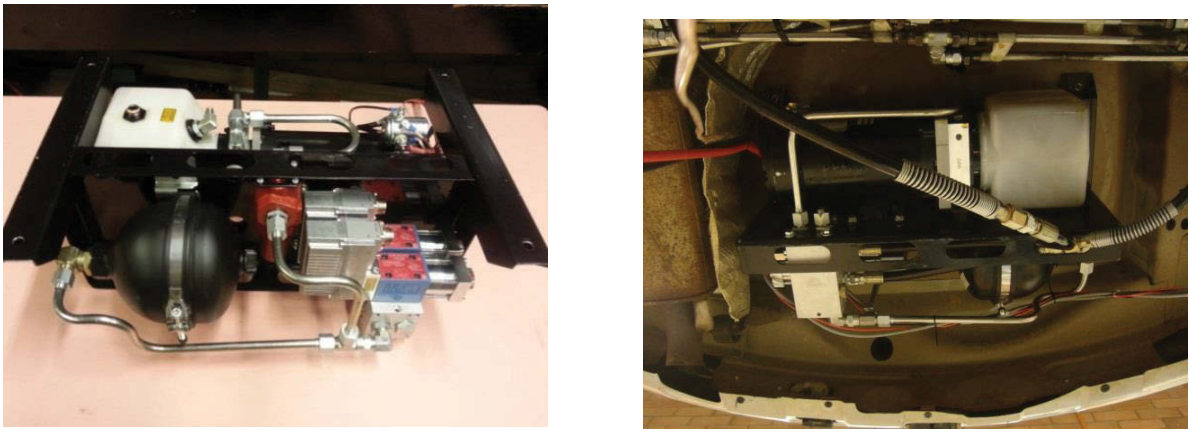

(a) Assembled *(b) Mounted*

Figure 4.8 Assembled and mounted pressure control unit of the active HIS

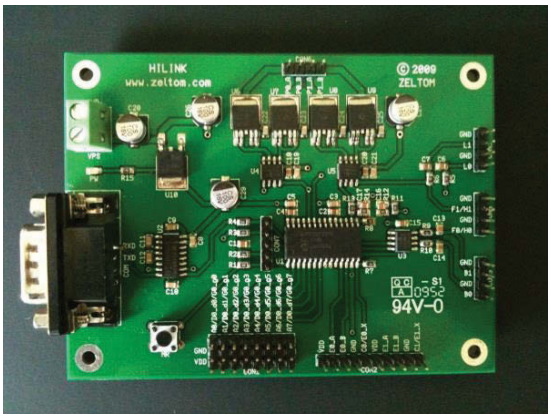

Figure 4.9 Simulink-based real-time implement board

The obtained experimental results are presented to compare the vehicle's roll angle and suspension deflection before and after control. Three sets of tests with different ground excitations are implemented. The 'Benchmark' and the 'Active' in the figures represent the

test results with and without active HIS system respectively. When the right side of the vehicle body is higher than the left side, the roll angle is defined as positive roll angle, and when it is lower, the roll angle is defined as negative roll angle.

4.5.2 Experimental results

4.5.2.1 Continuously sinusoidal road input

The obtained results from the first set of tests are presented in Figure 4.10. The ground excitation signal is described as two out-of-phase 0.01 m, 0.5 Hz sinusoidal waves to the left- and right-side wheels, shown in Figure 4.10(a). The restoring roll moment supplied by active HIS is shown in Figure 4.10(b). The vehicle body roll angle and roll rate before and after active control are measured and compared in Figure 4.10(c) and Figure 4.10(d) respectively. Benchmark data is collected using the same test procedure but with active suspension disabled. The result shows the roll angle has been significantly reduced by the active HIS with 37.5%.

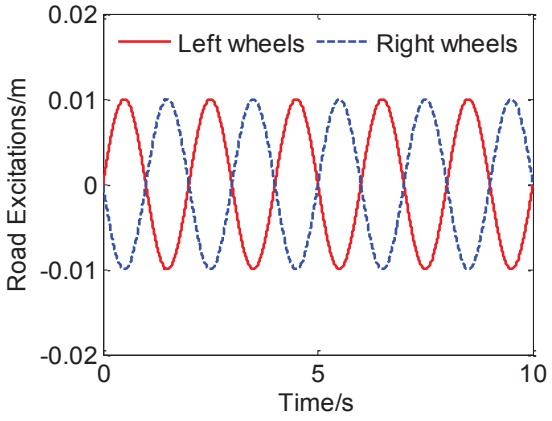

(a) Ground excitation

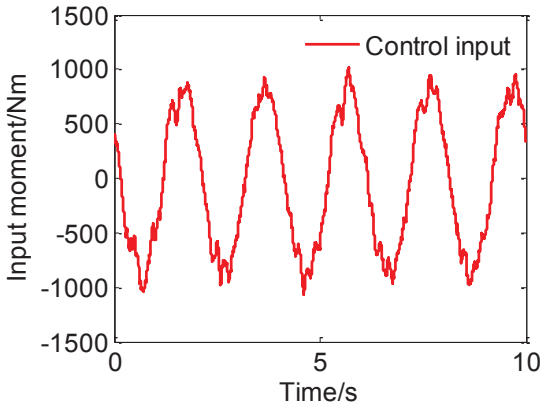

(b) The restoring roll moment supplied by active HIS

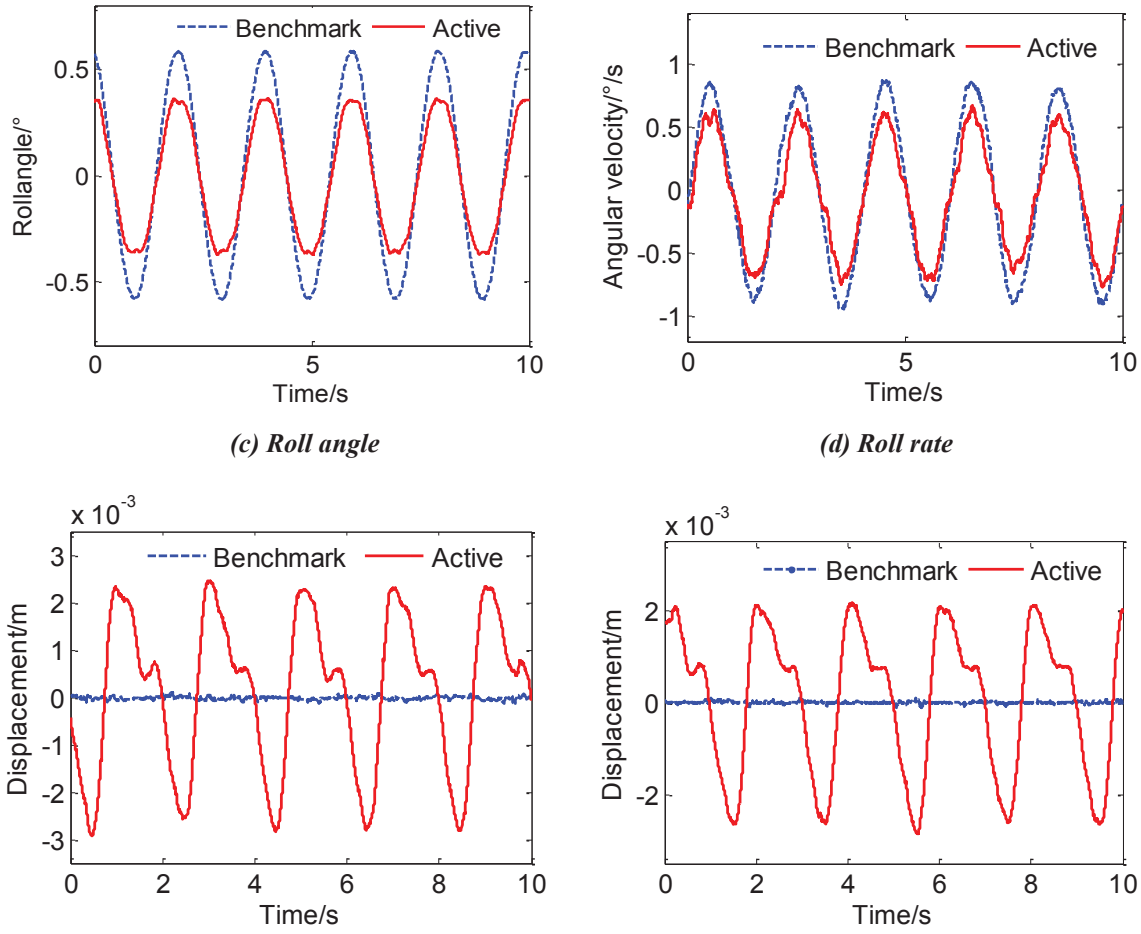

(c) Roll angle

(d) Roll rate

(e) Left suspension deflection

(f) Right suspension deflection

Figure 4.10 Experimental result of the continuously sinusoidal input

Figure 4.10(e) and Figure 4.10(f) compare the suspension deflections at rear-left and rear-right wheel stations. It can be seen that before control suspension deflections almost maintain zero, which means the ground excitation is directly transferred to the vehicle body. However, after control, the suspension deflections fluctuate largely along with the road excitation.

4.5.2.2 Half sinusoidal road input

Figure 4.11 depicts the results of the second set of tests. The ground excitation to the experimental car is a couple of oppositional half sinusoidal waves, with the amplitude of 0.02 m and frequency of 0.5 Hz, which is shown in Figure 4.11(a). The anti-roll moment input by the active HIS is presented in Figure 4.11(b).

The comparison of vehicle body roll angle from the tests with/without active HIS control is presented in Figure 4.11(c). The obtained results show that there is 44.5% reduction in the peak roll angle from the active HIS test. However, it takes slightly longer for the system to come back to still. The corresponding roll rate is described in Figure 4.11(d).

The suspension deflections at rear-left and rear-right wheel stations are compared in Figure 4.11(e) and Figure 4.11(f). In the benchmark test, the active HIS is turned off, and there is very limited suspension deflection. When the active HIS is turned on, it is noticed that the left suspension is considerably extended by the hydraulic actuator to compensate for the vehicle body's motion, reducing body roll angle.

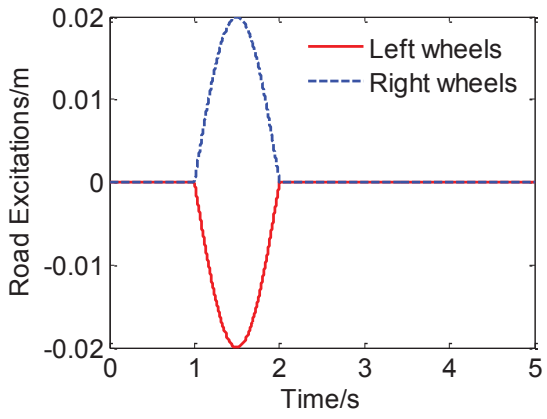

(a) Ground excitation

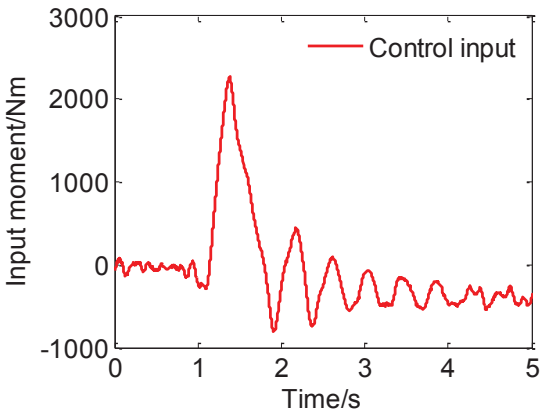

(b) The restoring roll moment supplied by active HIS

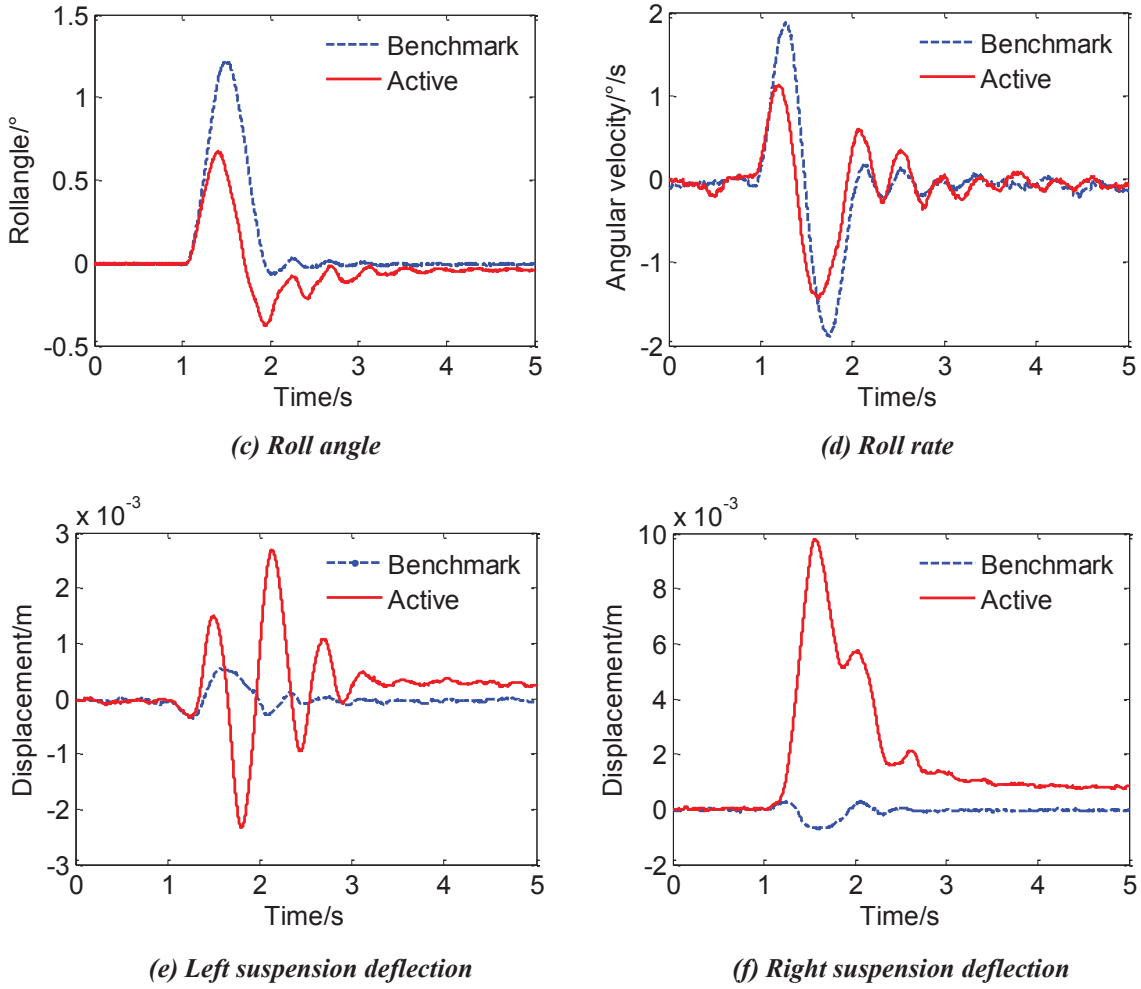

(c) Roll angle

(d) Roll rate

(e) Left suspension deflection

(f) Right suspension deflection

Figure 4.11 Experimental result of the half sinusoidal road input

4.5.2.3 Single sinusoidal input

In the third set of tests, the ground excitations to left and right wheels are two out-of-phase sine waves (one cycle only), at 0.5Hz with the amplitude of 0.02m, as shown in Figure 4.12(a). The results are described in Figure 4.12(b - f). The anti-roll moment generated by the hydraulic actuators is illustrated in Figure 4.12 (b). The roll angle and roll rate response before and after using active HIS are compared in Figure 4.12(c) and Figure 4.12(d), respectively.

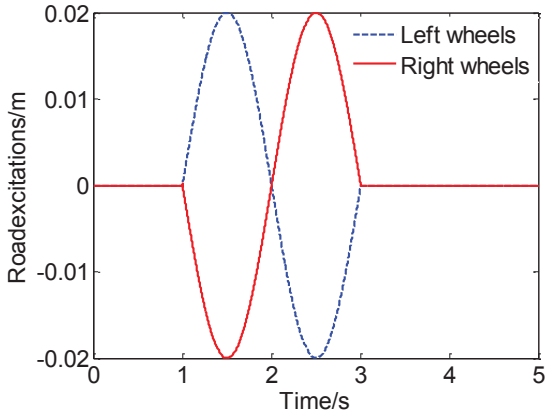

(a) Ground excitation

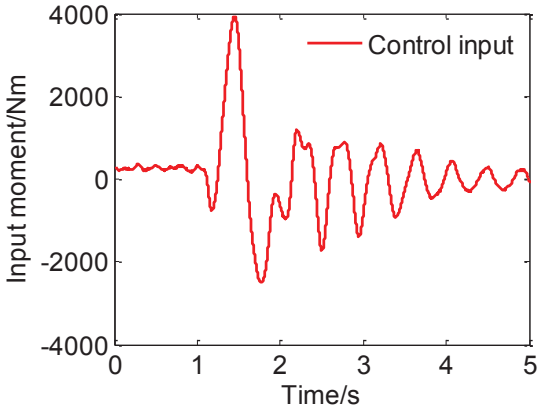

(b) The restoring roll moment supplied by active HIS

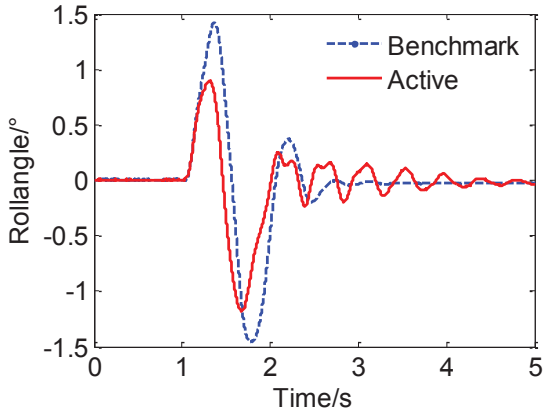

(c) Roll angle

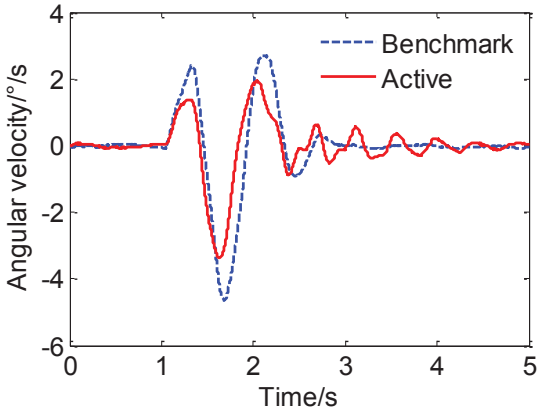

(d) Roll rate

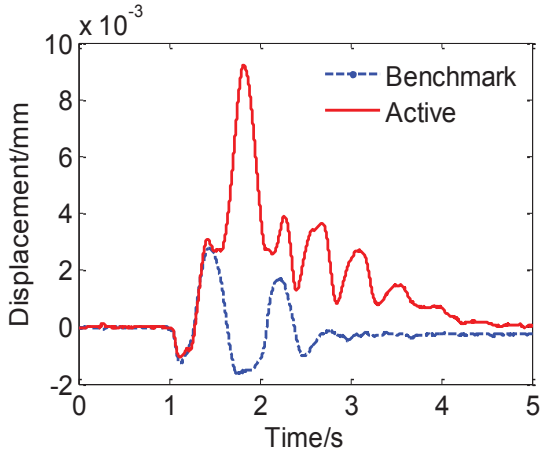

(e) Left suspension deflection

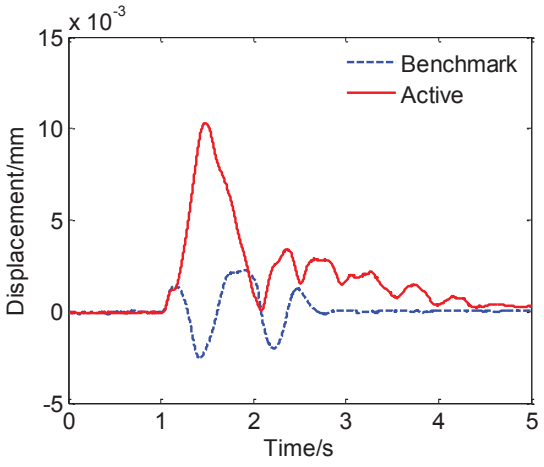

(f) Right suspension deflection

Figure 4.12 Experimental result of the single sinusoidal road input

From Figure 4.12(c) it can be seen that the roll angle decreases by 37.2% on the positive peak and 18.9% on the negative peak. The rear-left and rear-right suspension deflections are shown in Figure 4.12(e) and Figure 4.12(f), respectively. It is clear that both left and right suspensions in the active case have larger motions than the benchmark, thanks to the active suspension system, which compensates the vehicle body's motion by varying suspension travel.

4.6 Discussions

The measured results of the suspension deflection demonstrate that under low-frequency ground excitations (e.g. 0.5Hz), the vehicle's wheels and body tend to roll together as a rigid body, and conventional suspensions do little in regards to vehicle body position control. In contrast, to maintain the vehicle body's neutral level, active HIS can change suspension deflection by using hydraulic actuators to minimise vehicle body roll according to its roll angle control strategy.

From the obtained control results, it can be seen that some response curves are not as smooth as those before control, e.g., roll rate in Figure 10(d). This phenomenon may suggest that, by applying active HIS, the vehicle's ride comfort is slightly compromised. It is mainly because of three reasons. The first one is the noise contained in the sensor measurement and generated from the signal process. The accumulated noise certainly has a negative effect on the vehicle responses. The second reason is the nonlinear friction factor. Specifically, it is because of the difference between the static friction coefficient and the dynamic friction coefficient on the contact face of the piston and the cylinder. The last reason is the high-order dynamics of the actual hydraulic system.

Conventional active suspensions consume a considerable amount of energy. ZF Lemförder developed a novel active suspension system named ASCA (Active suspension via control arm). The maximum power consumption of the ASCA is claimed to be only 1.2 kW per wheel because of "the combination of a parallel spring/actuator configuration", and this makes to a total of 4.8kW for four wheels [120]. It is reported that the active suspension developed by Bose can exert energy with the shocks working like generators and ends up consuming two horsepower (1.5kW) of energy [121]. By contrast, the proposed active HIS system, only has a motor rated 1kW. The reason is that in the design, a 2L accumulator is employed and pre-charged with a high pressure (commonly 90bar~100bar) to satisfy the flow requirement, and thus the motor can be made smaller. In addition, the active HIS system only responds when it is demanded which reduces the energy consumption further.

4.7 Summary

In this chapter, the modelling of active HIS system is presented. The pressure control unit has been isolated from the rest of the system and tested in the frequency domain to eliminate the interference from other sub-systems. The experimental result has been provided in the Bode graph, from which a second-order transfer function model has been estimated for the hydraulic pressure control unit. Then the transfer function of the modelling has been converted into the state-space form to be compatible with the existing mechanical model. After the assembly of the mechanical and hydraulic sub-systems, a basic H∞ controller has been designed based on the integrated vehicle-HIS model. The weighting functions for the H∞ controller have been provided, and the implementation of the controller to the test vehicle fitted with active HIS system has been presented.

The controller's performance has been validated in three sets of tests under different road excitations. The preliminary experimental results on the active HIS show the applicability of the novel active HIS mechanism and its controller. The tests verify the designed controller in continuous excitation test and impulsive test in the first two experiments, with considerable roll angle reduction of 37.5% and 44.5%, respectively, compared to the benchmark result. In the third test with a full cycle of sinusoidal road inputs, the controller also gave consistent, effective and stable control performance.

5 Design and Implementation of Fuzzy, Fuzzy-PID and LQR Controllers for Active HIS

5.1 Introduction and rationale

The active HIS was validated experimentally in Chapter 4. In this chapter, three representatively classical, optimal and intelligent control methods, namely the fuzzy, PID and LQR control methods, are used with the vehicle roll control with the active HIS. However, when the basic PID controllers are applied to the active HIS in the experimental implementation, they can hardly provide stable control performance. Therefore, a self-tuning fuzzy-PID controller is developed.

This chapter begins with the fuzzy, LQR and fuzzy-PID controllers design. The fuzzy rules of the fuzzy controller and the weighting matrices of the LQR controller are provided. In the proposed fuzzy-PID controller, the fuzzy control method is applied to adjust the proportional, integral and derivative parameters in real time to make the controller more adaptive to the system.

Then the designed LQR, Fuzzy and Fuzzy-PID controller are validated by simulations in MATLAB and experiments on the 4-post test rig under different ground excitations. As in the H∞ controller tests in Chapter 4, the control objective is to minimise the roll angle of the vehicle's body to reduce the possibility of rollover. The results are discussed to compare the performances of the obtained controllers.

5.2 Controller design

The PID control is a widely used classical control algorithm. When developing a PID controller, the mathematic model of the system to be controlled is not necessary. Generally, the parameters of PID controllers are tuned manually by users based on their experiences. Similar to H∞ controllers, LQR controllers can generate optimal control signals efficiently. However, the optimal LQR control is different from the PID control in that it significantly depends on the system model. The more accurate the system model is, the better performance the LQR controller can produce. Fuzzy logic control is capable of handling nonlinear systems [122]. In the fuzzy control, control inputs are converted from linguistic descriptions to desirable outputs by using fuzzy logic. As in the PID control, developing fuzzy controllers does not need system models. The dynamic ranges of the input and output of the controller are determined by the users' knowledge.

5.2.1 Fuzzy controller design

Active HIS is a complicated system that contains nonlinearities, which made it difficult to model the system accurately for the model-based control algorithms. However, the fuzzy control can handle the nonlinearity effects of the system without a system model but through estimating the dynamic operating ranges of the system. In this section, the development of a fuzzy controller is presented.

The first step is to define the inputs and outputs of the controller and then map the inputs and outputs by membership functions. As the control target is to stabilise the vehicle roll motion under road excitations, the roll angular displacement of the vehicle body θ is adopted as the primary input. In addition, to ensure the control performance, the angular

acceleration of the sprung mass $\ddot{\theta}$ is also added as a secondary input. The active control forces are the control output of this controller, but due to the control forces at the left and right side of the active HIS are the same in terms of the magnitude with opposite signs, they can be represented by f .

There are in total three categories of membership functions that are used in the design of this controller. The triangle membership function (trimf), Pi membership function (pimf) and Gauss membership function (gaussmf) represent the inputs of roll angle, roll acceleration and the outputs of active control forces respectively. They are shown as follows

$$\begin{aligned} \mu_{A_i}(x_i) &= trimf(x_i, a_i, b_i, c_i) \\ \mu_{B_j}(x_j) &= pimf(x_j, a_j, b_j, c_j, d_j) \\ \mu_{C_k}(x_k) &= gaussmf(x_k, c_k, \sigma) \end{aligned} \tag{5.1}$$

The second step is to apply fuzzy logic to design the fuzzy controller. In general, the development of a basic fuzzy controller includes three main stages. They are the fuzzification, inference engine and defuzzification.

In the fuzzification stage, the crisp input values are converted to fuzzy values under an association of membership functions [123]. The arrangement of the input membership functions and the estimated dynamic input ranges are shown in Figure 5.1. It can be seen from Figure 5.1(a) that the roll angle range is estimated from -6 degree to 6 degree, where nine membership functions are applied, namely the negative very large (NVL), negative large (NL), negative medium (NM), negative small (NS), zero (ZS), positive small (PS), positive medium (PM), positive large (PL) and positive very large (PVL).

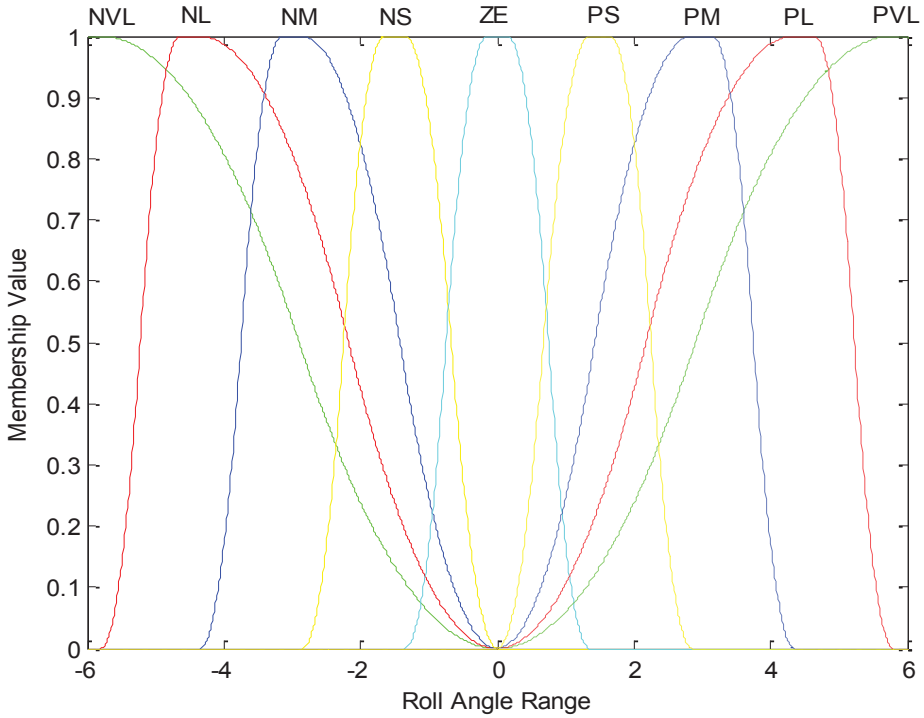

(a) Roll angle

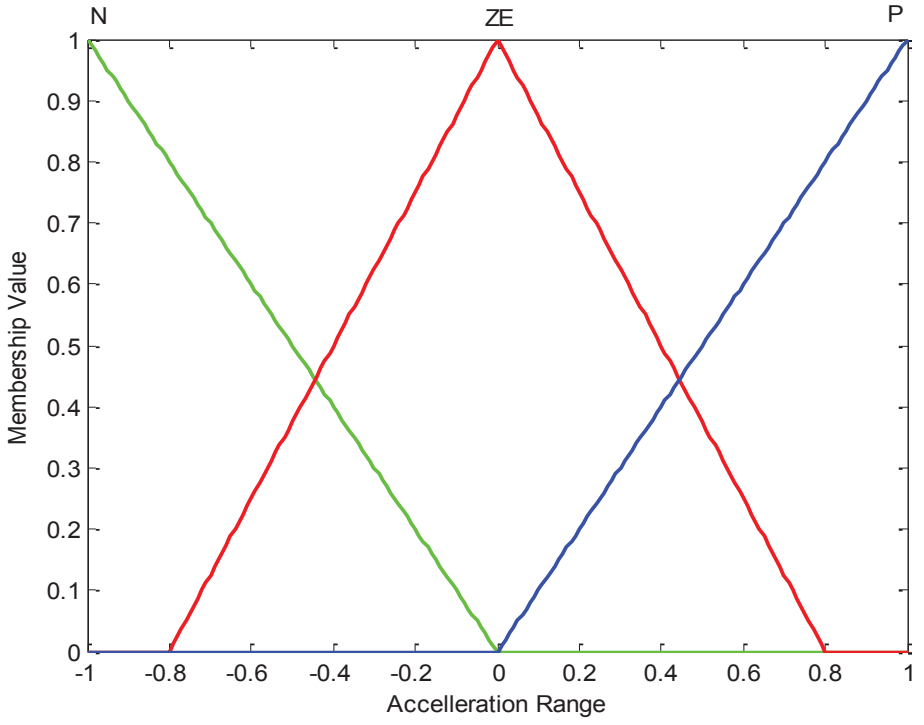

(b) Roll angular acceleration

Figure 5.1 Membership functions of the inputs

From Figure 5.1(b) the roll acceleration range is estimated from -1 degree per second squared to 1 degree per second squared. Three membership functions, negative (N), zero (Z) and positive (P) are used.

In the stage of the inference engine, the obtained fuzzy values of the inputs are converted to the fuzzy values of the output according to the defined rule based system or database. In this session, the Mamdani method is adopted to build the rule base, which can be expressed as

Rule i: IF $x_i = A_i$ AND $x_j = B_j$ THEN $x_k = C_k$.

Table 5.1 shows the rule base of this controller. There are 27 rules in total.

Table 5.1 Rule base of the fuzzy controller

θ	$\ddot{\theta}$	f	θ	$\ddot{\theta}$	f	θ	$\ddot{\theta}$	f
NVL	N	NVL	NVL	ZE	NVL	NVL	P	NL
NL	N	NNL	NL	ZE	NL	NL	P	NM
NM	N	NL	NM	ZE	NM	NM	P	NS
NS	N	NM	NS	ZE	NS	NS	P	NS
ZE	N	ZE	ZE	ZE	ZE	ZE	P	ZE
PS	N	PM	PS	ZE	PS	PS	P	PS
PM	N	PL	PM	ZE	PM	PM	P	PS
PL	N	PVL	PL	ZE	PL	PL	P	PM
PVL	N	PVL	PVL	ZE	PVL	PVL	P	PL

For example:

Rule 3: IF (θ) = NM AND ($\ddot{\theta}$) = N THEN (f) = NL

Rule 27: IF (θ) = PVL AND ($\ddot{\theta}$) = P THEN (f) = PL

In the stage of the defuzzification, the fuzzy output values are converted to the crisp values to control the roll motion of the active HIS equipped vehicle. The setting of output membership functions and the 3-D output surface are shown in Figure 5.2.

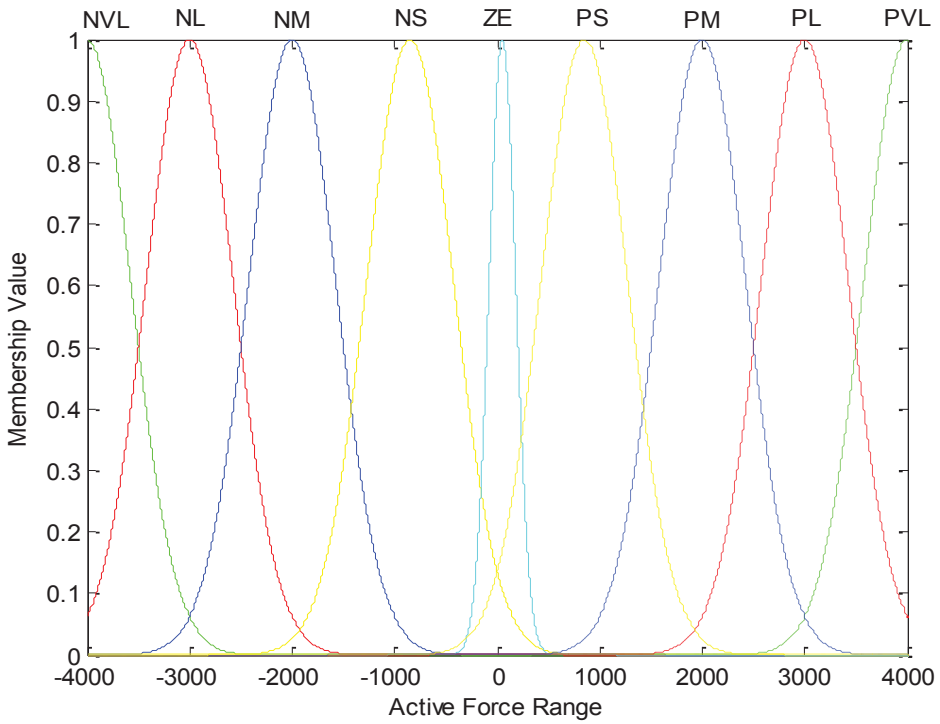

(a) Membership function

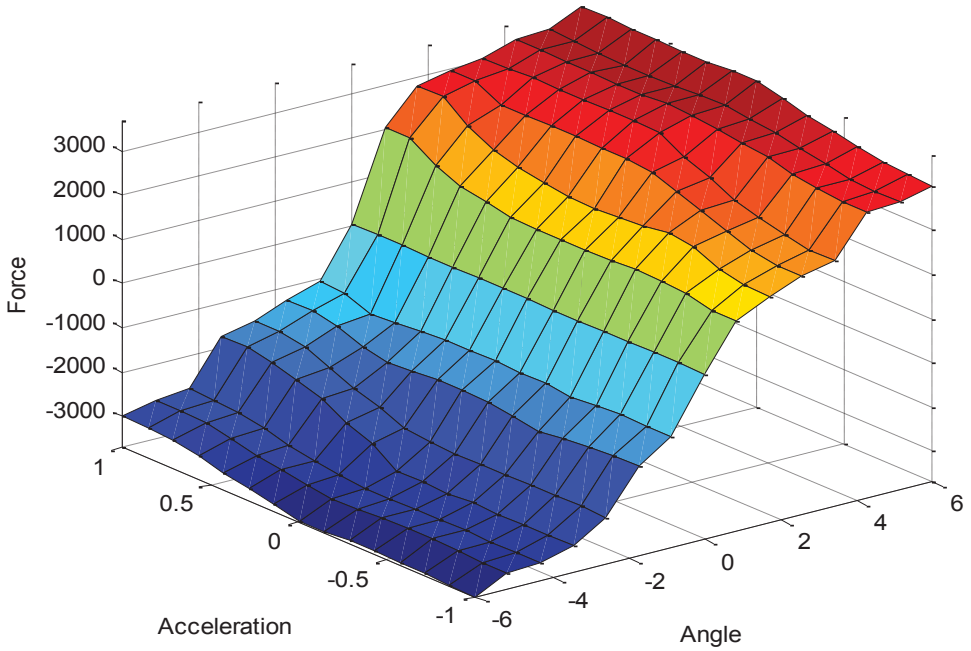

(b) 3-D output surface

Figure 5.2 Membership functions of the outputs and their 3D output surface

The output range of the active control force is estimated as from -4000 N to 4000 N and there are nine membership functions which are used, the same as the roll angle. In this controller, the defuzzification is carried out through the centroid of gravity method. The output of the controller can be yielded by the equation

$$f(x) = \frac{\int x_k \mu_k(x_k) dx}{\int \mu_k(x_k) dx}. \tag{5.2}$$

5.2.2 LQR controller design

Considering the active HIS equipped vehicle system, developing an LQR controller is to find an optimal matrix gain that enables the stabilising of the vehicle roll motion under road excitations. Figure 5.3 shows the controller with the plant. As shown in Figure 5.3, ground excitations are the external disturbances; the active control forces are the control inputs; the roll angle is the measured output and also the controlled output. The control strategy of this LQR controller is to stabilise the vehicle roll motion through minimising the roll angle by minimal control forces.

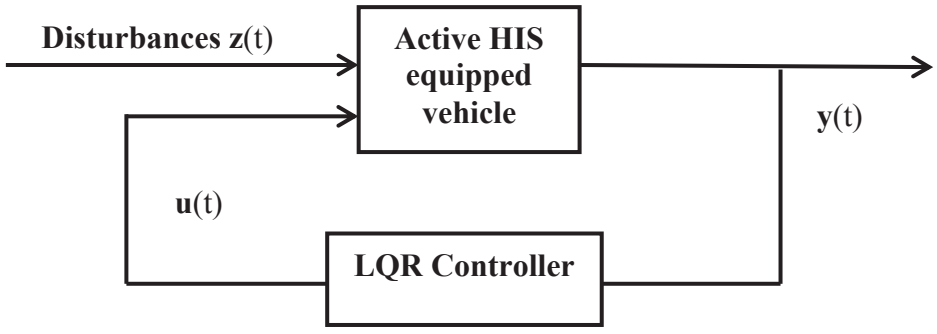

Figure 5.3 Schematic diagram of the LQR controller with the plant

In the LQR controller design, the controller synthesis is done in MATLAB. In general, the development of an LQR controller has the following steps.

Firstly, to derive the system equations and convert these equations to the state space from

$$\begin{cases} \dot{\mathbf{x}}(t) = \mathbf{A}\mathbf{x}(t) + \mathbf{B}\mathbf{u}(t) \\ \mathbf{y}(t) = \mathbf{C}\mathbf{x}(t) + \mathbf{D} \end{cases}; \tag{5.3}$$

Secondly, to identify the observability and controllability of the system and define the cost function of the system

$$\mathbf{J} = \int_0^\infty (\mathbf{x}^T \mathbf{Q}\mathbf{x} + \mathbf{u}^T \mathbf{R}\mathbf{u})dt\,; \tag{5.4}$$

Thirdly, to identify the matrix **Q** and **R** and then find the solution **P** in the algebraic Riccati equation

$$\mathbf{A}^T\mathbf{P} + \mathbf{P}\mathbf{A} - \mathbf{P}\mathbf{B}\mathbf{R}^{-1}\mathbf{B}^T\mathbf{P} + \mathbf{Q} = \mathbf{0}\,; \tag{5.5}$$

Fourthly, according to the obtained value of **P**, to calculate the optimal gain matrix **K** by using the formula

$$\mathbf{K} = \mathbf{R}^{-1}\mathbf{B}^T\mathbf{P}\,; \tag{5.6}$$

Finally, to tune the controller by adjusting the coefficient matrixes **Q** and **R** until a satisfactory control performance is achieved. In this section, the system model obtained in Chapter 4 is used to derive the LQR controller.

In the process of tuning the coefficient matrices **Q** and **R**, it is noticeable that adjusting the element of matrix **Q** leads to the changes in the response of the system, and adjusting the element of matrix **R** leads to the changes in the overshoot of the responses. The obtained gain matrix **K**, and coefficient matrices **Q**, **R** are presented

$$\mathbf{K} = [-1.8382 \quad 0 \quad 0.9073 \quad -0.9073 \quad -0.2918 \quad 0 \quad -0.0029 \quad 0.0029 \quad 0 \quad 0] \times 10^4$$

$$\mathbf{Q} = \begin{bmatrix} 6.10^6 & & & & & & & & & \\ & 0.1 & & & & & & & 0 & \\ & & 0.1 & & & & & & & \\ & & & 0.1 & & & & & & \\ & & & & 0.1 & & & & & \\ & & & & & 0.1 & & & & \\ & & & & & & 0.1 & & & \\ & & & & & & & 0.1 & & \\ & 0 & & & & & & & 0.1 & \\ & & & & & & & & & 0.1 \end{bmatrix}. \quad (5.7)$$

$$\mathbf{R} = [0.005]$$

5.2.3 Fuzzy-PID controller design

As mentioned earlier, it is hard to achieve a stable control performance by the primary form of PID controller, so a self-tuning fuzzy-PID controller is designed in this section. The 'self-tuning' means it is able to tune its parameters automatically according to the change of system properties or presence of disturbances.

Figure 5.4 provides a visual aid for the fuzzy-PID controller with the controlled plant. In Figure 5.4, the conventional PID controller is taken as a foundation of the controller and the PID parameters are regulated by a pre-set fuzzy logic block. The fuzzy logic control is integrated into the PID controller for better tuning the PID parameters and therefore better

controlling the system. Specifically, the change and rate of change of the measured output in errors are employed as the inputs of the fuzzy logic control. The crisp values of the outputs from the fuzzy controller are the current parameters of the PID controller, and they change continuously when the controller system is running. Therefore, the fuzzy-PID can provide better and more stable performance than conventional PID controllers.

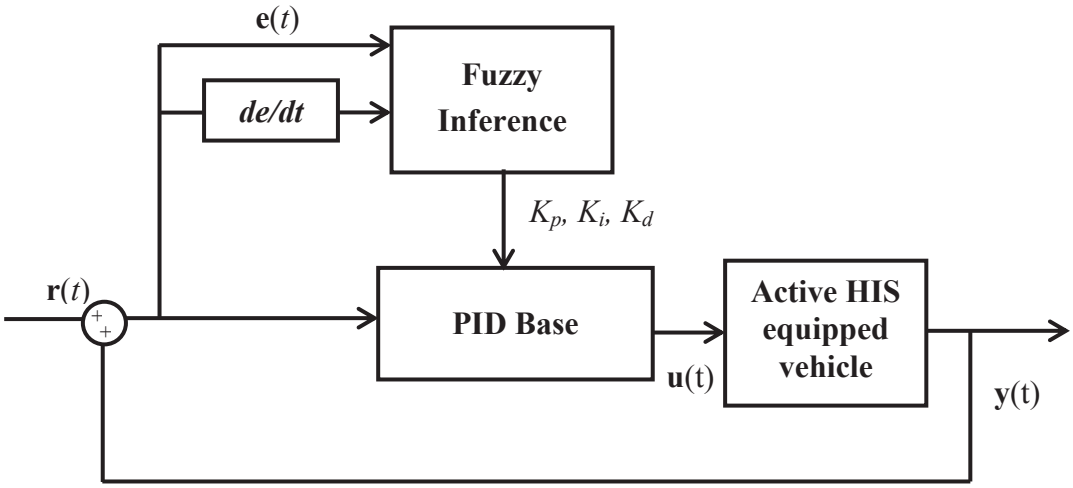

Figure 5.4 Schematic diagram of the Fuzzy-PID controller with the plant

In the development of the PID controller base, the Ziegler-Nichols rule is used to determine the controller parameters. The fuzzy logic part design for the fuzzy-PID controller is similar to the previously designed fuzzy controller. With considering *e(t)* and *de/dt* as the fuzzy inputs and K_p, K_i, K_d as the fuzzy outputs, the fuzzy logic is applied to develop the fuzzy control part of the fuzzy-PID controller.

The interval changes of the PID parameters are estimated as

K_p : [700 - 900] K_i : [5 - 15] K_d : [55 - 65].

The interval changes of the output error and the rate of the error are estimated as

e(t) : [-6 – 6] *de/dt* : [-5 – 5].

After obtaining the fuzzy-PID controller, the fuzzy part of the controller needs to be tuned to optimise the response of the system. The final obtained rule base between the fuzzy inputs and fuzzy outputs of the fuzzy-PID controller are shown in Table 5.2.

Table 5.2 Fuzzy-PID controller rule base

Ki		**de/dt**		
		N	ZE	P
e	N	**L**	**MD**	**S**
	ZE	**L**	**MD**	**S**
	P	**MD**	**MD**	**MD**

Kd		**de/dt**		
		N	ZE	P
e	N	**S**	**S**	**MD**
	ZE	**S**	**MD**	**L**
	P	**MD**	**L**	**L**

Kp		**de/dt**		
		N	ZE	P
e	N	**L**	**L**	**MD**
	ZE	**L**	**MD**	**S**
	P	**MD**	**S**	**S**

There are nine rules for each output because there are three membership functions that are applied to the fuzzy inputs of both the error and error rate. They are corresponding to the linguistic variables of N (negative), ZE (zeros), and P (positive) as shown in the table. For the fuzzy outputs of K_p, K_i, K_d, there are also three membership functions that are applied, corresponding to S (small), MD (medium) and L (large), respectively. For example,

Rule 5 of K_i: IF e = ZE AND de/dt = ZE THEN K_i = MD;

Rule 2 of K_d: IF e = N AND de/dt = ZE THEN K_i = S;

Rule 9 of K_p: IF e = P AND de/dt = P THEN K_p = S.

With the obtained rule base, the results of the outputs K_p, K_i, K_d are represented in the 3-D output surfaces, as shown in Figure 5.5. In this section, the centroid of gravity method is also used for the defuzzification.

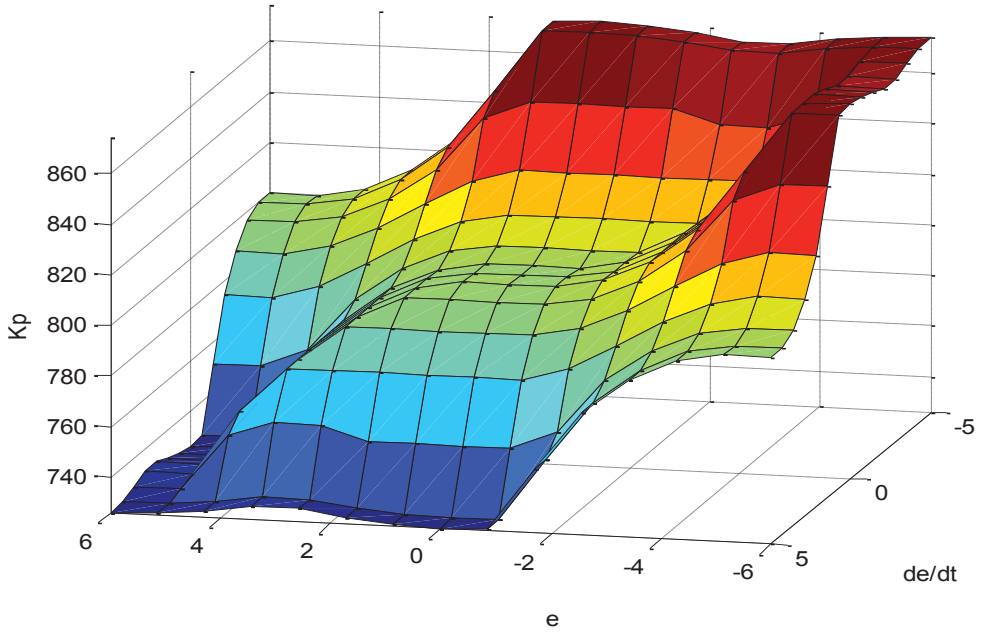
Kp
860
840
820
800
780
760
740
6
4
2
0
-2
-4
-6
e
5
0
-5
de/dt

(a) K_p

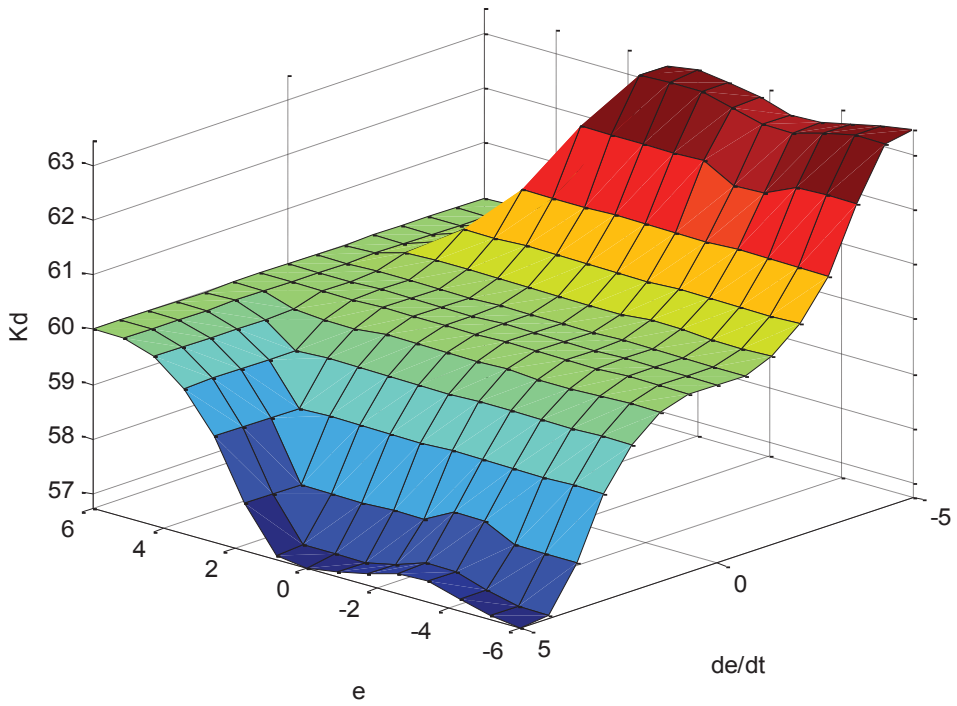
Kd
63
62
61
60
59
58
57
6
4
2
0
-2
-4
-6
e
5
0
-5
de/dt

(b) K_i

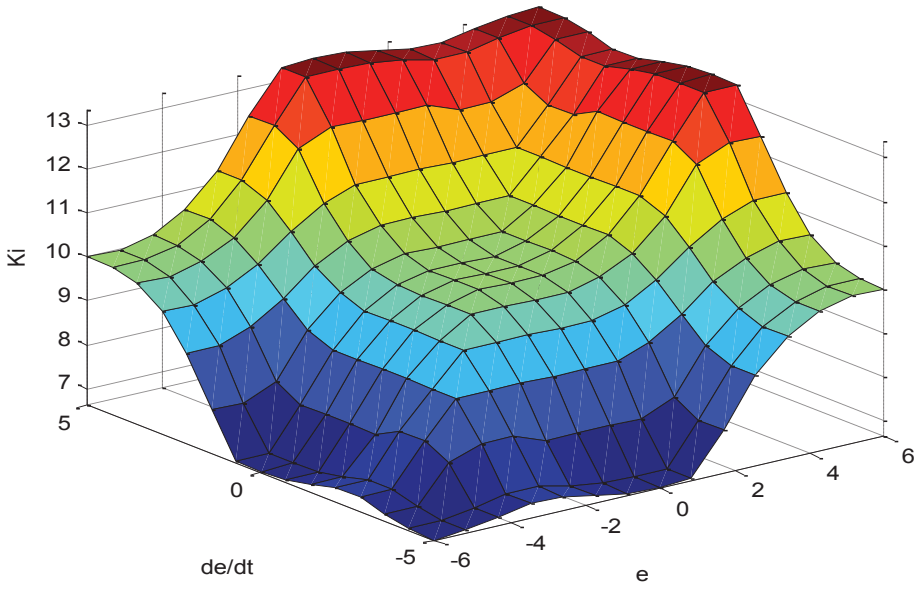

(c) K_d

Figure 5.5 3-D output surface of the PID parameters

5.5 Simulations

The feasibilities of the obtained LQR, fuzzy and fuzzy-PID controllers are verified through simulations in MATLAB. Having these three controllers implemented on the system model introduced in Chapter 4, the vehicle responses regarding the roll angle and suspension deflection are compared. The responses of the vehicle without active HIS are used as benchmarks for the comparisons and labelled 'Passive' in the presented figures. Three groups of out-of-phase road excitations with the fishhook, slalom and half-sine shapes of road surfaces are used in the simulations.

The summary of the simulation results of the roll angle reduction and suspension deflection are presented in Table 5.3. As shown in the table, the roll angle reductions compared with

the roll angle response of the passive system are used to compare the roll resistance performance. The suspension deflections on the left and right sides, namely the relative displacements between the sprung mass and the unsprung masses, are similar, so only one of them is presented to evaluate the control stability. It can be seen from Table 5.3 that the fuzzy-PID controller performs the best with larger roll angle reductions than the PID controller and more stable control performance than the fuzzy controller.

Table 5.3 The summary and comparison of the simulation results

Signal	***Roll angle Reduction***			***Suspension Deflection***		
	LQR	Fuzzy	F-PID	LQR	Fuzzy	F-PID
Fishhook	50%	70%	60%	Unstable	Unstable	Stable
Slalom	40%	80%	70%	Unstable	Unstable	Stable
Half sine	50%	70%	70%	Stable	Stable	Stable

5.5.1 Fishhook road input

The simulation results under fishhook ground inputs are shown in Figure 5.6, where Figure 5.6 (a)-(c) present the road input signals, the roll angle and suspension deflection responses, respectively. As illustrated in Figure 5.6 (b), the fuzzy-PID has the best performance with a reduction of 60% in the roll angle. Figure 5.6 (c) shows that under the active controls, the suspension deflections are much larger than those in the passive system. It is because the controllers generate control forces to tilt the vehicle body against the roll motion. Even if the LQR and fuzzy controller also decrease the roll angle significantly, some oscillations can be observed from the results, which lead to the instability of the system and affect the ride performance of the vehicle. In Figure 5.6 (c), the suspension deflection response of the LQR Controller is the smallest, which indicated that the LQR controller consumes the least energy than other controllers.

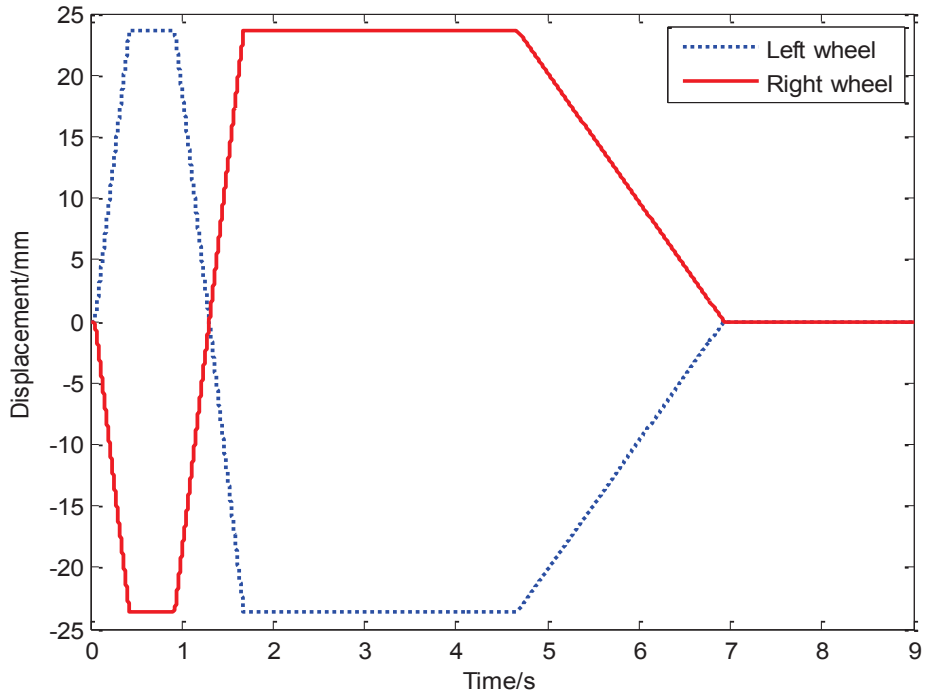

(a) Road input signals

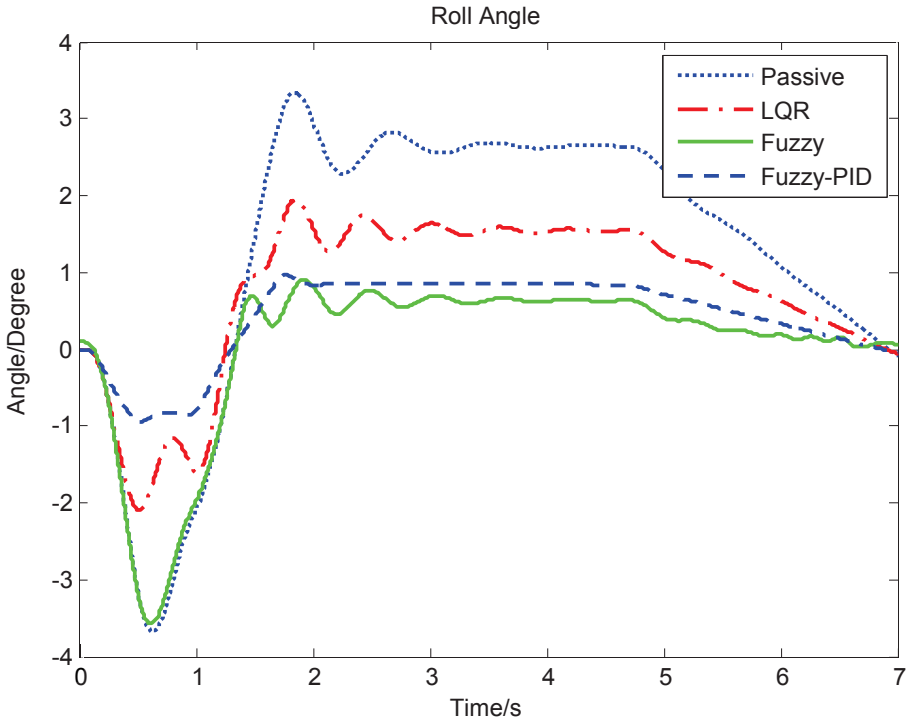

(b) Roll angle

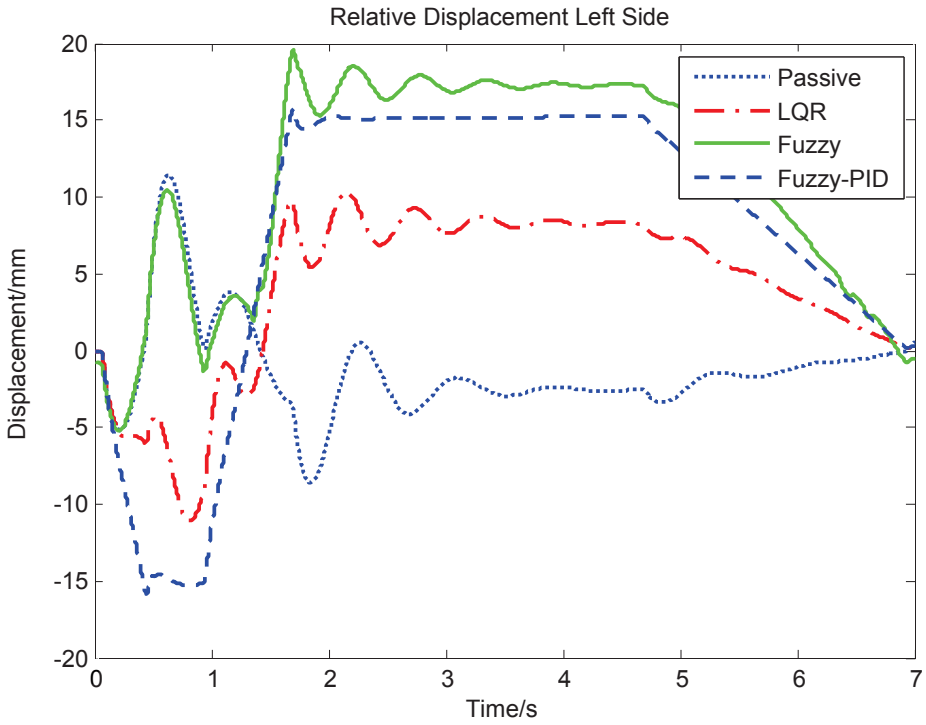

(c) Suspension deflection on the left

Figure 5.6 Simulation responses under fishhook ground excitations

5.5.2 Slalom road input

Figure 5.7 presents the slalom road input signals and the corresponding simulation results. The roll angle responses are compared in Figure 5.7 (b), from where it can be seen that the roll angle is significantly decreased by the fuzzy, fuzzy PID and LQR controllers with 80%, 70% and 40% reductions respectively. The fuzzy controller produces the largest roll angle reduction, but similar to the previous simulation, the results show some oscillations, while the fuzzy-PID controller achieves the control target of reducing the roll angle with stable performance. In Figure 5.7 (c), the LQR Controller also produces the smallest suspension deflection, which confirms the advantage of the LQR controller in the energy consumption.

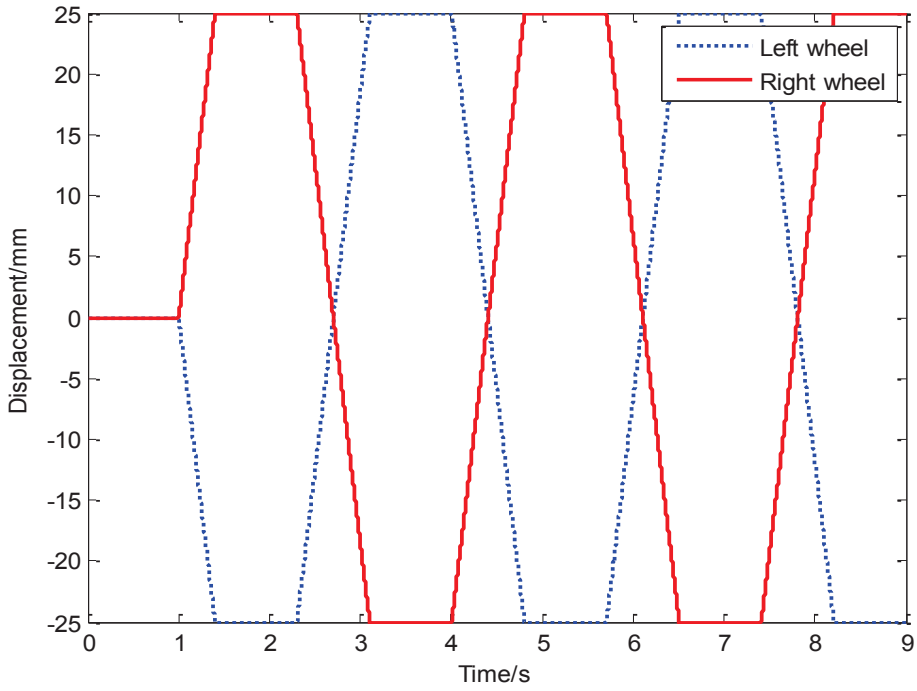

(a) Road input signals

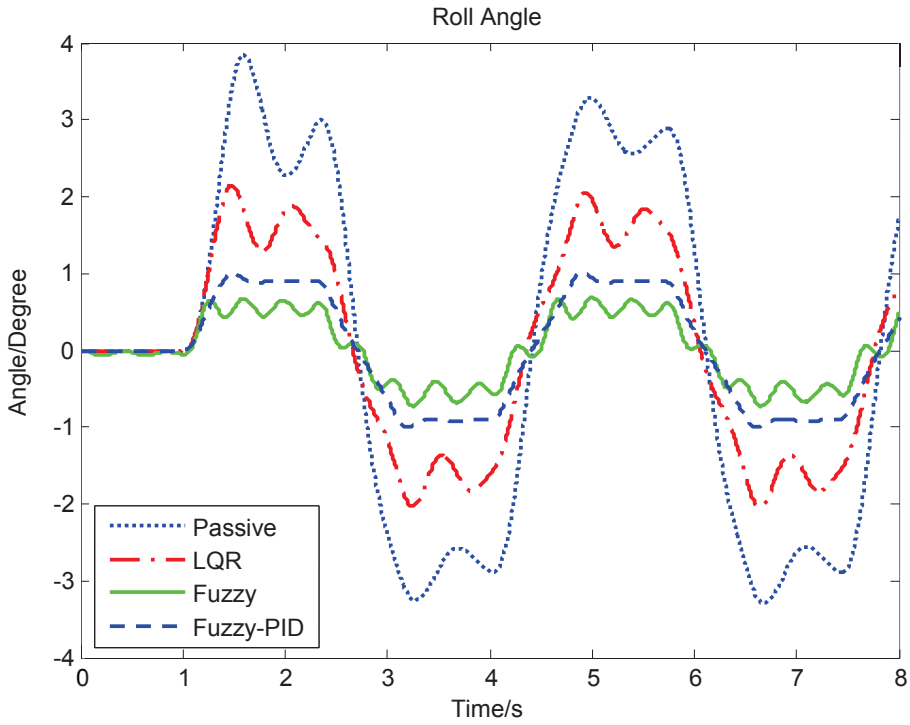

(b) Roll angle

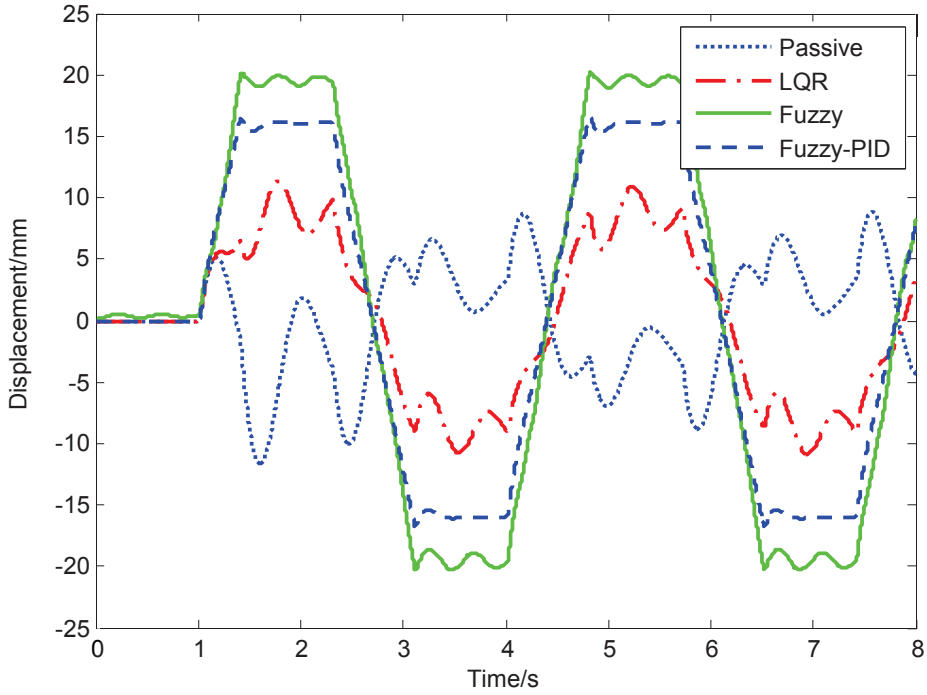

(c) Suspension deflection on the left

Figure 5.7 Simulation responses under slalom ground excitations

5.5.3 Half sine road input

For the simulation under 1/3 Hz half sine road excitations, the system responses with the proposed controllers are compared in Figure 5.8. It is can be seen from Figure 5.8 (b) that the LQR's controller decreases approximately 50% of the roll angle while the fuzzy and fuzzy-PID controller show more significant improvement with more than 70% roll angle reductions. However, considering the oscillations brought about by the fuzzy controller, the fuzzy-PID controller shows better control performance. In Figure 5.8 (c), large suspension deflections caused by the fuzzy and fuzzy-PID controllers can be observed, while the LQR controller produces a smaller suspension deflection that indicates its advantage in energy consumption, but it is also the reason for the compromised performance.

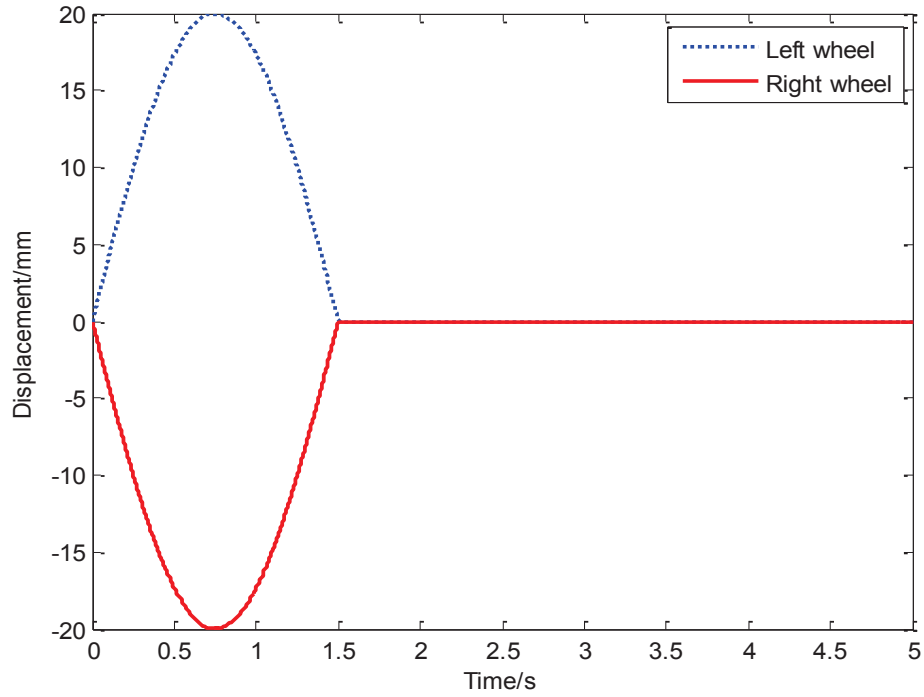

(a) Road input signals

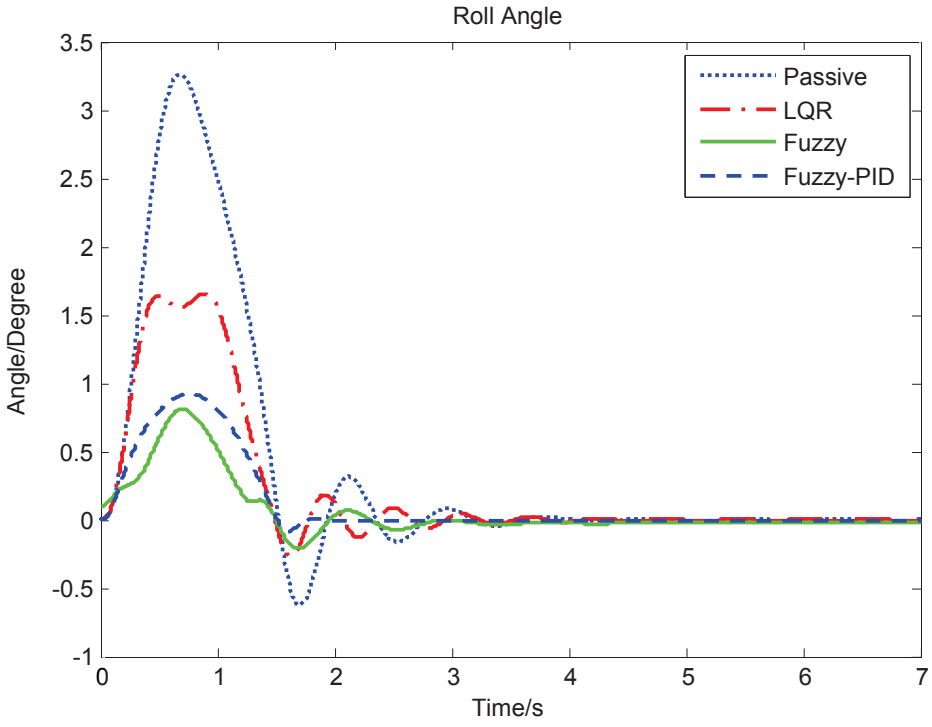

(b) Roll angle

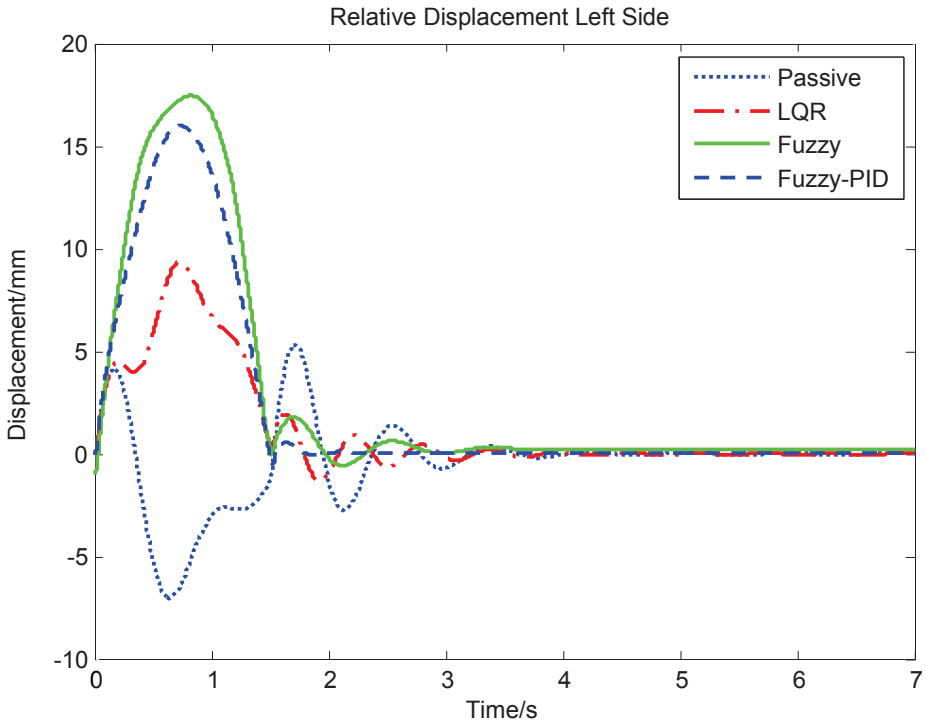

(c) Suspension deflection on the left

Figure 5.8 Simulation responses under half sine ground excitations

5.6 Experiments

The fuzzy and fuzzy-PID controllers are also tested on the real system. Three experiments are conducted on the 4-post test rig with three sets of ground roll excitations namely the half-sine, single-sine and sinusoidal road input. The vehicle responses without active control are also used as benchmarks. The vehicle responses under the fuzzy control and fuzzy-PID control are compared with the vehicle without control. The reductions in the roll angle and the suspension deflections are compared to show the control performance and the stability of the fuzzy and fuzzy-PID controllers.

5.6.1 Half sine road input

The experimental results under the half sine road excitations are shown in Figure 5.9, where Figure 5.9 (a) presents the half sine road inputs with 20 mm amplitude and 1/3 Hz frequency. The blue dotted curve represents the road excitation acting on the left wheels while the red curve represents the out-of-phase road input acting on the right wheels. The roll angles are compared in Figure 5.9 (b), from where we can see that the fuzzy controller reduces the roll angle by about 30%, but noticeable overshoot can be observed from the results. The fuzzy-PID controller shows better control performance than the fuzzy controller not only in terms of the roll resistant performance (with a 35% roll angle reduction) but also with less overshoot in the response.

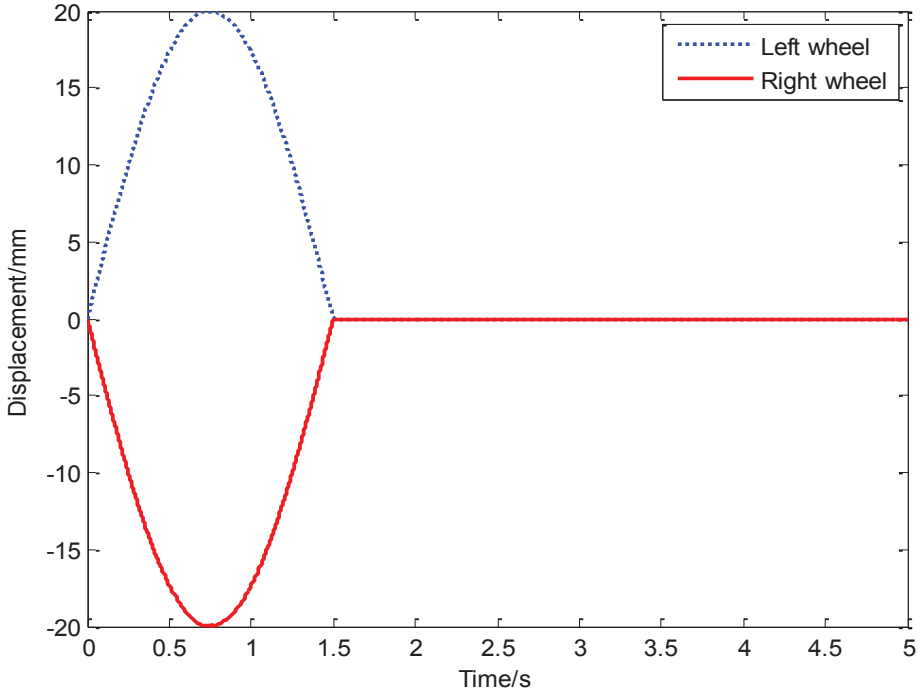

(a) Ground input signal

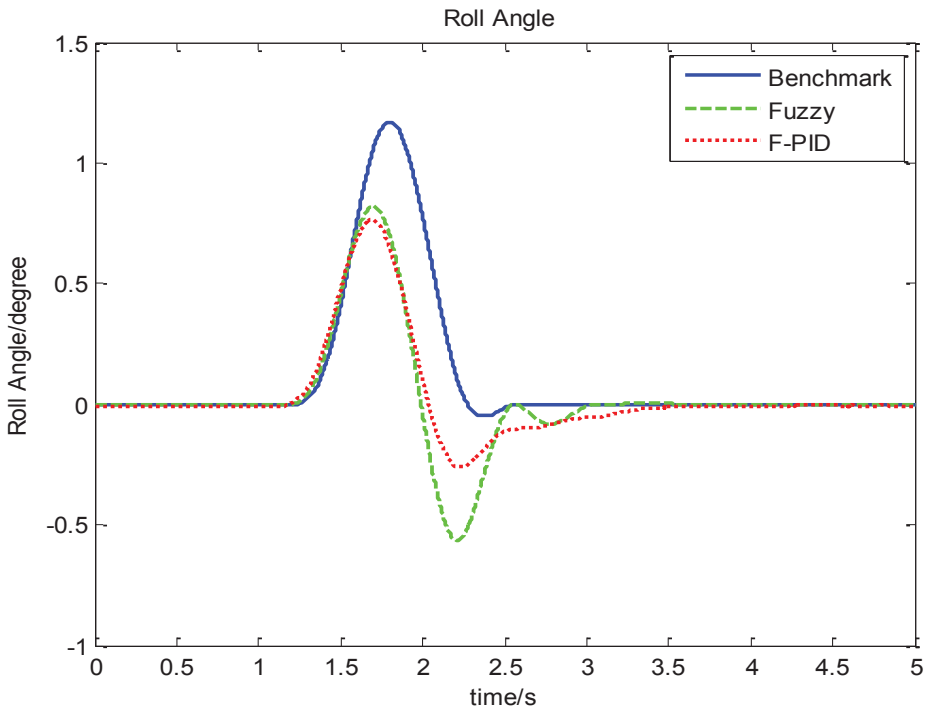

(b) Roll angle

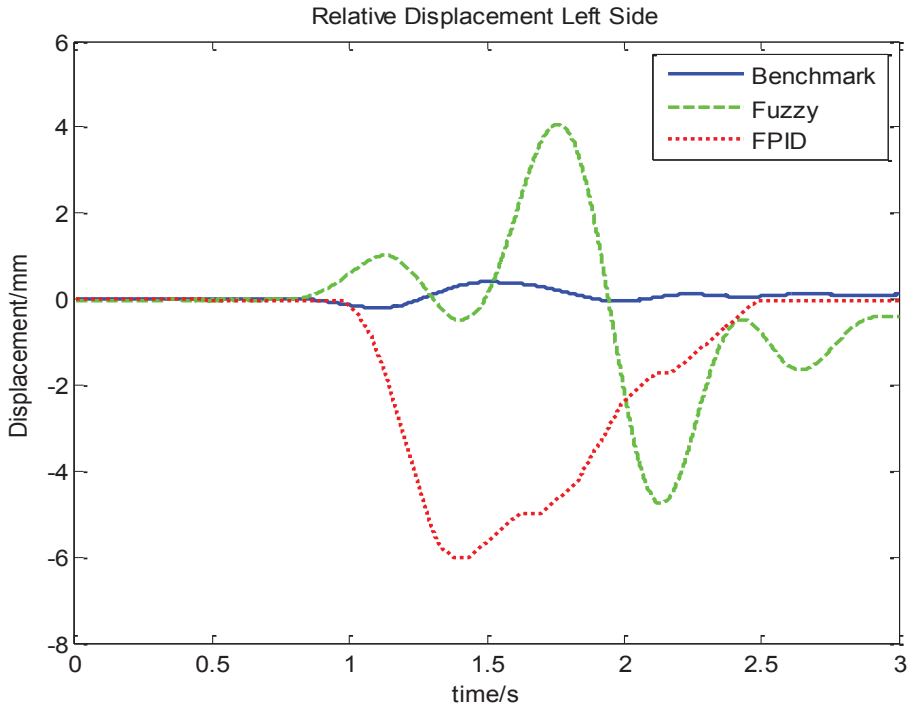

(c) Suspension deflection on the left

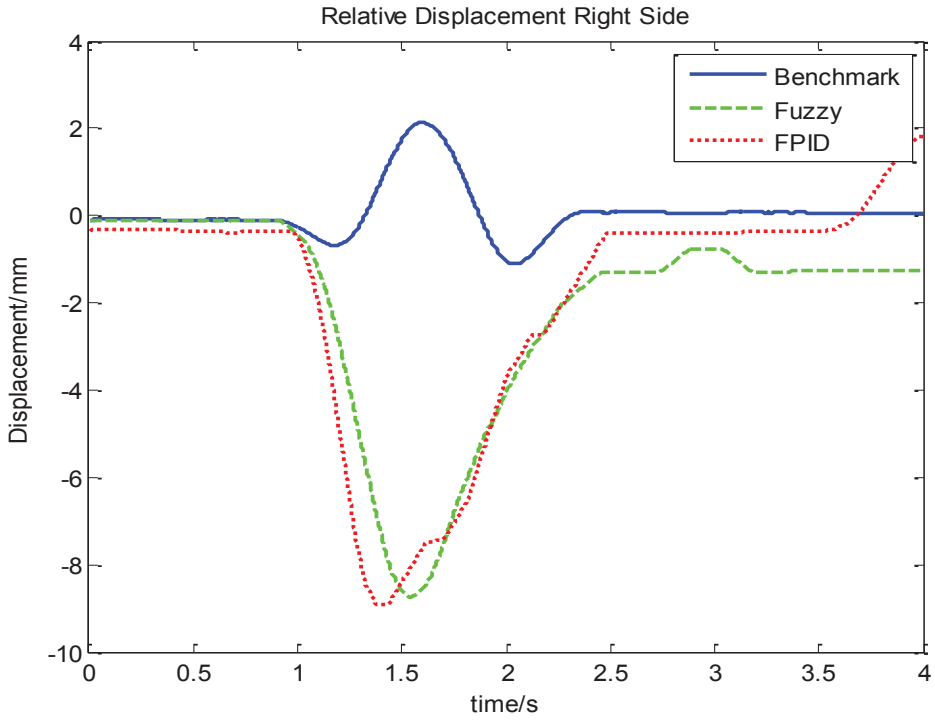

(d) Suspension deflection on the right

Figure 5.9 Experimental results under half sine road inputs

Figure 5.9 (c) and Figure 5.9 (d) provide the comparisons of the suspension deflection responses on the left and right respectively. It also can be seen that the suspension deflections on the left and right sides of the fuzzy-PID controller are similar but out of phase, which matched well with the simulation results. The suspension deflection on the left side of the fuzzy controller shows apparent oscillations that lead to the overshoot in the roll angle. It is also noticed that the controlled systems produce large suspension deflections while the suspension deflection of the passive system is quite small. As discussed in the simulation results, it is because of the high stiffness of the original passive suspension and the contributions of the active control forces.

5.6.2 Single sine road input

Figure 5.10 shows the experimental results under the single sine road excitations with 20 mm amplitude and 0.5 Hz frequency. The road inputs exerted on the left and right wheels are out of phase for generating the roll motion of the vehicle body as shown in Figure 5.10 (a). Figure 5.10 (b) plots the comparison of the roll angles of the passive and controlled systems. A 50% roll angle decrease indicates the good performances of the fuzzy controller. Compared with the fuzzy controller, the fuzzy-PID controller still performs better with an approximately 55% reduction in the roll angle.

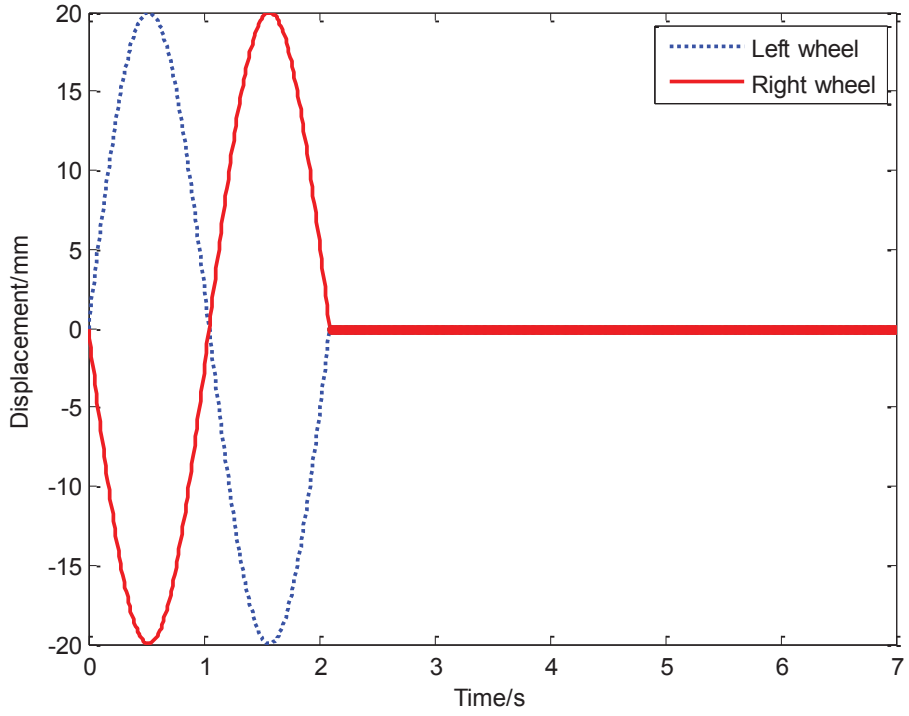

(a) Ground input signal

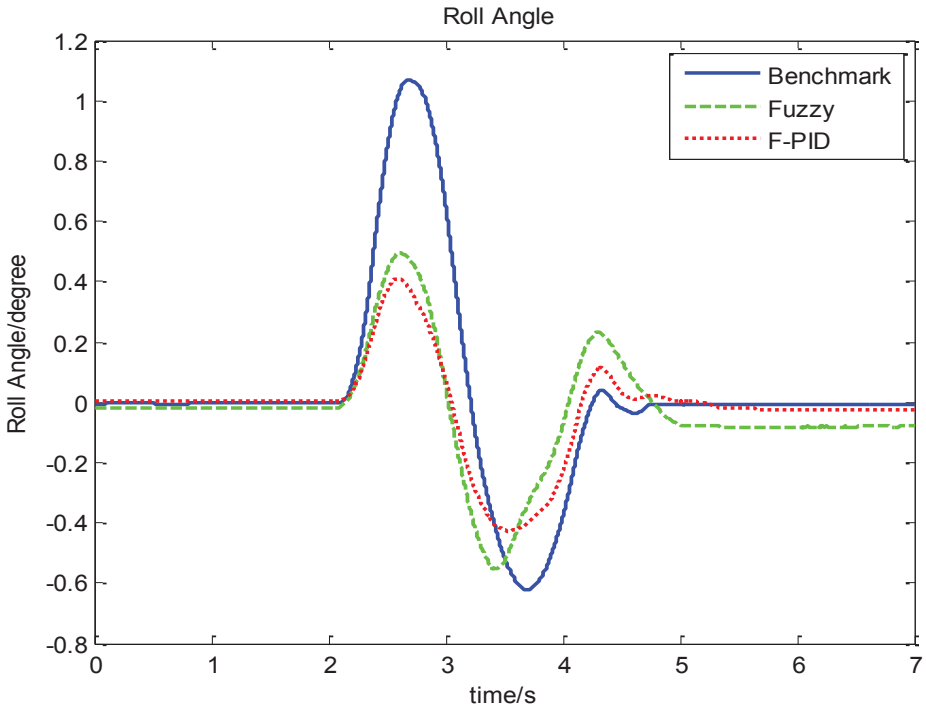

(b) Roll angle

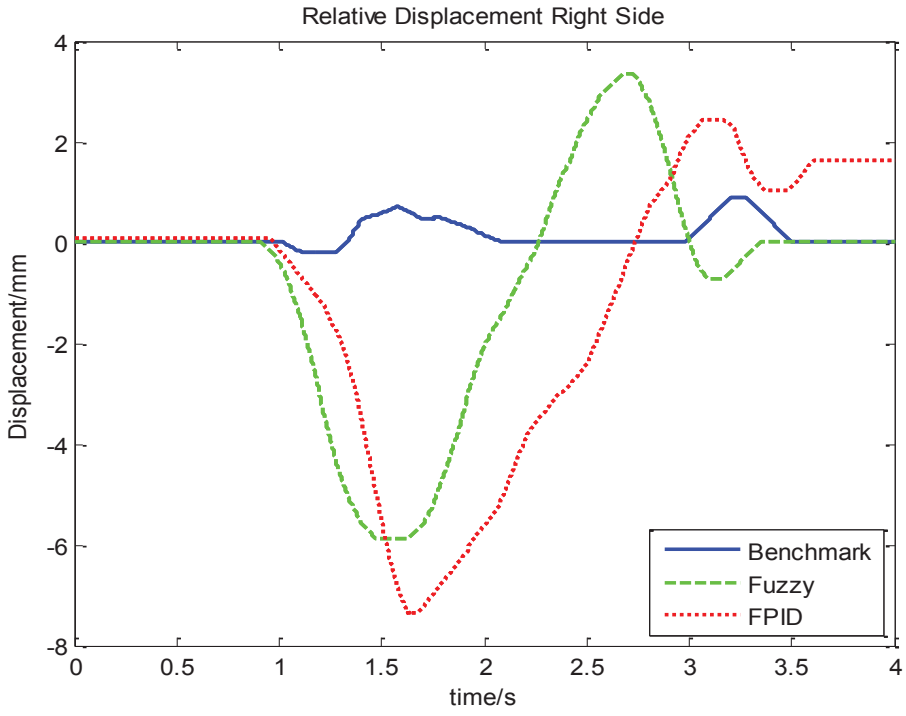

(c) Suspension deflection on the right

Figure 5.10 Experimental results under single sine road inputs

In Figure 5.10 (c), an error between the 3th and 4th seconds can be observed from the suspension deflection response of the passive system. These inaccurate results are caused by the sensor errors. Moreover, the difference between the passive case and the two controlled cases are similar to the previous test, which is brought about by the active control forces.

5.6.3 Sinusoidal road input

The experimental results under the sinusoidal ground input are given in Figure 5.11. Figure 5.11 (a) presents the out-of-phase road excitations with 5 mm amplitude and 0.5 Hz frequency for the left and right wheel. The results the roll angle responses are compared in Figure 5.11 (b), where the fuzzy controller leads to a 30% roll angle reduction compared to the benchmark and the fuzzy-PID control also performs slightly better with a smaller peak value in the roll angle.

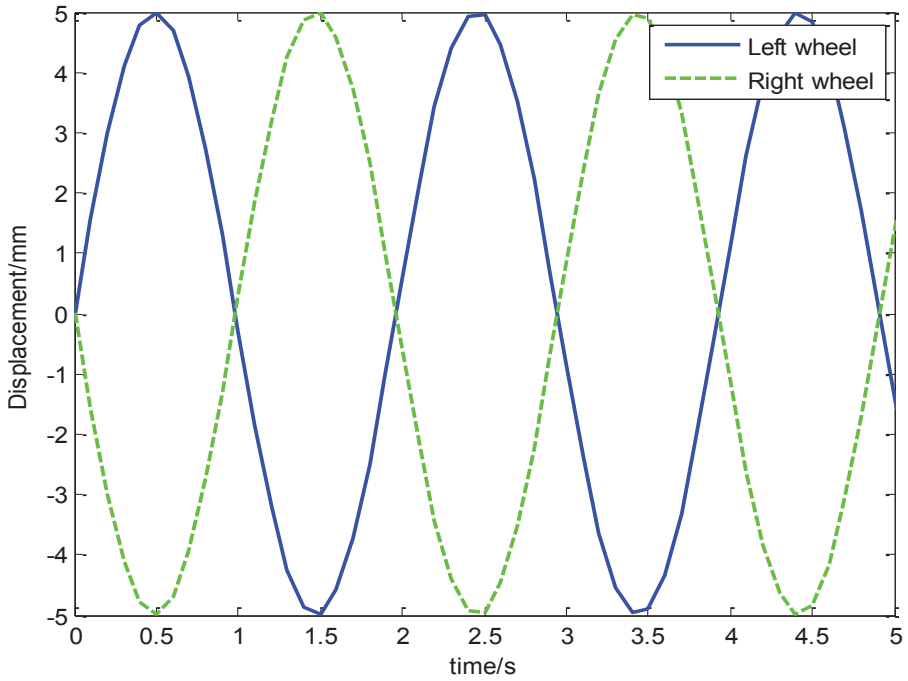

(a) Ground input signal

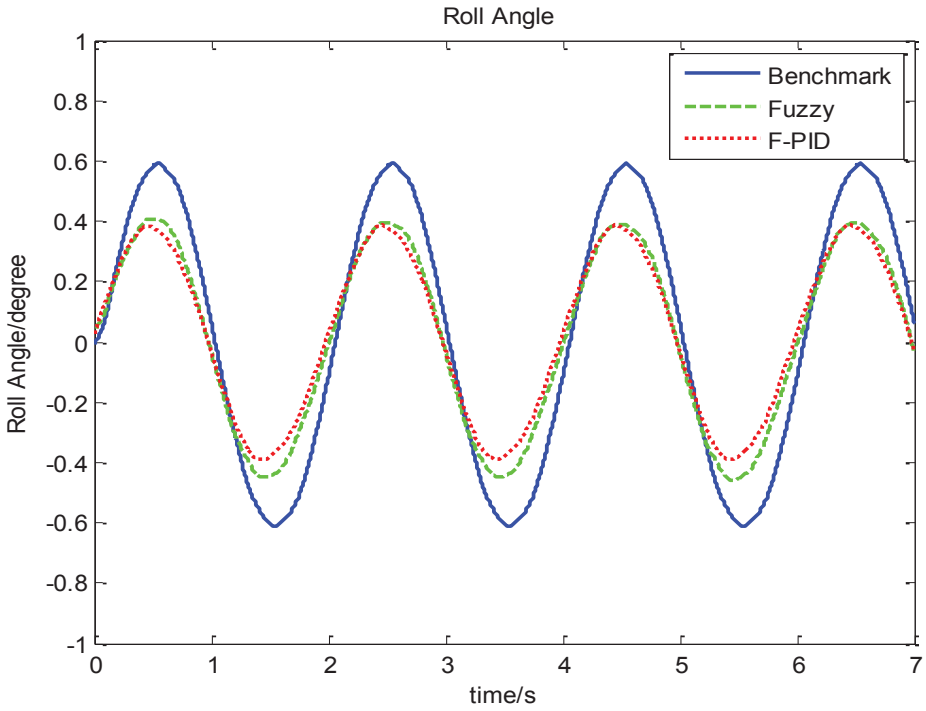

(b) Roll angle

Figure 5.11 Experimental results under sinusoidal road inputs

5.7 Summary

The primary target of this chapter was to apply different sorts of control algorithms on the active HIS to improve its control performance. The fuzzy, LQR and fuzzy-PID controllers were designed and validated by the simulations under a set of road excitations. The significant reductions in the roll angle presented in the results verified the controllability of the obtained controllers. The simulation results indicated that the fuzzy-PID controllers could provide the best control performance among these three controllers with larger roll reductions than the LQR controller and less oscillation than the fuzzy controller. The relatively small suspension deflections produced by the LQR controller indicated its

advantage of energy consumption, but it is also the reason for the compromised control performance.

The fuzzy and fuzzy-PID controllers were also verified on the real system. A group of tests under road excitations were conducted on the four-post test rig introduced in Chapter 4. The results showed the fuzzy controller was able to decrease the vehicle roll angle significantly, but the fuzzy-PID controller performed better with larger roll angle reductions and less overshoot.

6 A New Model for the Active HIS and its Control Implementations

6.1 Introduction and rationale

In the initial investigation of the active HIS, noticeable progress was made. However, due to the nonlinearities of the fluid system, further performance improvements were unreachable. By looking at the root of the problem, it was found that because some physical variables (e.g. fluid flow, pipe friction) are not included in the mathematical model of the active HIS used in previous chapters, it is not sophisticated enough to describe the characteristics of the system. That is, the old model of the active HIS is so simple that it yields inaccurate estimations of the system's states. As the foundation of the model-based controllers, the system model needs to be rebuilt.

In this Chapter, an attempt is made to develop a new mathematical model of the active HIS system that includes the fluid flow and viscous friction. It is followed by the model parameter tuning, in which some data obtained from the tests for developing the old model are used to tune the new model. Then the model validation is carried out through simulations and tests. The tests are conducted on the aforementioned active HIS equipped SUV. The responses of the old mathematical model in the simulations are also compared with those of the new model to compare the accuracy of the two system models. Based on the new mathematical model, the model-based control theories are applied. An H∞ controller and an LQR controller are developed and implemented in simulations. The H∞

controller is also implemented on the test vehicle, and the test result is compared with its counterpart of the H∞ controller in Chapter 4.

6.2 Active HIS system model development

6.2.1 Active HIS modelling

The new system model is remaining a linear model so that the advanced linear control algorithms can be applied to the active HIS system. To simplify the development of the new model, the new model is developed at half car level and the half car model introduced in Section 4.3.2 is used. The dynamics of the accumulator and motor-pump setup are not considered. They are replaced by the pressures P_2 and P_4 as shown in Figure 6.1.

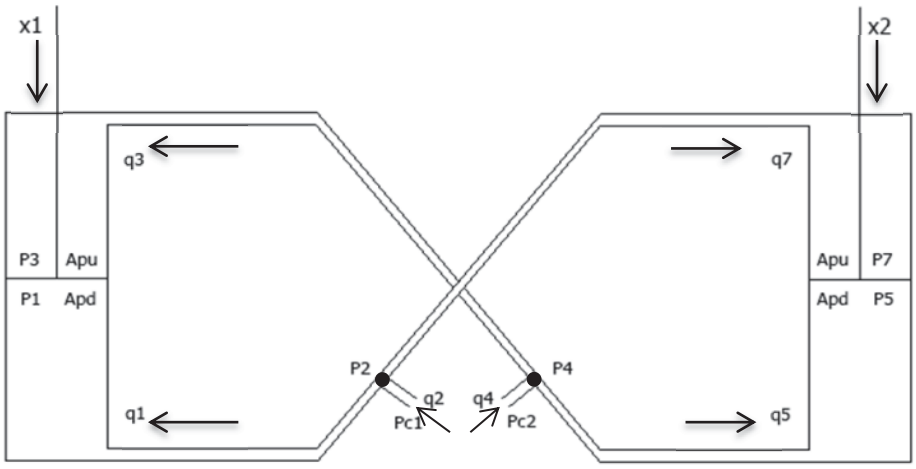

Figure 6.1 Transmission process of the control signals in the active HIS

In Figure 6.1, P_1, P_3, P_5, P_7, P_2, P_4 represent pressures at different positions of the system; q_1, q_3, q_5, q_7, q_2, q_4 are flows; P_{c1} and P_{c2} are the controlled pressures that are directly controlled by the active HIS; A_{pu} and A_{pd} are the upside and downside areas of the pistons respectively; x_1, x_2 are the displacements of the pistons; q_2 and q_4 are the flows from the

control unit. An assumption is made that they are solely controlled by the servo valve, and the effect of the accumulator is neglected.

P_2 and P_4 are the pressures at the outlets of the servo valve, which can be expressed by the equations

$$\dot{P}_2 = \frac{E}{LA_L}\left(q_2 - q_1 - q_7\right) = \frac{E}{LA_L}\left(GP_{c1} - GP_2 - q_1 - q_7\right) , \tag{6.1}$$

$$\dot{P}_4 = \frac{E}{LA_L}\left(q_4 - q_3 - q_5\right) = \frac{E}{LA_L}\left(GP_{c2} - GP_4 - q_3 - q_5\right) , \tag{6.2}$$

where E is the fluid bulk modulus; L and A_L are the length and area of the hydraulic pipeline from the servo valve to the hydraulic actuators respectively; G is proportional coefficient of the controller of the servo valve; P_{c1} is the reference pressure of the servo valve's first control signal; P_{c2} is the reference pressure of the servo valve's second control signal.

The equations of the fluid pressures inside the cylinder chambers are as follows

$$\dot{P}_1 = \frac{E}{sA_{Pd}}\left(A_{Pd}\dot{x}_1 + q_1\right) = \frac{E}{sA_{Pd}}\left(A_{Pd}\left(-l\dot{\theta} + \dot{Z}_s - \dot{Z}_{u1}\right) + q_1\right), \tag{6.3}$$

$$\dot{P}_3 = \frac{E}{sA_{Pu}}\left(-A_{Pu}\dot{x}_1 + q_3\right) = \frac{E}{sA_{Pu}}\left(A_{Pu}\left(l\dot{\theta} - \dot{Z}_s + \dot{Z}_{u1}\right) + q_3\right), \tag{6.4}$$

$$\dot{P}_5 = \frac{E}{sA_{Pd}}\left(A_{Pd}\dot{x}_2 + q_5\right) = \frac{E}{sA_{Pd}}\left(A_{Pd}\left(l\dot{\theta} + \dot{Z}_s - \dot{Z}_{u2}\right) + q_5\right), \tag{6.5}$$

$$\dot{P}_7 = \frac{E}{sA_{Pu}}\left(-A_{Pu}\dot{x}_2 + q_7\right) = \frac{E}{sA_{Pu}}\left(A_{Pu}\left(-l\dot{\theta} - \dot{Z}_s + \dot{Z}_{u2}\right) + q_7\right), \tag{6.6}$$

where s represents the initial fluid height in the chambers; $\dot{x}_1$ and $\dot{x}_2$ are the first order derivatives of the piston displacements; $\dot{Z}_S$ is the first order derivative of the sprung mass displacement and the $\dot{Z}_{u1}$ and $\dot{Z}_{u2}$ are the first order derivatives of the unsprung masses displacement in Figure 4.3. It is noted that $\dot{x} = -l\dot{\theta} + \dot{Z}_S - \dot{Z}_u$ is the relative displacement of the sprung and unsprung mass, showing the effects of the vehicle motion onto the fluid system.

Applying Newton's second law to the fluid system, we have

$$F - Cq_1 - \mathrm{Re}\dot{q}_1 = ma, \tag{6.7}$$

where C is the fluid damping parameter; Re is the pipe friction parameter; ρ is the density of the hydraulic oil.

Substituting F, a and m into Equation (6.7),

$$\left(P_2 - P_1\right)A_L - Cq_1 - \mathrm{Re}\dot{q}_1 = LA_L\rho\dot{q}_1, \tag{6.8}$$

$$\therefore \dot{q}_1\left(LA_L\rho + \mathrm{Re}\right) = -P_1A_L + P_2A_L - Cq_1. \tag{6.9}$$

Then the equation of the flow that goes into the bottom left fluid chamber can be obtained

$$\therefore \dot{q}_1 = -\frac{P_1}{\left(LA_L\rho + \mathrm{Re}\right)} + \frac{P_2}{\left(LA_L\rho + \mathrm{Re}\right)} - \frac{C}{\left(LA_L\rho + \mathrm{Re}\right)}q_1. \tag{6.10}$$

Similarly, the equations of the flows that go into other fluid chambers can be written as

$$\dot{q}_3 = -\frac{P_3}{\left(LA_L\rho + \mathrm{Re}\right)} + \frac{P_4}{\left(LA_L\rho + \mathrm{Re}\right)} - \frac{C}{\left(LA_L\rho + \mathrm{Re}\right)} q_3 , \tag{6.11}$$

$$\dot{q}_5 = -\frac{P_5}{\left(LA_L\rho + \mathrm{Re}\right)} + \frac{P_4}{\left(LA_L\rho + \mathrm{Re}\right)} - \frac{C}{\left(LA_L\rho + \mathrm{Re}\right)} q_5 , \tag{6.12}$$

$$\dot{q}_7 = -\frac{P_7}{\left(LA_L\rho + \mathrm{Re}\right)} + \frac{P_2}{\left(LA_L\rho + \mathrm{Re}\right)} - \frac{C}{\left(LA_L\rho + \mathrm{Re}\right)} q_7 . \tag{6.13}$$

6.2.2 Model integration

The coupling of the vehicle and the active HIS is achieved through the relationships of the active control forces by the hydraulic cylinders and the fluid pressures inside the hydraulic cylinders

$$F_1 = P_1 A_{Pd} - P_3 A_{Pu} , \tag{6.14}$$

$$F_2 = P_5 A_{Pd} - P_7 A_{Pu} . \tag{6.15}$$

where, F_1 and F_2 are the forces effected on the vehicle body by the left and right actuators respectively; P_1, P_3, P_5, P_7 are the pressures inside the two hydraulic circuits; A_{pu} and A_{pd} are the piston area of the upside and downside of the actuators.

Then the relationships between the vehicle dynamic variables and the pressures in the hydraulic actuators of the active HIS system can be derived by substituting F_1 and F_2 into the equations of motion of the half car model in Chapter 4.

The new mathematical model of the active HIS equipped vehicle can be derived by integrating the obtained equations of the state variables of the active HIS (i.e. equations of the pressures and flows) and the half car model. The state vectors of the active HIS and the half car models are as follows,

$$\mathbf{x}_{HIS} = \begin{bmatrix} P_1 & P_3 & P_5 & P_7 & q_1 & q_3 & q_5 & q_7 & P_2 & P_4 \end{bmatrix}^T \tag{6.16}$$

$$\mathbf{x}_{car} = \begin{bmatrix} \theta & Z_s & Z_{u1} & Z_{u2} & \dot{\theta} & \dot{Z}_s & \dot{Z}_{u1} & \dot{Z}_{u2} \end{bmatrix}^T \tag{6.17}$$

By combining the state vectors, the coefficient matrices of integrated system are obtained

$$\mathbf{x} = \begin{bmatrix} \mathbf{x}_{HIS} & \mathbf{x}_{car} \end{bmatrix}^T \qquad \mathbf{u} = \begin{bmatrix} \mathbf{u}_{HIS} & \mathbf{u}_{car} \end{bmatrix}^T \tag{6.18}$$

$$\mathbf{A} = \begin{bmatrix} \mathbf{A}_{HIS} & \mathbf{A}_{HIS-car} \\ \mathbf{A}_{car-HIS} & \mathbf{A}_{car} \end{bmatrix} \qquad \mathbf{B} = \begin{bmatrix} \mathbf{B}_{HIS} & \mathbf{0} \\ \mathbf{0} & \mathbf{B}_{car} \end{bmatrix} \tag{6.19}$$

Finally, the integrated system model can be obtained and expressed as

$$\dot{\mathbf{x}} = \mathbf{A}\mathbf{x} + \mathbf{B}\mathbf{u} \tag{6.20}$$

$$\begin{bmatrix} \dot{\mathbf{x}}_{HIS} \\ \dot{\mathbf{x}}_{car} \end{bmatrix} = \begin{bmatrix} \mathbf{A}_{HIS} & \mathbf{A}_{HIS-car} \\ \mathbf{A}_{car-HIS} & \mathbf{A}_{car} \end{bmatrix} \begin{bmatrix} \mathbf{x}_{HIS} \\ \mathbf{x}_{car} \end{bmatrix} + \begin{bmatrix} \mathbf{B}_{HIS} & \mathbf{0} \\ \mathbf{0} & \mathbf{B}_{car} \end{bmatrix} \begin{bmatrix} \mathbf{u}_{HIS} \\ \mathbf{u}_{car} \end{bmatrix} \tag{6.21}$$

where $\mathbf{A}_{HIS-car}$ represents the coupling matrix from the active HIS to the test vehicle and $\mathbf{A}_{car-HIS}$ represents the coupling matrix from the test vehicle to the active HIS. The reader is referred to Appendix A for more details of the system modelling.

6.3 Active HIS model parameter tuning

Some parameters of the active HIS equipped vehicle have been obtained from the specifications of the products and the parameter estimation in previous works. Nevertheless, it is still necessary to fine tune these parameters to achieve the desired behaviour to be consistent with the true physical system.

This objective is achieved by the method of trial and error. The data obtained from previous works are used as the initial values of the parameters to be tuned. The simulation responses of the tuned system are compared with the test results for developing the old model in Section 4.3.1. The iterative process was used to refine the values until the responses of the new model and the real system are closely matched. To simulate the actuator locking in the mathematical model as the same as the real system test in Section 4.3.1, some state variables are set to zero to restrict the movement of the car body and therefore that of the cylinders.

Figure 6.2 shows the simulation response of the pressure P_1 in the fluid chamber of the new model when a control signal of 70 bar pressure is applied to the servo valve. The experimental data of the actuator-locked test are shown in Figure 6.3. It can be seen that from Figure 6.2, it takes approximately 15 ms for the active HIS to reach its transient state in the locked condition which is similar to the experimental response in Figure 6.3.

However, it is noted that the real system does not exactly reach the target value 70 bar. This phenomenon cannot be observed in the simulation response. It is probably because of the limitation of the pressure control unit that is not included in the new system model. This phenomenon could be brought about by the power restriction in the motor-bump setup.

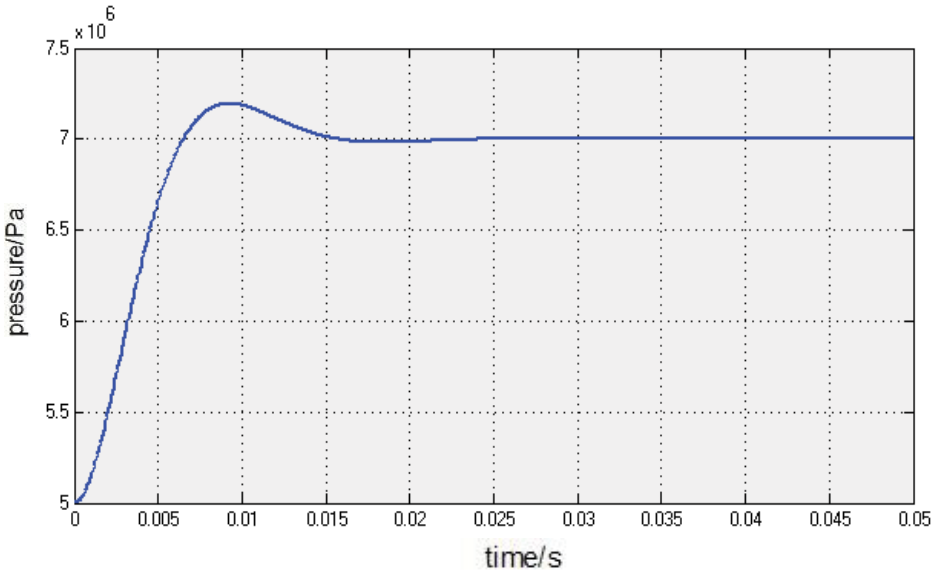

Figure 6.2 Simulation response of the pressure P_1 in the fluid chamber

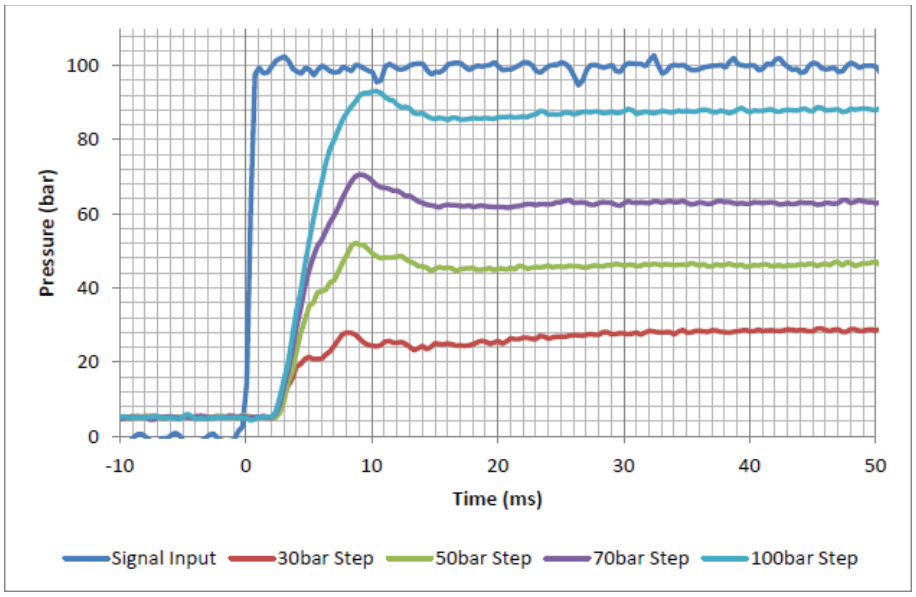

Figure 6.3 Experimental results of the locked-actuator test

In the process of tuning parameters, to align the new model with the real system in their performances, particular emphasis was laid on the friction coefficients of the pipe wall and the viscous fluid damping. The fine-tuned parameter values and the corresponding reference values of the integrated system model are provided in Table 6.1.

Table 6.1 Tuned system's parameters compared to given ones

Parameters	Value	Reference Value
m_s – Half sprung mass (kg)	950	900
m_u – Unsprung mass (kg)	41	42
I – Half roll moment of inertia (kg*m2)	388	435
k_t - Tyre stiffness (N/m)	$2.7 *10^5$	$2 *10^5$
k_s – Suspension spring stiffness (N/s)	$4.4 *10^4$	$4 *10^4$
C_s – Suspension damper coefficient (Ns/m)	2507	$2 *10^3$
l - Distance from CG to a suspension (m)	0.5	0.575
A_{pu} – Upper piston cross-sectional area (m^2)	$5.1 *10^{-4}$	$5.1*10^{-4}$
A_{pd} – Lower piston cross-sectional area (m^2)	$4.1 *10^{-4}$	$4.1 *10^{-4}$
E – Bulk modulus of the hydraulic oil (MPa)	1400	1400
L – Pipe length from valve to actuator (m)	1.0	1.0
G – Controller gain in the servo valve	$1.5*10^{-9}$	Not given
s – Initial fluid height in the chambers (m)	0.075	Stroke 0.15m
C_p – Fluid viscous damping coefficient	$5 *10^6$	Not given
Re – Pipe friction coefficient	$1 *10^4$	Not given
ρ – Hydraulic oil density (kg/m^3)	870	870

6.4 Model verification and characteristics study

To validate the new active HIS model, two tests are implemented. The test data of the real system are logged and compared with the simulation results of the new model. Moreover, the responses of the old model are also included in the comparison to illustrate the difference between the new and old models.

The model validation tests are conducted on the active HIS equipped SUV test rig introduced in Chapter 4. In the tests, the hydraulic cylinders are charged with different pressures. The responses of the real system are compared with the results of the new model in simulations to validate the effectiveness and robustness of the new model. The comparisons of the pressures in the top and bottom chambers, roll angles and suspension

deflections at the left and right wheels are provided. The pressure responses are measured by the pressure sensor inside the cylinder chambers. The suspension deflection responses are obtained by the LVDTs between the sprung and unsprung mass. The data of the roll angles are calculated from the signals of the two LVDTs that are mounted between the left and right sides of the vehicle and the ground.

It is noted that the test data presented in this section are not converted to their physical units but are still in volts that are the raw voltage signals logged from the sensors. It is applicable for the reason that the relation between the measured sensors' signals and the variable values are linearly dependent. Thus, the waveform of the variables that is the primary focus of the experiment is retained.

6.4.1 25 and 50 bar control signals input at the same time

In this test, a 25 bar and a 50 bar pressure control signals are send to the servo valve to increase the pressures in the upper and lower chambers of the hydraulic cylinders respectively. The two control signals are input to the servo valve controller simultaneously. The simulation and experiment results are shown as follows.

6.4.1.1 Pressure Response

The pressure responses of the upper and lower chambers of a hydraulic actuator in the experiment and simulation are provided in Figure 6.4 and Figure 6.5 respectively. It can be seen that the simulation and experiment results presented very similar pressure responses in both upper and lower chambers. The results suggest that the pressure responses inside the fluid chambers can be estimated by the new model accurately.

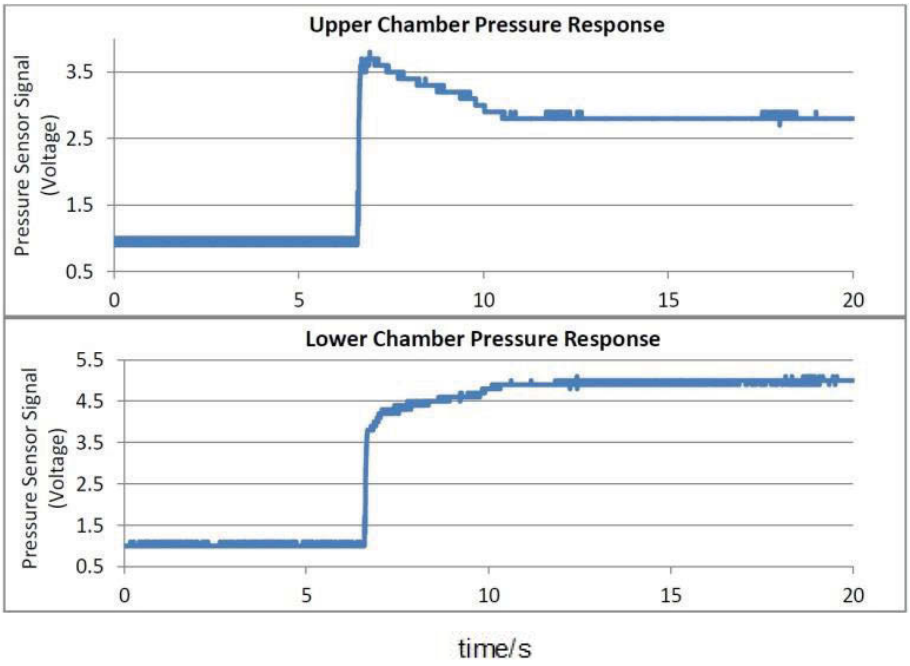

Figure 6.4 Pressure responses of top and bottom chambers in experiment

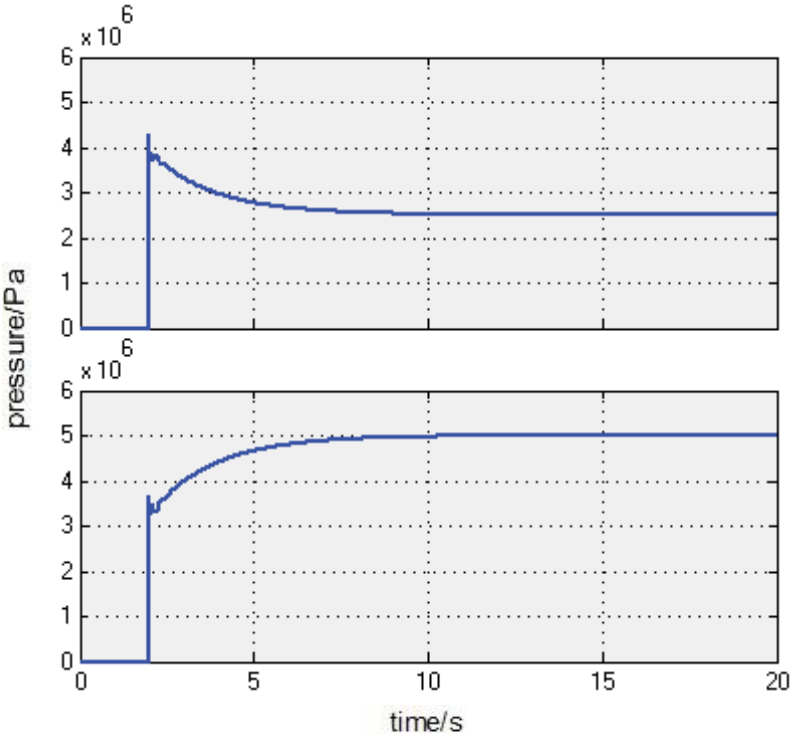

Figure 6.5 Pressure responses of top and bottom chambers in simulation

The top graphs in Figure 6.4 and Figure 6.5 show the top chamber pressure responses and the bottom graphs show the bottom chamber pressure responses. Both the simulation and experiment results show that when different pressure control signals are sent to the servo valve, the fluid pressures in the top and bottom chambers increase to similar pressures immediately, but it takes several seconds to reach the objective pressures. It is due to that when the pressure in one chamber of the hydraulic cylinder increases suddenly, it will push the piston to reach equilibrium immediately. The results demonstrate that the active HIS is able to provide control forces as soon as the control signals are applied, but there is a system time delay before generating desirable control forces to the vehicle body.

6.4.1.2 Roll Angle

The experiment and simulation results of the roll angle responses under the condition that the two hydraulic circuits are charged with 25 and 50 bar at the same time are shown in Figure 6.6 and Figure 6.7, respectively. From the graphs, similar roll angle responses of the real system test and the model-based simulation can be observed, which indicate that the new model can describe the behaviour of the test vehicle accurately.

Considering the rise time, it takes longer time for the mathematical model to reach steady state than the real system. It is because of the absence of the accumulator in the model. In the test, due to the limitation of the power provided by the hydraulic accumulator, the active HIS system cannot take the vehicle body to its target roll angle, so the rise time of the physical system is shorter for a smaller transient roll angle. However, as can be seen from Figure 6.7 it reaches 85% of the transient roll angle of the physical system in three seconds. Thus, the estimated roll angle by the system model is satisfactory.

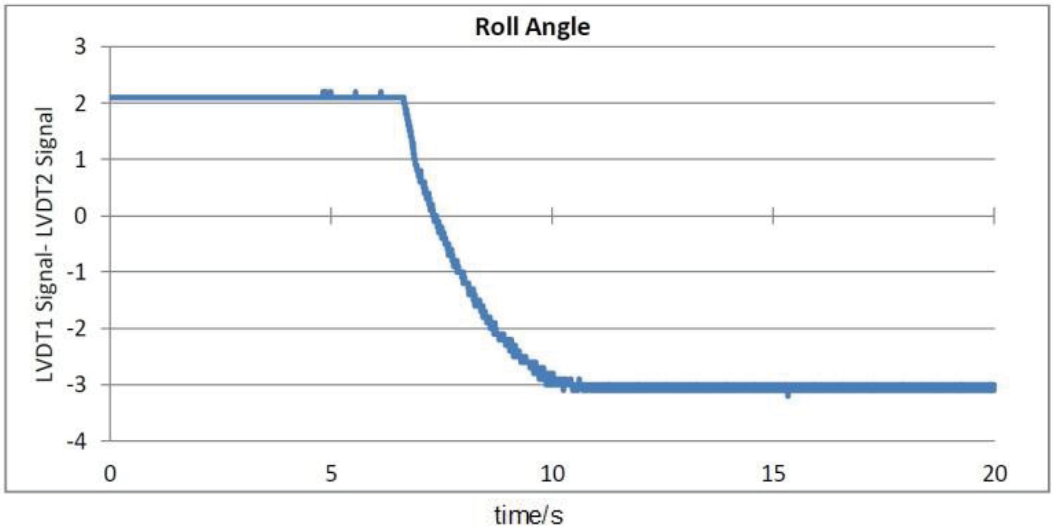

Figure 6.6 Roll angle responses in experiment

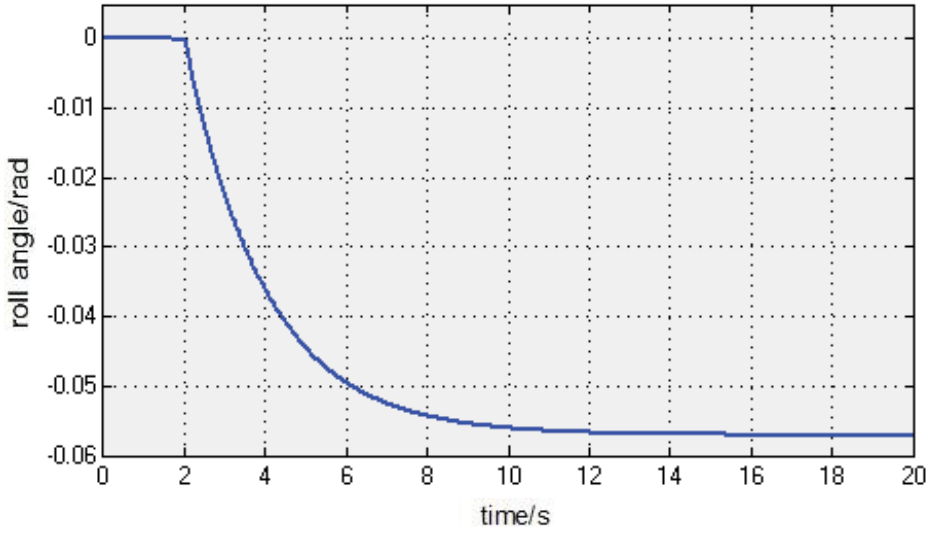

Figure 6.7 Roll angle responses in simulation

6.4.1.3 Suspension deflection

Figure 6.8 and Figure 6.9 show the experiments and simulations results of the wheel vertical displacements relative to the vehicle body, namely the suspension deflections. Similar to the fluid pressures and the roll angles, the suspension deflections also show similar responses in

the experiments and simulations. In Figure 6.8, it takes approximately four seconds to reach the steady state in the experiment that is similar to the simulation results in Figure 6.9.

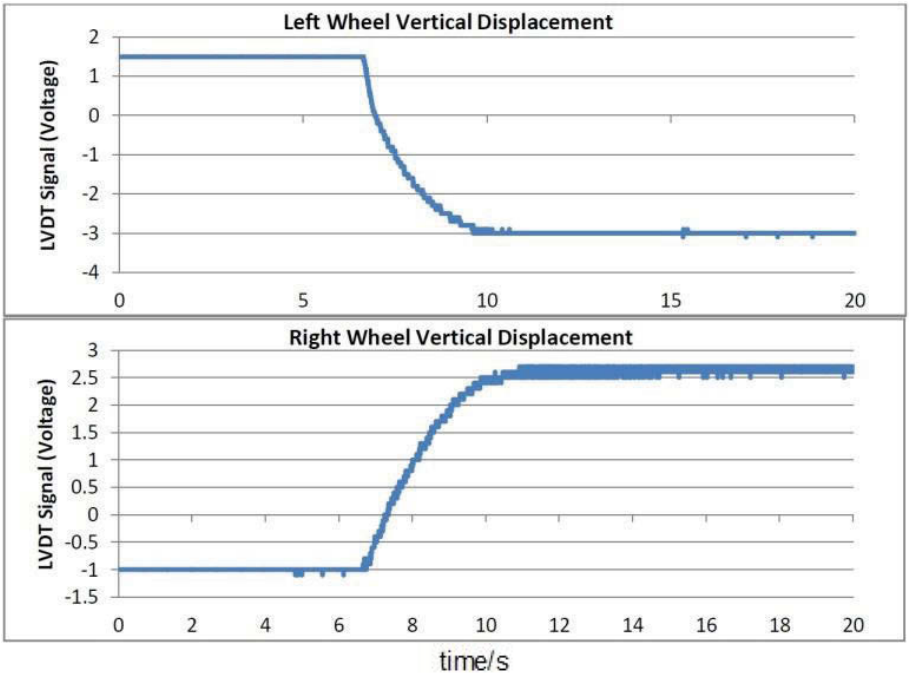

Figure 6.8 Suspension deflection responses in experiment

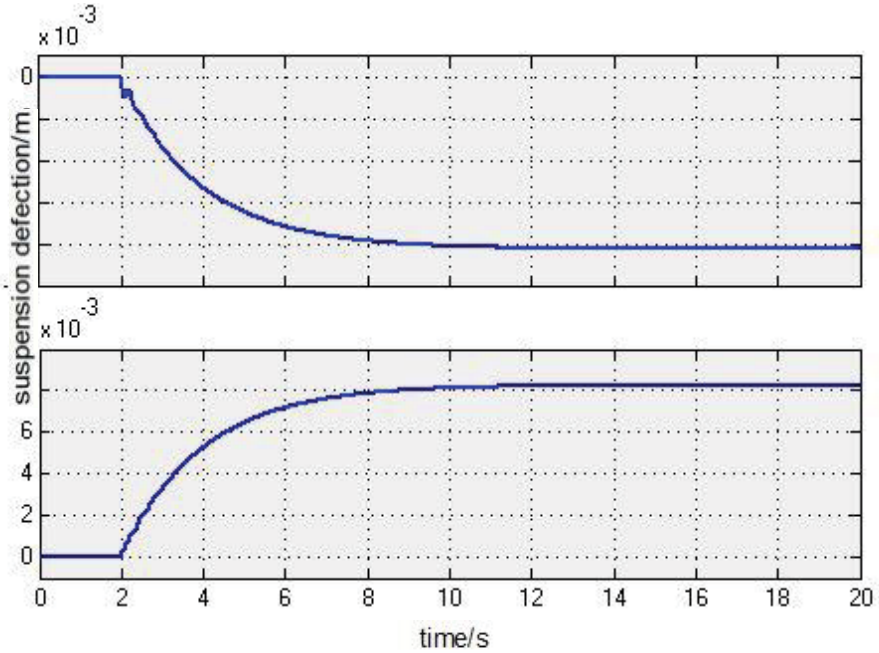

Figure 6.9 Suspension deflection responses in simulation

6.4.2 25 and 50 bar control signals input with 1 second delay

In this test, a pressure control signal of 25 bar is sent to the servo valves for the one hydraulic circuit, and one second later, another pressure control signal of 50 bar is sent to the servo valve for the other hydraulic circuit. More complicated control signals than the previous test are used in this test, which takes the robustness and accuracy of the new model into consideration. The simulation and experiment results are shown as follows.

6.4.2.1 Pressure Response

Figure 6.10 and Figure 6.11 show the pressure responses of the upper and lower chambers in the hydraulic actuators in the experiment and simulation. The plots at the top of Figure 6.10 and Figure 6.11 show the pressure responses of the upper chamber and the bottom plots show the pressure responses of the lower chamber. It can be seen that the curve shapes in the simulation and test are well matched and the rise time is around 6 seconds. The results reconfirm the accuracy of the model.

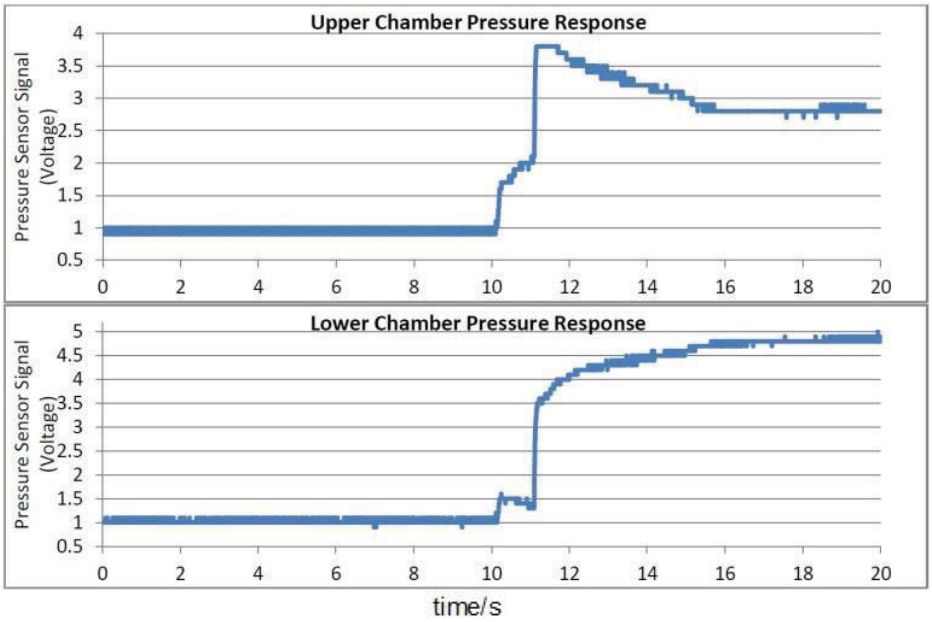

Figure 6.10 Pressure responses of top and bottom chambers in experiment

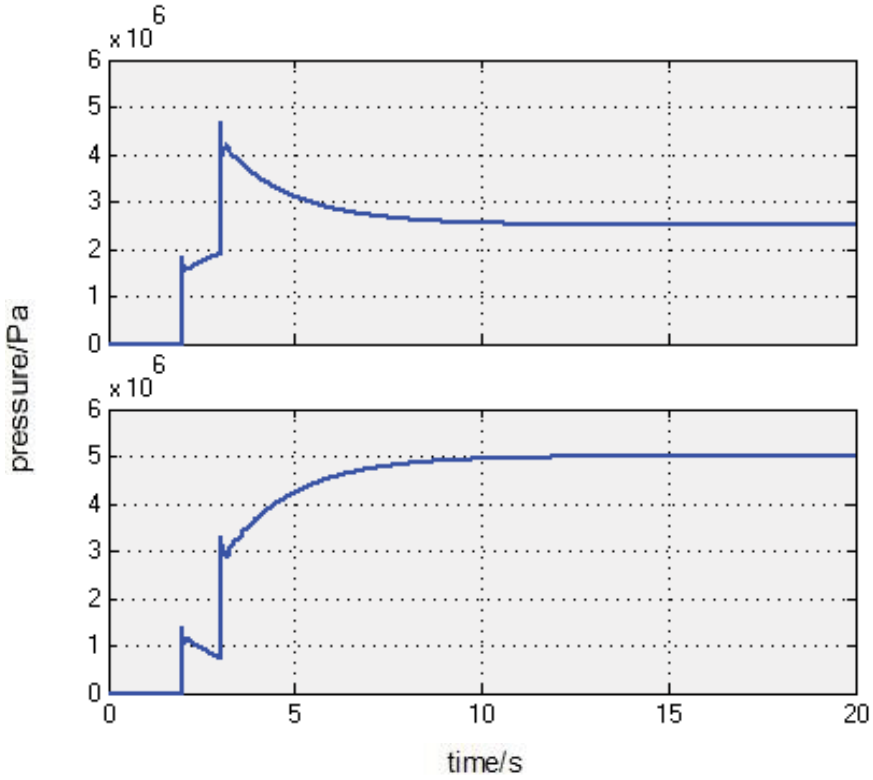

Figure 6.11 Pressure responses of top and bottom chambers in simulation

6.4.2.2 Roll Angle

The experiment and simulation results of the roll angles are presented in Figure 6.12 and Figure 6.13. Similar to the first test, although the curve pattern of the results of the simulation is consistent with the experimental results, the rise time of the simulation and the experiment is not the same. It is 5 seconds in the experiment but 10 seconds in the simulation. As mentioned above, without considering the accumulator in the model development, the physical limitation cannot be described by the new system model. However, because the mathematical model can achieve 80% of the maximum roll angle in five seconds, its accuracy is satisfactory.

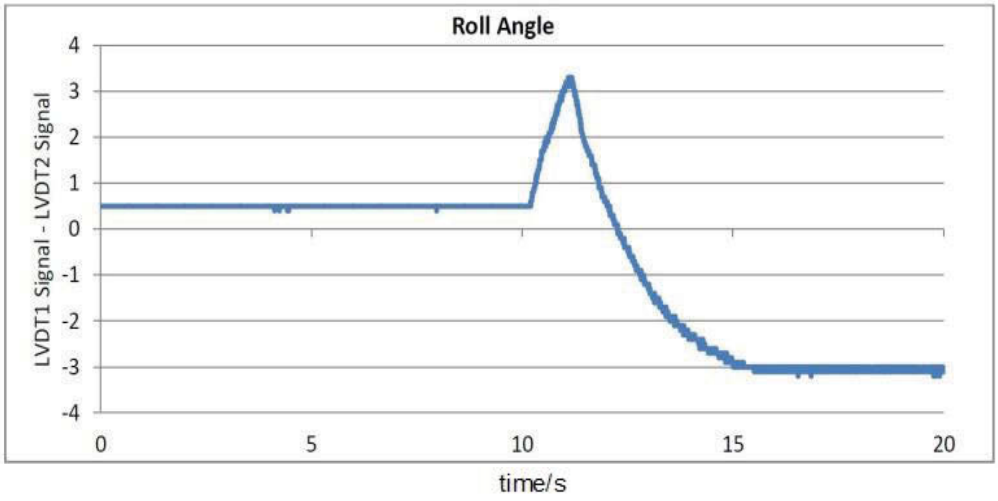

Figure 6.12 Roll angle responses in experiment

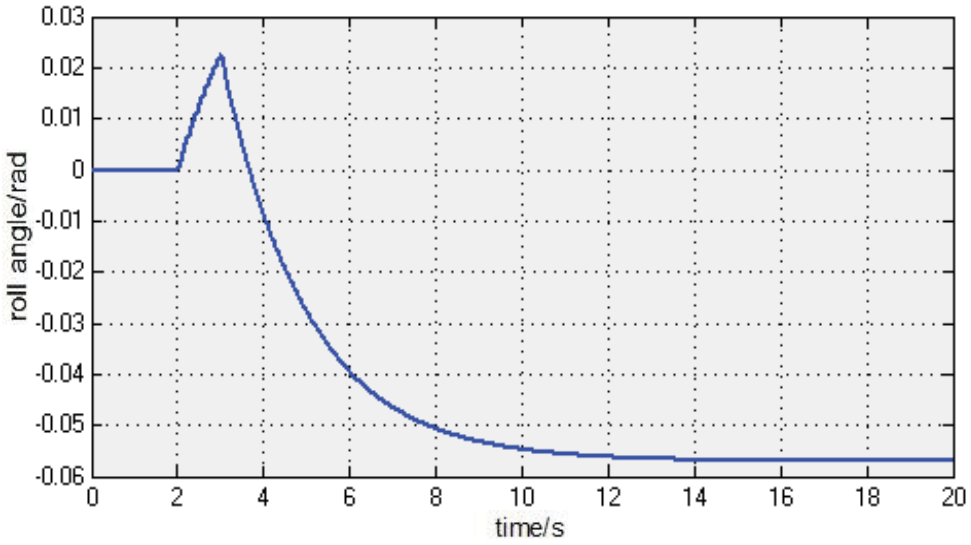

Figure 6.13 Roll angle responses in simulation

6.4.2.3 Suspension deflection

In Figure 6.14 and Figure 6.15, the suspension deflection of the left and right wheels in experiment and simulation are provided. It can be observed that the suspension deflections responses of the new model matched well with those of the real system. Thus, the accuracy of the developed new model can be validated by the results presented above.

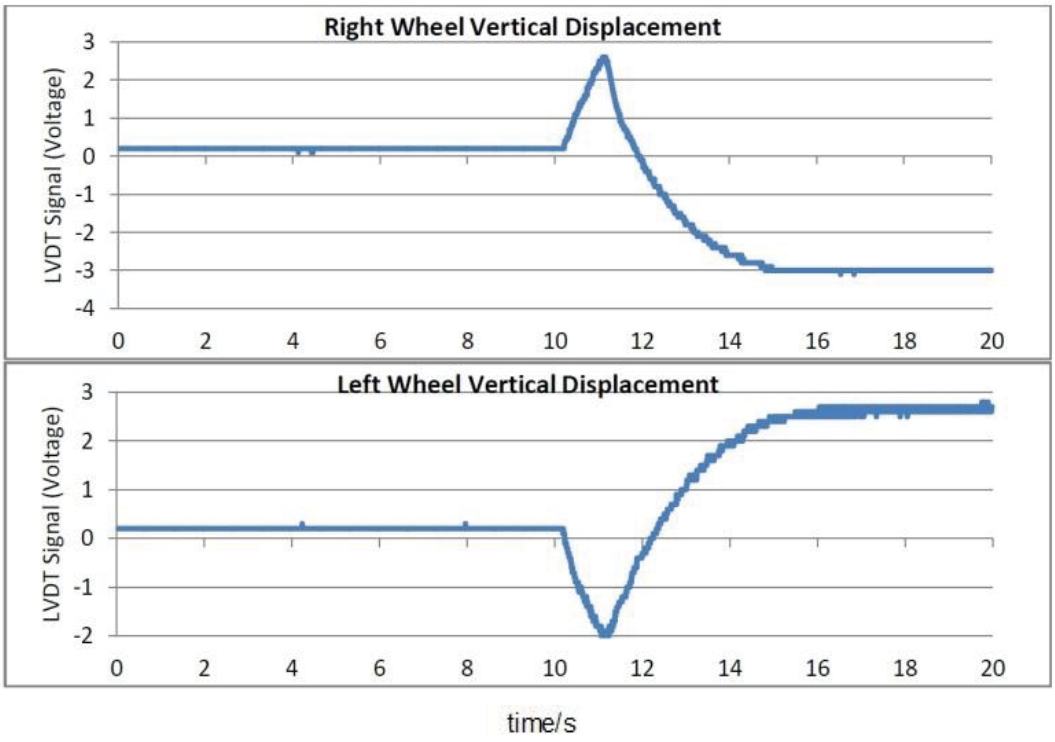

Figure 6.14 Suspension deflection responses in experiment

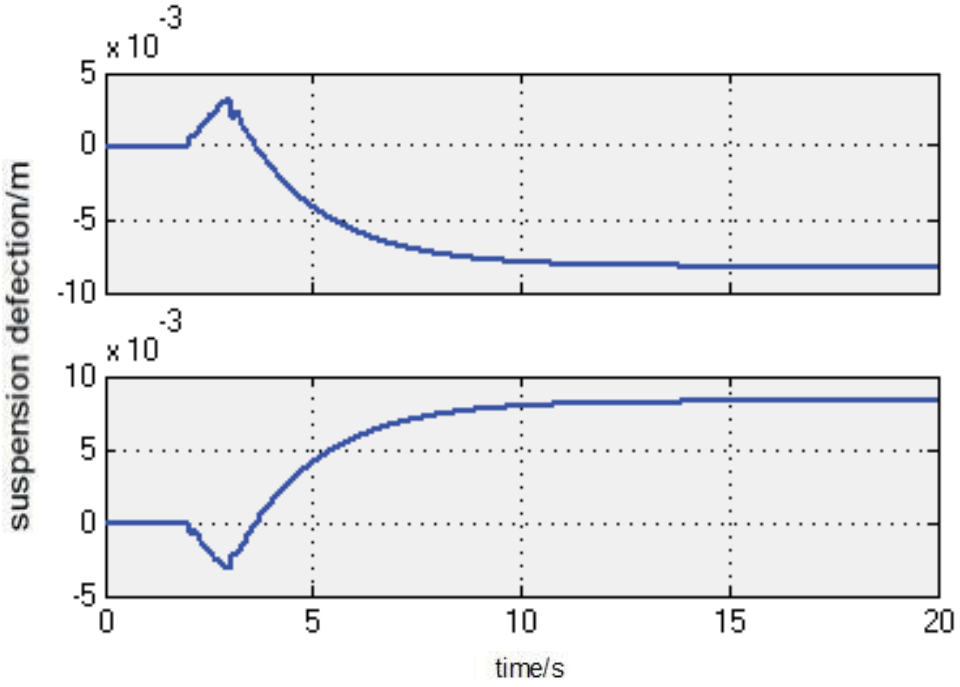

Figure 6.15 Suspension deflection responses in simulation

6.4.3 Comparison with the old model

After obtaining the accurate model and test data, the new model's response is compared with the system response of the old model. Figure 6.16 shows the difference of the roll angle responses of the old model with the physical system response in Figure 6.6 and the new model response in Figure 6.7. As shown in Figure 6.16, apparent oscillation can be observed from the data curve of the roll angle response. It is due to the theoretical assumption in the development of the old model. Without considering the fluid flow and flow related factors (i.e. fluid damping and pipe friction), the system response of the old model is distinct from the behaviour of a general hydraulic system. Hence, it can be concluded that the new model is able to describe the real system better than the old model.

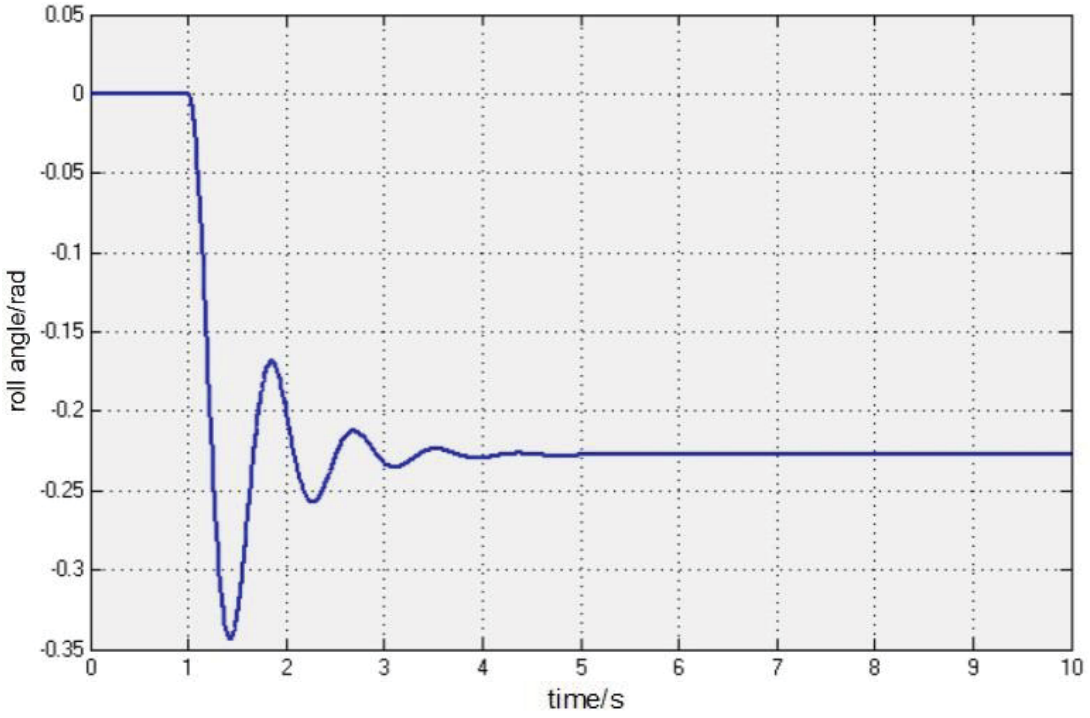

Figure 6.16 Roll angle response of the old model under the control signals input simultaneously

6.5 Controller design and implementation

6.5.1 Control method

6.5.1.1 H∞ Control Method

The H∞ control algorithm can be used to develop H∞ output feedback controllers for the control problem with limited measurements, and can be also applied to design H∞ state feedback controllers that can address the control problem with multiple inputs, outputs and control criteria. Furthermore, for a particular model, the optimal control signals can be easily generated through the H∞ control method. The H∞ controller development can be done by the MATLAB toolbox.

As mentioned in Section 6.1, understanding the dynamics of the active HIS thoroughly and developing an accurate system model are necessary for a successful application of the model-based control algorithm. One of the benefits of the H∞ control is that it is capable of generating a satisfactorily compensated response for the system resonance compensation and bandwidth limiting.

Generally, the H∞ control problem is an optimisation control problem. However achieving optimal control signals raises the possibility of obtaining unstable controllers. Hence, it is pivotal to balance the two conflicting criteria between the system stability and optimal feedback. This objective can be achieved by applying the H∞ loop-shaping techniques.

The advantages and disadvantages of applying the H∞ control algorithm to the active HIS are the focuses in this research. A similar method to Section 4.4 is used for an output feedback controller design. Figure 6.17 is the schematic diagram of the plant with the H∞

output feedback controller, where $\mathbf{d}_4$ is the sensor noise and external disturbance during the measurement and W_n is the weighting function of $\mathbf{d}_4$; **y** is the measured output, namely the roll angle of the vehicle body in this study. In the test, the roll angle of the sprung mass is obtained by the two ground-connected LVDTs mentioned earlier.

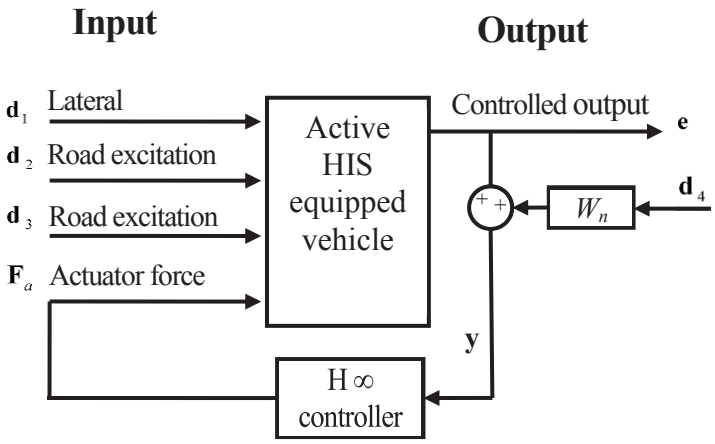

Figure 6.17 Schematic diagram of the plant with the H∞ output feedback controller

6.5.1.2 LQR Control Method

The LQR control algorithm is used to deal with the optimal control problem by solving the Riccati equation for the minimum cost. For achieving this target, full state feedbacks of the to-be-controlled system are necessary. The LQR control algorithm can calculate the optimum control signals automatically for the plant based on a compensation matrix containing the weighting factors of each feedback state signal.

Figure 6.18 shows the schematic of the controlled system, where **K** is the gain matrix of the LQR controller, **r**(t) is the external disturbance, **x**(t) is the full state feedback, **u**(t) is the control input, **e** is the controlled output. Commonly in designing an LQR controller it is

necessary to find a proper gain matrix **K** through tuning the weighting factors, which produces a control input **u** to stabilise the system.

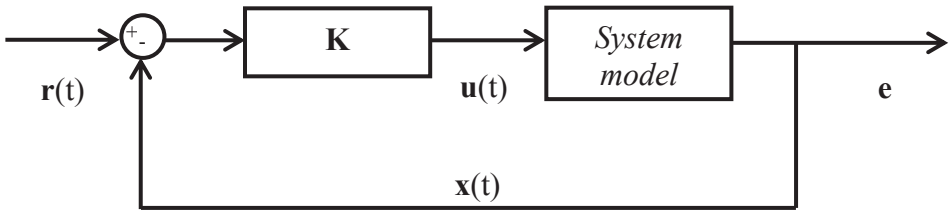

Figure 6.18 Schematic diagram of the plant controlled by a LQR controller

The same as in the H∞ method, a balance between the optimum control signals and the stability of the active-HIS-vehicle-integrated system needs to be kept. When tuning the controller, the system instability is exaggerated by improper parameters. The weighting matrix inherited flexibility enables control engineers to adjust the behaviour of the system manually through control criteria set by them. In other words, tuning the weighting factor of a certain state variable would mitigate or magnify the effect of the state variable on the control signals.

In this study, a set of appropriate weighting factors is obtained through the trial-error method. Therefore, it is possible for improving controller performance by further tuning the weighting coefficients. Because a full state feedback is required in the LQR controller implementations, but the measurement of some state variables in the system (e.g. the roll angle acceleration and speed of fluid flow) is not accessible in reality, the designed LQR controller is only implemented in the simulation but not in the test.

6.5.2 Simulations

The designed LQR and H∞ controllers are validated on the new system model in simulations with five sets of lateral excitations, namely the lateral excitation with impulse input, step input, fishhook input, slalom and sinusoidal input. The roll angle responses of the system controlled by the LQR and H∞ controllers are presented and compared with the vehicle response without control as follows.

6.5.2.1 Lateral excitation with impulse input

Figure 6.19 shows the simulation results of the lateral impulse excitation. Figure 6.19(a) gives the input signal of the impulse excitations, which is equivalent to a lateral input of gravitational acceleration acting on the sprung mass. It can be seen from Figure 6.19(b) that both the controllers respond fast to a sudden disturbance. With the H∞ and LQR controllers conducted, the roll angle reduces approximately 40% and 50% respectively. Compared with the H∞ controller, the LQR controller shows faster response and less overshoot.

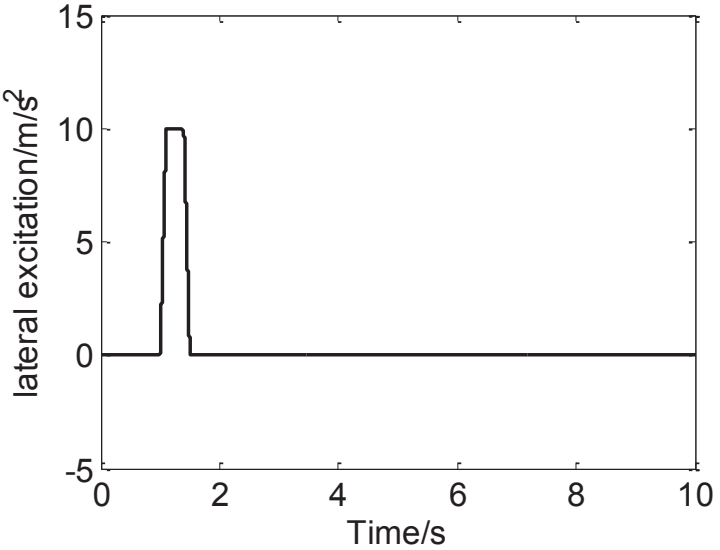

(a) Excitation signal

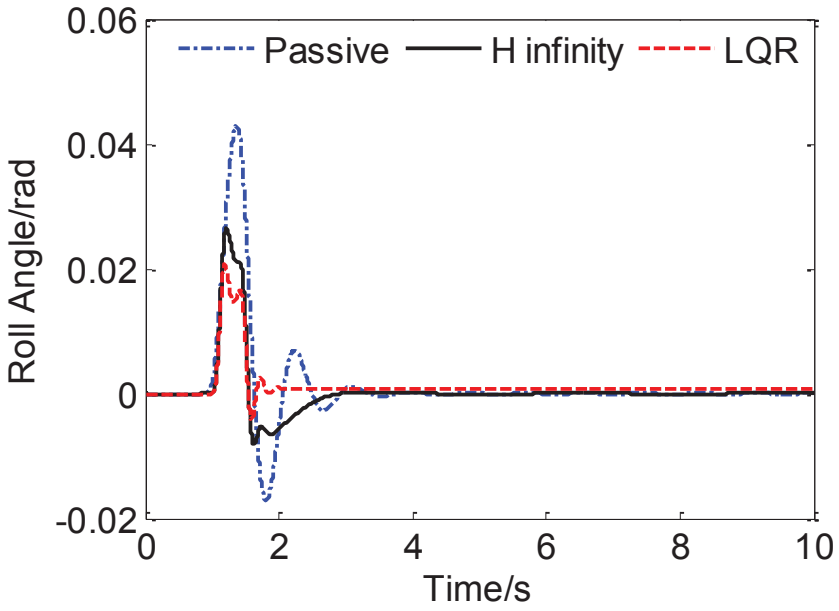

(b) Roll angle response

Figure 6.19 Simulation roll angle response under impulse lateral excitation

6.5.2.2 Lateral excitation with fishhook input

This simulation employs a fishhook excitation on the vehicle body. The excitation signal and the roll angle comparison are shown in Figure 6.20(a) and Figure 6.20(b). As shown in Figure 6.20(b), both H∞ and LQR controllers reduce the roll angle substantially, with around 90% decreases. In contrast with the H∞ controller, a smoother roll angle response can be observed from the curve of the LQR controller. However, the inherited drawback of the LQR control algorithm from the use of the weighting matrices is revealed. Under the LQR control, the transient state of the roll angle is not stabilised at 0 radians. On the other hand, the H∞ controller is found to be more effective with a more stable response, although its peak value is slightly larger.

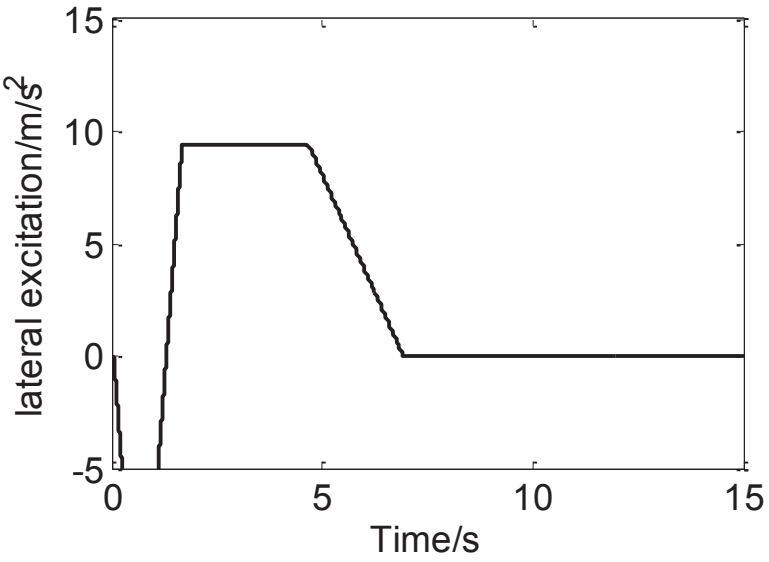

(a) Excitation signal

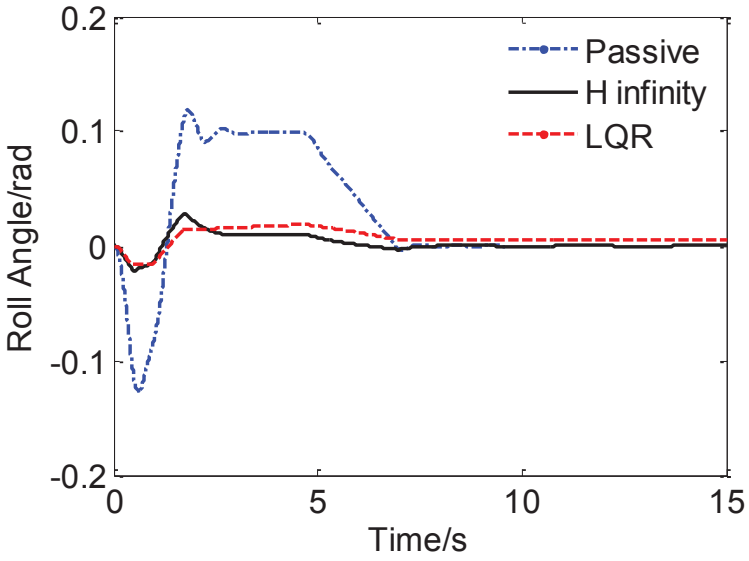

(b) Roll angle response

Figure 6.20 Simulation roll angle response under fishhook lateral excitation

6.5.2.3 Lateral excitation with slalom and sinusoidal input

The simulation results under the slalom and sinusoidal excitations are presented in Figure 6.21 and Figure 6.22 respectively. In these two simulations, the LQR controller performs

slightly better than the H∞ controller with a larger roll angle reduction and smoother responses. However, the control performances in these two simulations are not as good as in the fishhook simulation. Only about 50%~70% roll angle reduction can be achieved. It is due to the controllers' limitation in response time. Compared with previous simulations, it is found that the performance of the controller depends on the frequencies of the excitations.

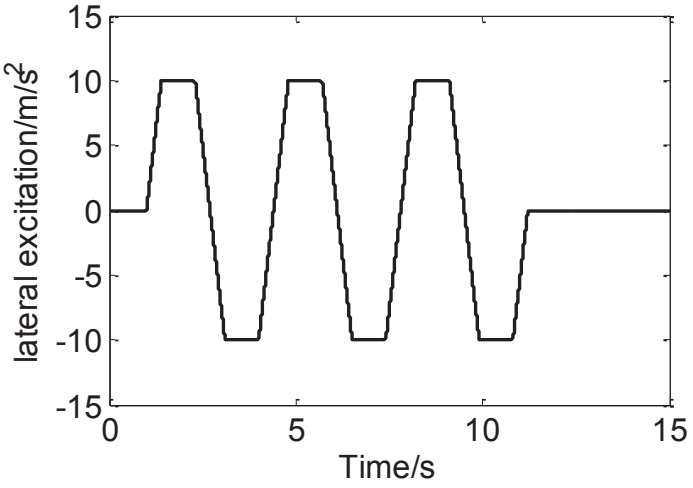

(a) Excitation signal

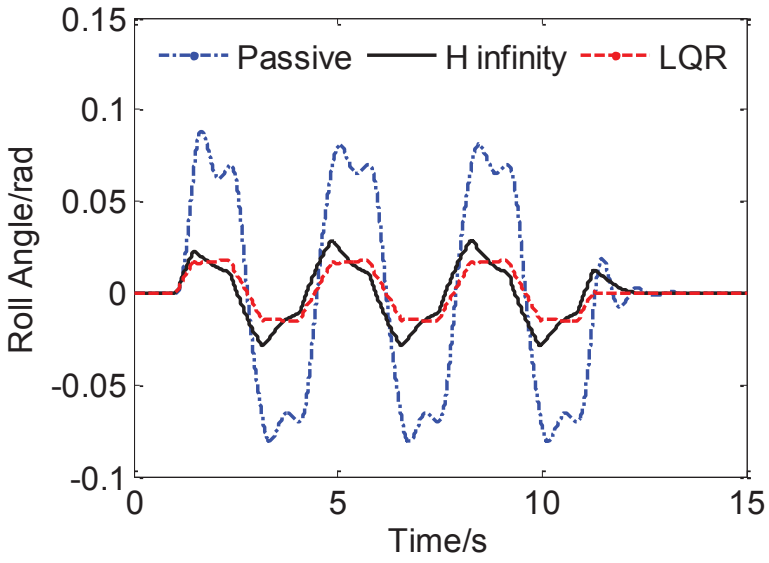

(b) Roll angle response

Figure 6.21 Simulation roll angle response under slalom lateral excitations

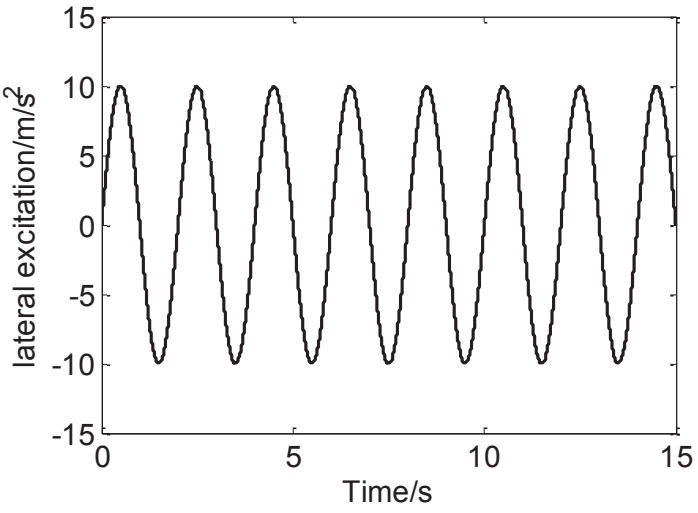

(a) Excitation signal

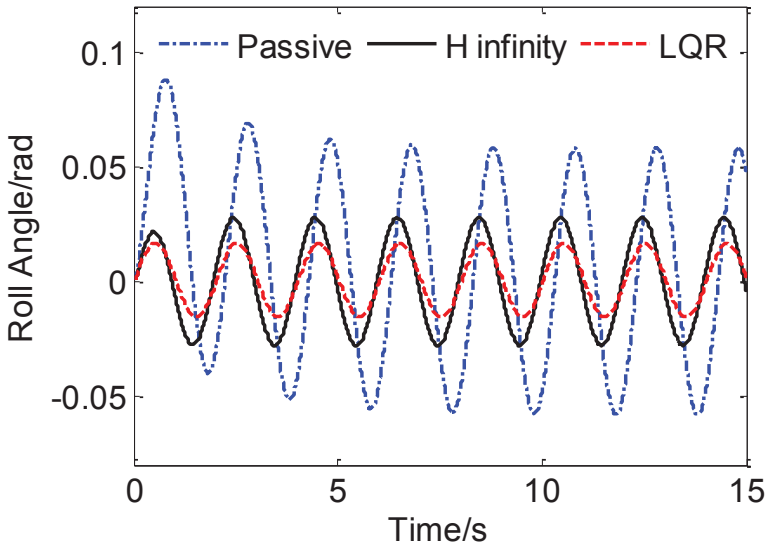

(b) Roll angle response

Figure 6.22 Simulation roll angle response under sinusoidal lateral excitations

6.5.3 Experimental validation

As mentioned above, due to the lack of the measurement of some state variables, only the designed H∞ controller is validated in the experiment. As shown in Figure 6.23(a), a set of out-of-phase ground excitations with single sine signal act on the left and right tracks of the

test vehicle. The roll angle response in the H∞ control case is compared with its counterpart of the previously designed H∞ controller in Section 4.5.2.3. It can be seen from Figure 6.23(b) that the H∞ controller derived from the new system model improves the control performance slightly with a small drop of roll angle and reduced oscillations.

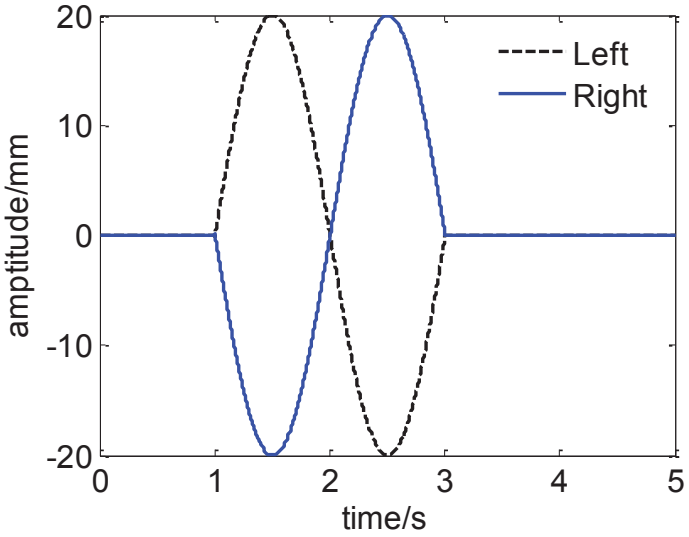

(a) Ground excitations

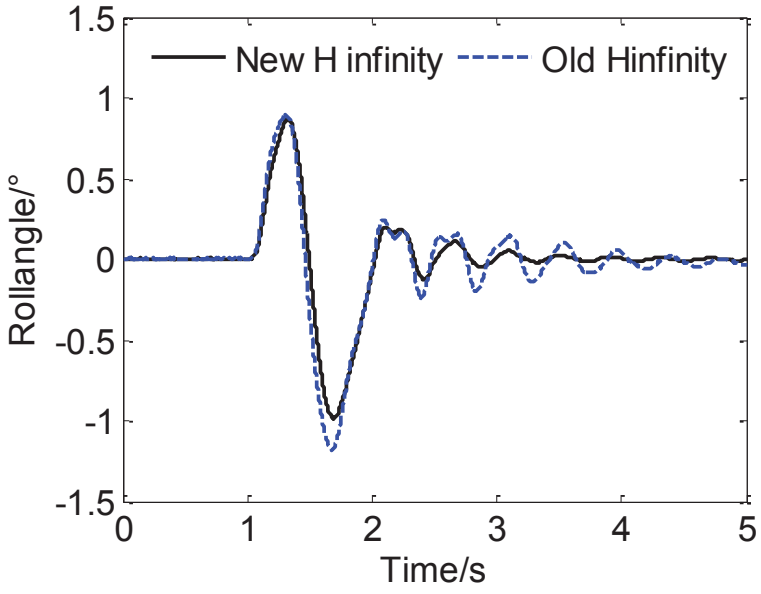

(b) Roll angle response

Figure 6.23 Experimental roll angle responses under single sine road excitations

6.5.4 Discussion

6.5.4.1 Mathematical model development

The parameter tuning played a vital role in identifying the inconsistencies and errors within the model. While the performance of the mathematical model was tuned similarly to the performance of the physical system, the significant factors that affect the system's behaviour were added or identified. For example, in the old model, because the rise time of pressures in the actuator chambers was almost instantaneous, the working fluid damping and pipe friction were added to combat the problem of the old model's failure to produce a reasonable and realistic rise time. Adjusting these two coefficients changed the new model's characteristics accordingly, such as the speed of the working fluid and pressure rise time. Other inconsistencies about the sign convention were also recognised because of some unrealistic results reflected in the responses of the incorrect model.

However, the parameter tuning was only a small step towards producing a satisfactory system response. The new model developed in this chapter was tuned against the test data of a locked hydraulic actuator. However, the test with the locked actuator merely verified the pressure response of the hydraulic cylinder, while the flow in the system was not addressed. That is, the obtained system model would not necessarily estimate the flow of the working fluid in the system accurately even though the tuned performance matched well with the test data. More tests, particularly the tests about the fluid flow, need to be conducted to build a database on a large enough scale so that the mathematical model can be further tuned with other available experimental data, and thus a more accurate system model can be developed.

In the beginning, the system model was built as a complex, non-linear model. However, the model-base advanced controllers, such as H∞ and LQR controllers, cannot be derived based on a nonlinear model. Hence, the nonlinear model was linearized by the Taylor expansion technique. Unfortunately, the obtained model was too complicated to be well tuned. Specifically, the model tuning was a trial-error process, so it depended largely on luck and tuning such a complicated model would take an unacceptably long time.

6.5.4.2 Control methodologies

In the simulations, the H∞ and LQR controllers had achieved satisfactory performance because the fluid flow and damping are added to the system model. However, because of the absence of the sensors on the test rig for measuring the flow rate in the fluid system, the LQR controller could not be experimentally implemented. For the future work, this problem can be addressed by the LQG control. A Kalman filter, which is used to estimate an adequately accurate full state from only a few available measurements of output signals, is needed to be added to the LQR controller for the LQG controller development.

Figure 6.24 and Figure 6.25 exhibit the pressure responses in the hydraulic system under the H∞ control and the LQR control respectively. Both the two hydraulic circuits were pre-charged with 20 bar pressure as the system initial pressure. In Figure 6.24, it can be seen that the H∞ controller charges both chambers to make the pressures larger than the initial value, but since the pressure in one chamber is higher than in the other, the hydraulic actuator still produces control force to the vehicle chassis. However, as shown in Figure 6.25, the LQR controller presents a much more efficient behaviour with decreasing the pressure in the one chamber and increasing it in the other.

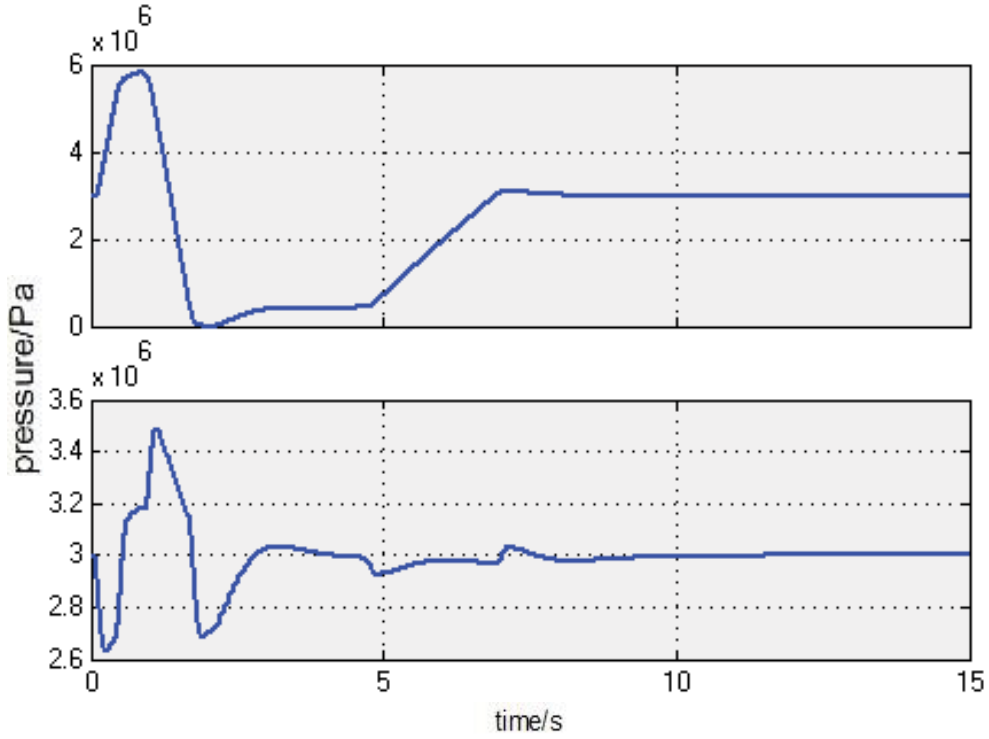

Figure 6.24 Simulation pressure responses inside the chambers under the H∞ control

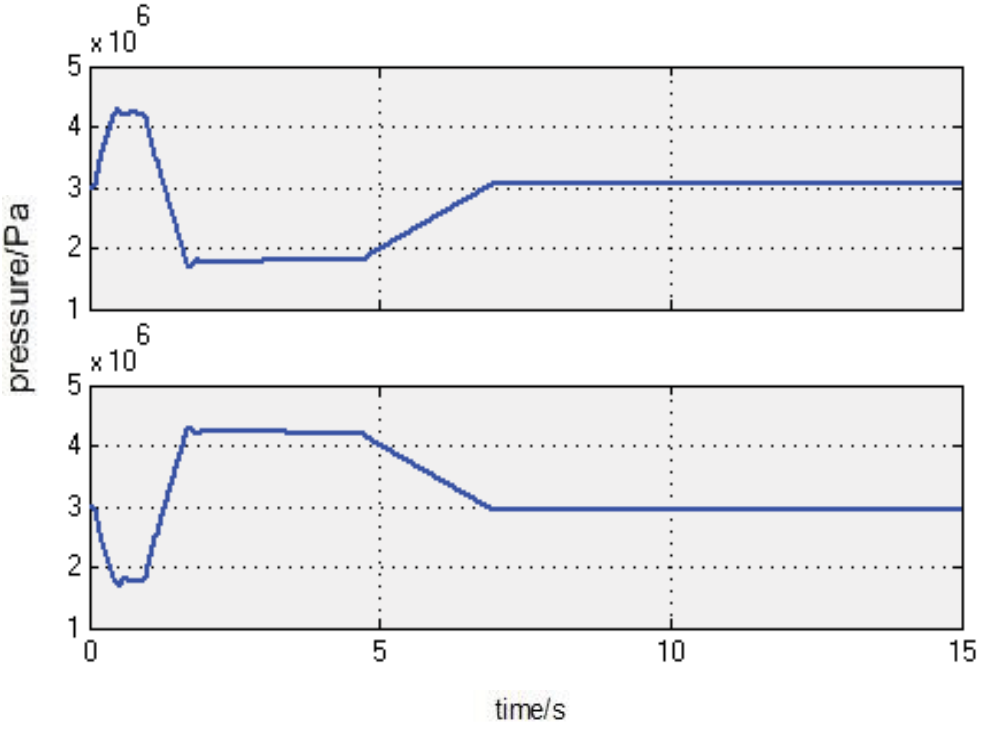

Figure 6.25 Simulation pressure responses inside the chambers under the LQR control

The LQR controller had greater flexibility regarding the control criteria adjustment and performance tuning due to the included weighting matrices. However, the presence of a large number of state variables made it a time-consuming process to find proper weighting matrices. The considerable decrease of the vehicle body roll angle when the LQR controller was applied in the simulations was enough to demonstrate the effectiveness of the controller.

6.5.4.3 Active HIS duty cycle limitation

As produced in Chapter 2, an accumulator and a pump for powering the hydraulic circuits was included in the control unit of the active HIS.

The accumulator provided a complement to the working fluid to shorten the response time of the system. However, since the volume of the hydraulic accumulator was limited, the accumulator was not able to maintain the flow compensation for a long time. Once the fluid pressure dropped to be equal with the outside, the accumulator had to be recharged before working by the motor-pump setup concluding a duty cycle in the system. This duty cycle in large motions was around five seconds. In other words, the active HIS system is not capable of maintaining or increasing the pressures in the hydraulic actuators for longer than five seconds in continuous large roll motion.

However, in the real world, when the vehicle is under lateral excitations, the active HIS only needs to maintain the levelling of the vehicle body. In this situation, large flow is unnecessary. On the other hand, the vehicle under road excitations for roll motion over a long period rarely exists. Overall, the duty cycle of the system is also not a concern due to the capability of the active HIS for handling lateral excitations and sudden road excitations.

6.5.4.3 The limitation of the test facility

Because of the limitation of the test facility, the ground excitation results are used to verify those of the lateral excitation. Because for the active HIS, the control feedback signal is the roll angle. The ground excitation is used to stimulate the vehicle roll motion which is the same as the lateral excitation, so I think the experimental results can verify the lateral excitation well.

6.6 Summary

In this chapter, a new mathematical model of the active HIS system was developed with the fluid flow, hydraulic system damping and their associated time delay included. This new model made it possible to study the characteristics of the active HIS further and, therefore, obtain more understanding regarding the system. The new state variable, namely the fluid flow, considered in the model development had given deeper insight into the behaviour of the system than the old model.

The model validation was conducted by comparing the system response in the simulation and experiments with different pressure control signals sent to the servo valve. Even though there were some differences in the rise time of the roll angle since the accumulator and pump were not considered in the new model, the responses of the new model reflected the real system's performance very well. The results demonstrated that the new model was able to produce a fairly accurate estimation of the system behaviour.

Furthermore, the obtained new model provided a platform with strong compatibility, on which the onwards study could be carried out. The further investigation concerning the

effects of the pump and accumulator could be conducted and the relevant equations could be integrated into the obtained system model by replacing the pressure P_2 and P_4.

Based on this new model, the designed LQR and H∞ controllers were validated in the simulations with different lateral excitation applied to the sprung mass. The roll angle responses of the active HIS equipped under the LQR and H∞ control were compared with their counterparts of the vehicle without the active HIS. The simulation results verified the effectiveness of the LQR and H∞ controllers with fast response time and the significant reductions in the roll angle. It was also noticed that the control performances were related to the frequencies of the excitations exerted on the vehicle body. The H∞ controller was also validated experimentally and compared with the old H∞ controller in Chapter 4. The new H∞ controller provided better control performance than the old one with a small further reduction in the roll angle and an apparent improvement in reducing the oscillations.

7 Delay-Dependent H∞ Control

7.1 Introduction and rationale

In this section, an attempt is made to reduce the effects of the time delay caused by the system on the control performance. To do this, the four-DOF half-car mechanical system introduced in Chapter 4 is used to construct the H∞ control problem.

A state feedback H∞ controller without time delay is designed first. The related H∞ control problem is solved by the linear matrix inequality (LMI) approach. The obtained H∞ controller is validated by simulations with step input and fishhook input from the round. The suspension deflection and roll angle with control and without control are compared.

The delay-dependent state feedback H∞ controller is then also obtained with the LMI method. The simulation results of the vehicle under step input are presented. The control responses of the delay-dependent H∞ controller without time delay and with 15 ms time delay are compared with the results without active control.

7.2 Background

Some works of analytic H∞ controller design methods were presented in the 1990s [124, 125]. After this, the software toolbox was developed in 1995 [126]. As a result, a number of design methods of the state feedback controllers for time-delay systems were proposed in recent decades. A memory-less delay-independent H∞ controller for the state delayed system was designed in 1994 [127]. In 1995, the H∞ control with an α-stability constraint

for time-delays systems with LMI approach was presented [128]. The robust controller design method for uncertain systems with time delays using the LMI approach was studied in 1996 [129].

The performance and stability of the systems with time delay were proposed by characteristic equation analysis in 1998 [130]. The delay-dependent and delay-independent robust H∞ control problem for uncertain linear systems with state and input delays were investigated in [131]. Recently, the time delay in active suspensions were also studied intensively [132, 133].

The H∞ control problem can be solved by the algebraic Riccati equation (ARE) approach and the LMI approach, and the computation is also quite easy using the existing software (e.g., Robust Control Toolbox & LMI Control Toolbox in MATLAB). This chapter attempts to apply the existing methods to the active HIS for the vehicle roll control.

7.3 State feedback H∞ controller without time delay

7.3.1 State feedback H∞ controller design with LMI method

The four-DOF vehicle model in Chapter 4 is used for the controller design, where the active suspension system is represented by the control forces, as shown in Figure 4.3. The system equation of the half-car model is modelled as

$$\dot{\mathbf{X}} = \mathbf{A}\mathbf{X} + \mathbf{B}_1\mathbf{w} + \mathbf{B}_2\mathbf{u}, \tag{7.1}$$

where the vehicle state vector $\mathbf{x} = \begin{bmatrix} \theta & z_s & z_{u1} & z_{u2} & \dot{\theta} & \dot{z}_s & \dot{z}_{u1} & \dot{z}_{u2} \end{bmatrix}^T$, road disturbance input vector $\mathbf{w} = \begin{bmatrix} w_1 & w_2 \end{bmatrix}^T$ and control force input vector $\mathbf{u} = \begin{bmatrix} f_1 & f_2 \end{bmatrix}^T$, and the system matrices are defined as

$$\mathbf{A} = \begin{bmatrix} 0 & \mathbf{I} \\ -\mathbf{M}^{-1}\mathbf{K} & -\mathbf{M}^{-1}\mathbf{C} \end{bmatrix}_{8\times 8}, \mathbf{B}_1 = \begin{bmatrix} \mathbf{0} \\ \mathbf{B}_{road} \end{bmatrix}^T_{8\times 2}, \mathbf{B}_2 = \begin{bmatrix} \mathbf{0} \\ \mathbf{B}_{control} \end{bmatrix}^T_{8\times 2},$$

where

$$\mathbf{M} = \begin{bmatrix} I & 0 & 0 & 0 \\ 0 & m_s & 0 & 0 \\ 0 & 0 & m_u & 0 \\ 0 & 0 & 0 & m_u \end{bmatrix} \qquad \mathbf{K} = \begin{bmatrix} 2l^2k_s & 0 & -lk_s & lk_s \\ 0 & 2k_s & -k_s & -k_s \\ -lk_s & -k_s & k_s + k_t & 0 \\ lk_s & -k_s & 0 & k_s + k_t \end{bmatrix}$$

$$\mathbf{C} = \begin{bmatrix} 2l^2c_s & 0 & -lc_s & lc_s \\ 0 & 2c_s & -c_s & -c_s \\ -lc_s & -c_s & c_s & 0 \\ lc_s & -c_s & 0 & c_s \end{bmatrix} \qquad \mathbf{B}_{road} = \begin{bmatrix} 0 & 0 \\ 0 & 0 \\ k_t/m_u & 0 \\ 0 & k_t/m_u \end{bmatrix}_{4\times 2} \qquad \mathbf{B}_{contr} = \begin{bmatrix} l/I & -l/I \\ 1/m & 1/m \\ -1/m_u & 0 \\ 0 & -1/m_u \end{bmatrix}_{4\times 2}$$

The roll angle, left and right suspension deflections are the three control objectives to be minimised in this controller design. It is assumed that the system is described by the block diagram that is shown in Figure 7.1. The corresponding state space formulation for the plant is given by

$$\begin{aligned} &\textit{Plant}: && \dot{\mathbf{x}}(t) = \mathbf{A}\mathbf{x}(t) + \mathbf{B}_1\mathbf{w}(t) + \mathbf{B}_2\mathbf{u}(t) \\ &\textit{Output}: && \mathbf{z}(t) = \mathbf{C}_1\mathbf{x}(t) + \mathbf{D}_{12}\mathbf{u}(t) \\ &\textit{Measurement}: && \mathbf{y}(t) = \mathbf{C}_2\mathbf{x}(t) \end{aligned} \quad , \qquad (7.2)$$

where $\mathbf{x}(t) \in R^n$ is the state, $\mathbf{u}(t) \in R^m$ is the control input, $\mathbf{w}(t) \in R^l$ is the disturbance input, which belongs to $L_2[0,\infty)$, $\mathbf{z}(t) \in R^p$ is the controlled signal output, and the system matrices

$$\mathbf{C}_1 = \begin{bmatrix} 1 & 0 & 0 & 0 & 0 & 0 & 0 & 0 \\ l_1 & 1 & -1 & 0 & 0 & 0 & 0 & 0 \\ -l_2 & 1 & 0 & -1 & 0 & 0 & 0 & 0 \end{bmatrix}, \qquad \mathbf{C}_2 = \mathbf{I}, \qquad \mathbf{D}_{12} = \mathbf{0}.$$

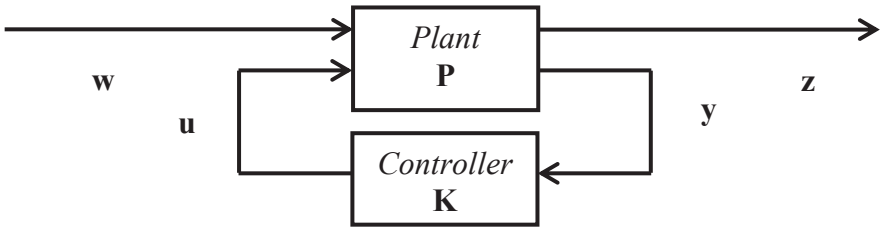

Figure 7.1 Plant with a state feedback controller

For the design of an H∞ controller of the system as per Equation (7.2), this study proposes a continuous time state feedback law

$$\mathbf{u}(t) = \mathbf{K}\mathbf{x}(t), \tag{7.3}$$

where **K** is the state feedback gain matrix to be designed, such that

(1) the closed-loop system is asymptotically stable;

(2) the closed-loop system guarantees, under zero initial condition, $\|\mathbf{z}(t)\|_2 < \gamma \|\mathbf{w}(t)\|_2$ for all non-zero $\mathbf{w}(t) \in L_2[0,\infty)$ and some prescribed constant $\gamma > 0$.

When we apply control (7.3) to the system (7.2), the closed loop system from $\mathbf{w}(t)$ to $\mathbf{z}(t)$ is given by

$$\begin{aligned}\dot{\mathbf{x}}(t) &= \mathbf{A}_K\mathbf{x}(t) + \mathbf{B}_1\mathbf{w}(t) + \mathbf{B}_2\mathbf{u}(t)\\ \mathbf{z}(t) &= \mathbf{C}_K\mathbf{x}(t) + \mathbf{D}_{12}\mathbf{u}(t)\end{aligned}, \tag{7.4}$$

where

$$\begin{aligned}\mathbf{A}_K &= \mathbf{A} + \mathbf{B}_2\mathbf{K}\\ \mathbf{C}_K &= \mathbf{C} + \mathbf{D}_{12}\mathbf{K}\end{aligned}. \tag{7.5}$$

Theorem 1. Consider the hydraulically interconnected suspension system. Given scalar $\gamma > 0$, the closed-loop system is asymptotically stable with H∞ performance index γ, if there exist matrices **Q** > 0, and a matrix **M** satisfying matrix inequality (7.6). Moreover, a desired H∞ state feedback control law is given by

$$\begin{bmatrix} \mathbf{QA}^T + \mathbf{AQ} + \mathbf{M}^T\mathbf{B}_2^T + \mathbf{B}_2\mathbf{M} & \mathbf{B}_1 & \mathbf{QC}^T + \mathbf{M}^T\mathbf{D}_{12}^T \\ * & -\gamma^2\mathbf{I} & \mathbf{D}_{11}^T \\ * & * & -\mathbf{I} \end{bmatrix} < 0. \tag{7.6}$$

Proof 1. Choose the Lyapunov function as

$$V(\mathbf{x}(t)) = \mathbf{x}^T(t)\mathbf{P}\mathbf{x}(t)\cdot \tag{7.7}$$

Taking the derivative of the Lyapunov function (7.7) yields

$$\dot{V}(\mathbf{x}(t)) = \dot{\mathbf{x}}^T(t)\mathbf{P}\mathbf{x}(t) + \mathbf{x}^T(t)\mathbf{P}\dot{\mathbf{x}}(t). \tag{7.8}$$

Then assume the zero initial condition and we introduce

$$J = \int_0^\infty [\mathbf{z}(t)^T\mathbf{z}(t) - \gamma^2\mathbf{w}(t)^T\mathbf{w}(t)]dt. \tag{7.9}$$

Substitute system (7.4) into Equation (7.8), then for any non-zero **w***(t)*

$$J \le \int_0^\infty [\mathbf{z}(t)^T \mathbf{z}(t) - \gamma^2 \mathbf{w}(t)^T \mathbf{w}(t) + \dot{V}(\mathbf{x}(t))]dt = \int_0^\infty \boldsymbol{\eta}^T(t)\boldsymbol{\Pi}\boldsymbol{\eta}(t)dt\,, \qquad (7.10)$$

where

$$\boldsymbol{\eta}(t) = [\mathbf{x}(t) \quad \mathbf{w}(t)]^T,$$

and

$$\boldsymbol{\Pi} = \begin{bmatrix} \mathbf{A}_K{}^T\mathbf{P} + \mathbf{P}\mathbf{A}_K + \mathbf{C}_K^T\mathbf{C}_K & \mathbf{P}\mathbf{B}_1 + \mathbf{C}_K^T\mathbf{D}_{11} \\ * & -\gamma^2\mathbf{I} + \mathbf{D}_{11}{}^T\mathbf{D}_{11} \end{bmatrix} < 0\,.$$

By Schur complement, $\boldsymbol{\Pi} < 0$ is equivalent to

$$\begin{bmatrix} \mathbf{A}_K{}^T\mathbf{P} + \mathbf{P}\mathbf{A}_K & \mathbf{P}\mathbf{B}_1 & \mathbf{C}_K{}^T \\ * & -\gamma^2\mathbf{I} & \mathbf{D}_{11}^T \\ * & * & -\mathbf{I} \end{bmatrix} < 0, \qquad (7.11)$$

and then pre- and post-multiplying by $diag(\mathbf{P}^{-1}\boldsymbol{\Pi})^T$ and its transpose, respectively, gives

$$\begin{bmatrix} \mathbf{P}^{-1}\mathbf{A}_K{}^T + \mathbf{A}_K\mathbf{P}^{-1} & \mathbf{B}_1 & \mathbf{P}^{-1}\mathbf{C}_K{}^T \\ * & -\gamma^2\mathbf{I} & \mathbf{D}_{11}^T \\ * & * & -\mathbf{I} \end{bmatrix} < 0\,. \qquad (7.12)$$

After substituting $\mathbf{Q} = \mathbf{P}^{-1}, \mathbf{M} = \mathbf{K}\mathbf{P}^{-1}$, we can obtain Equation (7.6). Then minimise γ and subject it to LMI (7.6). This problem can be solved very efficiently by means of the MATLAB LMI Toolbox software.

7.3.2 Simulations

In this part, we will validate the state feedback H∞ suspension controller by simulations. The minimisation of γ can be realised as 1. Substituting the half-car model parameters, controller gain matrix can be obtained as

$K = 10^6 \times$ [8.2602 1.2715 -6.7434 5.4673 1.5971 -0.2270 0.0768 -0.0728; -3.2309 0.7256 0.5496 -1.0848 -0.2194 -0.1333 -0.0181 0.0132].

The results of the actively controlled suspension are compared with vehicle response without control. Step road input and fishhook road input are used to stimulate the vehicle roll motion.

7.3.2.1 Step road excitation

Considering the case of step ground disturbance in an otherwise smooth road surface, the corresponding ground displacements of the left and right wheels are 30 mm and -20 mm respectively, as shown in Figure 7.2 (a). The step responses of the open-loop system, namely the original vehicle system without control, and the closed-loop system that is controlled by the state feedback H∞ controller are compared in Figure 7.2 (b) - (d). It can be seen from Figure 7.2 (b) and (c) that the controlled close loop system shows much better step response of the roll angle and left suspension deflection than the original passive vehicle system. The left suspension is compressed by the active suspension to compensate for the vehicle roll caused by the uneven road. As shown in Figure 7.2 (d), the right suspension deflection is not significantly reduced to compress the suspension because the

direction of vehicle roll needs the suspension springs at the right wheel stations to be extended to stabilise the roll motion of the vehicle body.

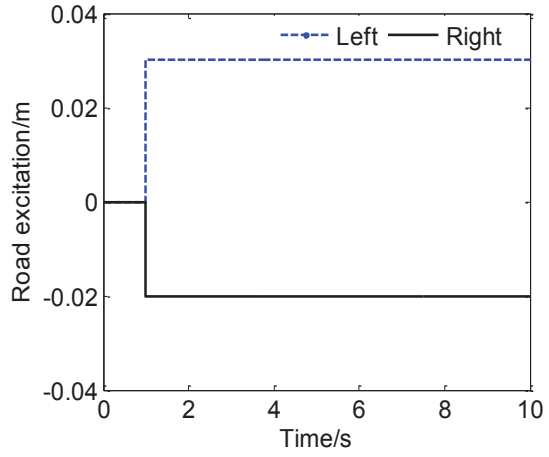

(a) Ground excitation

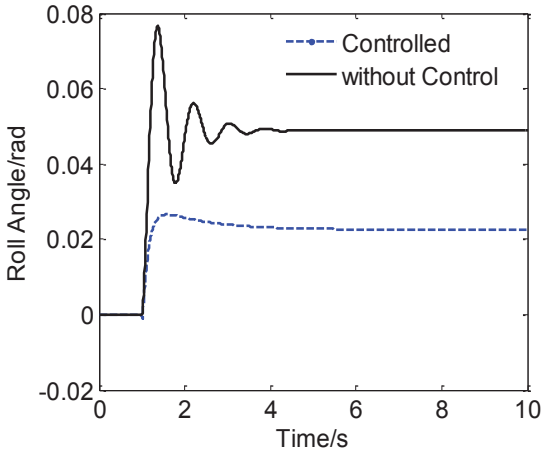

(b) Roll angle

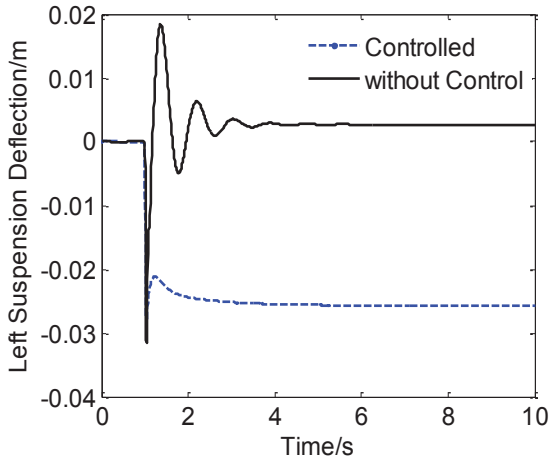

(c) Left suspension deflection

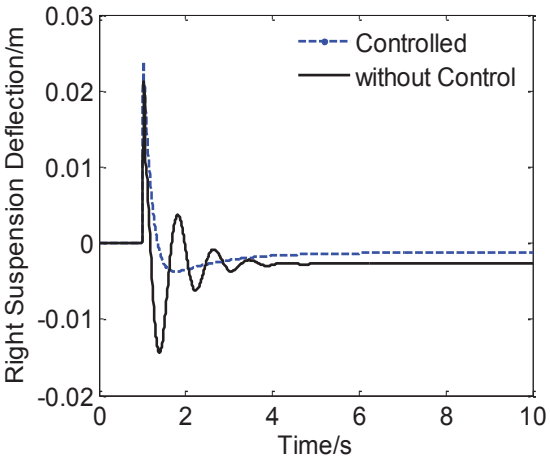

(d) Right suspension deflection

Figure 7.2 Simulation results of step road input

7.3.2.2 Fishhook road excitation

More complex road inputs with fishhook shape surface are considered, as shown in Figure 7.3 (a). The left and right wheel stations undergo a bump and a pothole but with reversed consequence. The out-of-phase road disturbance caused the vehicle roll. Figure 7.3 (b) shows that the vehicle controlled by the obtained H∞ controller also presents superior stability to the vehicle without control under fishhook road excitations, with substantial decreases in the roll angle and overshoot. The simulation results confirmed that good and fast response quantities for roll angle can be guaranteed by the designed H∞ controller.

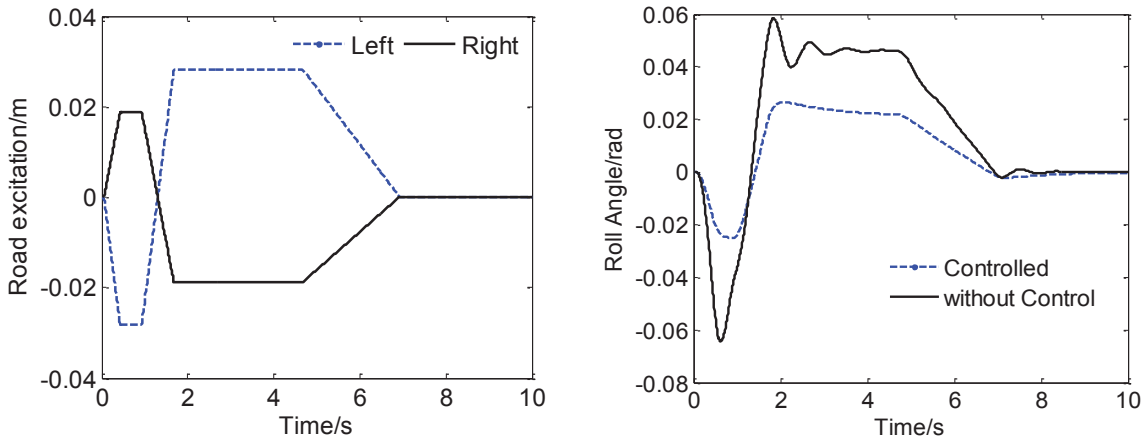

(a) Ground excitation ***(b) Roll angle***

Figure 7.3 Simulation results of fishhook road input

7.4 State feedback H∞ controller with time delay

7.4.1 Delay-dependent State feedback H∞ controller design

Based on the development of the delay-independent state feedback H∞ controller, the delay-dependent state feedback H∞ controller also can be developed through a similar method.

As per Equation (7.1), the system with time delay can be modelled as

$$\dot{\mathbf{x}} = \mathbf{A}\mathbf{x} + \mathbf{B}_1\mathbf{w} + \mathbf{B}_2\mathbf{u}(t-\tau). \tag{7.13}$$

The corresponding state space formulation for the plant is given by

$$\begin{aligned} \dot{\mathbf{x}} &= \mathbf{A}\mathbf{x} + \mathbf{B}_1\mathbf{w} + \mathbf{B}_2\mathbf{u}(t-\tau) \\ \mathbf{z} &= \mathbf{C}_1\mathbf{x} + \mathbf{D}_{12}\mathbf{u}(t-\tau) \\ \mathbf{y}(t) &= \mathbf{C}_2\mathbf{x}(t) \end{aligned} \tag{7.14}$$

As per Equation (7.14), a continuous time state feedback law is proposed as

$$\mathbf{u}(t) = \mathbf{K}\mathbf{x}(t-\tau) \tag{7.15}$$

Theorem 2. Consider the suspension system (7.14). Given scalar $\bar{\tau} > 0$, the closed-loop system of (7.14) is asymptotically stable with H∞ performance index γ for any constant time-delay τ satisfying $\bar{\tau} \geq \tau \geq 0$, if there exist matrices **L** > 0; **R** > 0, **W** > 0 and also **M**, **N**, satisfy matrix inequalities (7.16) and (7.17). Moreover, a desired H∞ state feedback control law is given by $\mathbf{u}(t) = \mathbf{V}\mathbf{L}^{-1}\mathbf{x}(t)$ [132].

$$\begin{bmatrix} \mathbf{L}\mathbf{A}^T + \mathbf{A}\mathbf{L} + \bar{\tau}\mathbf{M} + \mathbf{N} + \mathbf{N}^T + \mathbf{W} & \mathbf{B}_{2V} - \mathbf{N} & \mathbf{B}_1 & \bar{\tau}\mathbf{L}\mathbf{A}^T & \mathbf{L}\mathbf{C}_1^T \\ * & -\mathbf{W} & 0 & \bar{\tau}\mathbf{V}^T\mathbf{B}_2^T & \mathbf{V}^T\mathbf{D}_{12}^T \\ * & * & -\gamma^2\mathbf{I} & \bar{\tau}\mathbf{B}_1^T & 0 \\ * & * & * & -\bar{\tau}\mathbf{R} & 0 \\ * & * & * & * & -\mathbf{I} \end{bmatrix} < 0 \tag{7.16}$$

$$\begin{bmatrix} \mathbf{M} & \mathbf{N} \\ \mathbf{N}^T & \mathbf{L}\mathbf{R}^{-1}\mathbf{L} \end{bmatrix} > 0 \tag{7.17}$$

The reader is referred to the literature [132] for the details of the proof of the Theorem 2. Minimising γ and subjecting it to LMIs (7.16) and (7.17), this H∞ control problem can be solved by the MATLAB LMI Toolbox.

7.4.2 Simulations

The γ can be minimised as 1. Then the controller gain matrix can be obtained in MATLAB:

K =10^4× [1.4466 0.4934 -1.1177 1.4174 0.2160 0.0194 -0.0375 -0.0032; -0.3946 -0.5022 0.5504 0.0025 -0.0604 -0.0715 0.0029 -0.0383].

The obtained delay-dependent state feedback H∞ controller is verified by simulations. The same step road inputs with the previous simulations are adopted and the simulation results with 0 ms and 15 ms time delay are compared with the responses of the original vehicle system with a passive suspension respectively.

7.4.2.1 Step road excitation with $\tau = 0$

The step road excitations that are applied in this simulation are the same as the step input in the simulation of the delay-independent H∞ controller, as shown in Figure 7.2 (a). When there is no system time delay, namely $\tau = 0$, the system response of the passive system and the vehicle controlled by the delay-dependent H∞ controller are plotted in Figure 7.4, where Figure 7.4 (a) shows the step response of the roll angle, Figure 7.4 (b) shows the step response of the suspension deflection at the left wheel station and Figure 7.4 (c) shows the step response of the suspension deflection at the right wheel station. The obtained results demonstrated that the step response of the controlled system is similar to that of the system controlled by the delay-independent H∞ controller. The roll angle is substantially reduced

and the left and right suspension deflections are compressed or extended to tilt the vehicle body back.

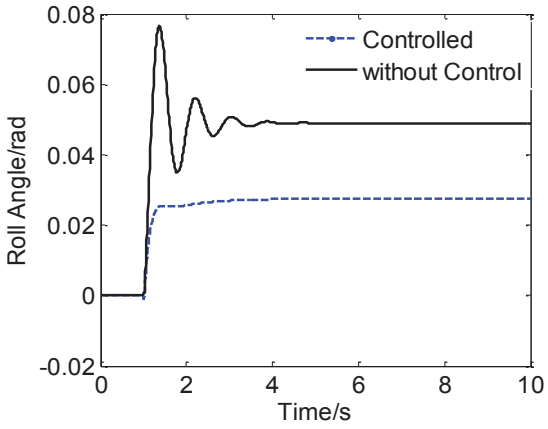

(a) Roll angle

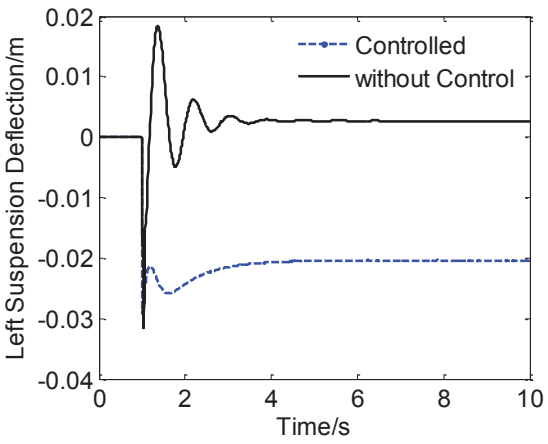

(b) Left suspension deflection

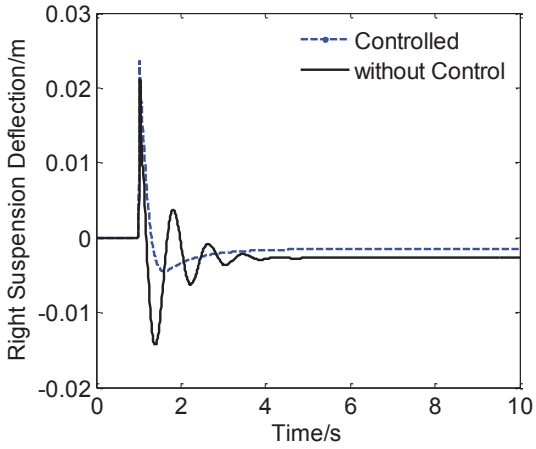

(c) Right suspension deflection

Figure 7.4 Simulation results of 0 ms time delay

7.4.2.2 Step road excitation with $\tau = 15$ ms

In this simulation, a time-delay of 15 ms at the control input is introduced while the system and the road step disturbance remain unchanged. Figure 7.5 (a) - (c) presents the responses

of the roll angles and suspension deflections. The controlled and uncontrolled results are compared in the figures.

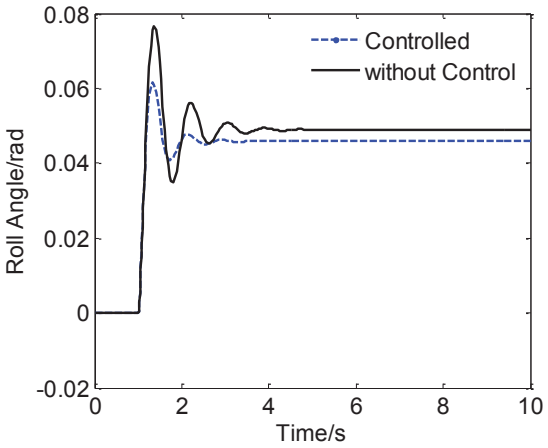

(a) Roll angle

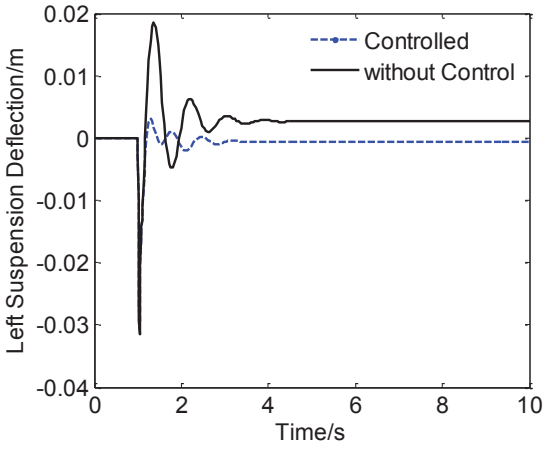

(b) Left suspension deflection

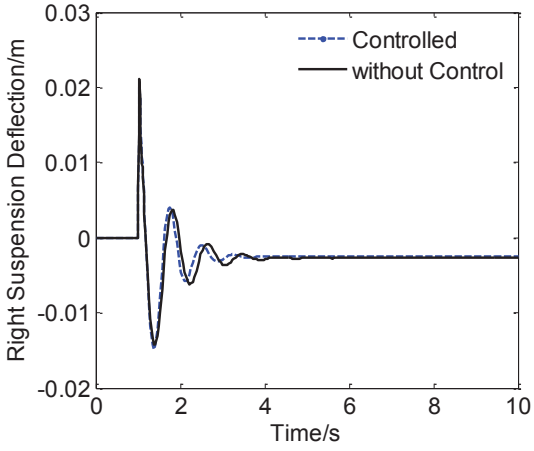

(c) Right suspension deflection

Figure 7.5 Simulation results of 15 ms time delay

It can be seen from Figure 7.5 that the delay-dependent H∞ controller is able to stabilise the closed-loop system. It is confirmed that the obtained controller is of larger tolerance for the

time delay in the control input. Figure 7.5 (a) compares the roll angles of the systems with and without control, wherein we can see the control performance is slightly degraded by the introduced system time delay, but the roll angle is still decreased over 50% than the passive system. The result demonstrates that the designed delay-dependent H∞ controller is still capable of controlling the vehicle roll motion effectively although a relatively large time delay is introduced. Figure 7.5 (b) and (c) provide the comparison of the left suspension deflection and right suspension deflection respectively. We can see that the suspensions are not significantly depressed or extended by the active suspension, which is the reason for the difference between the roll angles with 0 and 15 ms time delay.

7.5 Summary

In this chapter, an attempt was made to reduce the effect of the system time delay on the active suspension control. A delay-independent state feedback H∞ controller and a delay-dependent state feedback H∞ controller were designed for active vehicle suspensions. The formulation of the H∞ problem for the suspension system was solved by the method of matrix inequalities. The delay-dependent H∞ controller design is similar to the design of a delay-independent state feedback H∞ controller, but the time delay needs to be included in the controller development. The step road input and fishhook road input were chosen as road disturbances in the simulations. The results demonstrate that the developed delay-dependent H∞ controller can provide stable and good enough control performance even with actuator time delay to a certain extent in the roll control.

8 Conclusions and Future work

8.1 Summary

This thesis can be summarised as follows.

Chapter 1: the basic problem under investigation was introduced in Chapter 1, and the research objectives were established.

Chapter 2: some essential background information on vehicle suspension systems and control algorithms were provided in Chapter 2. It also revealed some fields about the HIS systems that required further investigation, such as the need to experimentally validate the road holding performance of the HIS.

Chapter 3: this chapter presented an investigation into the road holding ability of a vehicle equipped with the HIS system. The equations of motions of the vehicle-HIS system were derived, through the use of a multi-rigid-body vehicle model. The vehicle dynamic analysis was carried out and it was found that the anti-roll bars stiffen the vehicle warp mode while the HIS does not. Simulations and corresponding experimental verification with different road excitations were then implemented. The test rig and experimental setup were explained and the obtained results were compared. Good agreement was found between the simulations results and the experimental results under low-frequency road excitations. The results demonstrated that when the vehicle underwent off-road driving, the anti-roll bars weakened the road holding ability of the vehicle while the HIS system had a negligible effect.

Chapter 4: the active HIS was experimentally validated in Chapter 4. The hydraulic suspension model was estimated experimentally from the test data. A roll-plane, half-car, linear model was used for developing the H∞ controller. The active suspension model was then integrated with the half car model through their mechanical-hydraulic interface in the cylinders. An H∞ roll control strategy was employed to control the vehicle body's roll motion. The weighting function design of the H∞ control was provided. On the four-post test rig introduced in Chapter 3, the active suspension with H∞ control was validated with several road excitations. The effectiveness of the designed H∞ controller was verified by the test data with a considerable roll angle reduction in the experimental results.

Chapter 5: different categories of control methods were applied in Chapter 5. Fuzzy logic control, fuzzy PID control and LQR theory were adopted to control the vehicle body's roll motion. The system model in Chapter 4 was also used for developing the model-based LQR control. Three controllers were developed and implemented in simulations. A set of road excitations was used to validate designed controllers in simulations. The fuzzy and fuzzy PID controllers were also validated in the experiments. It was found that these three controllers showed their effectiveness in the simulations and experiments with considerable roll angle reductions, and the fuzzy PID controller had a better effect and stability than the other two controllers.

Chapter 6: a more sophisticated mathematical linear model for the active HIS system was developed in Chapter 6. The new active HIS model including the fluid pressure, flow and system damping was integrated with the half-car model. The model parameter tuning was carried out, which resulted in a model that was capable of producing a more accurate

estimation of the system, with significant improvements over the old model in Chapter 4. For verifying the new model, simulations and corresponding experiments were conducted. A high consistency was found between the model and real system responses in the simulations and experiments. Several controllers were applied in the new model and the simulations were conducted. The H∞ controller in Chapter 4 was applied experimentally in the new model and compared with the results of the old model. It was found that the new model was of good value in the simulation study and also had positive effects on the controller design.

Chapter 7: an attempt was made to reduce the influence of the system time delay in Chapter 7. An H∞ state feedback controller was derived. The obtained delay-dependent controller was applied on the half-car model in Chapter 4. It was found that the obtained controller was able to achieve the optimal control performance even with the system time delay to a limited extent.

8.2 Contributions

The specific objectives and contributions of this thesis, as set out in Section 1.2, were achieved as follows.

1. *To review the literature regarding various categories of vehicle suspension systems to show their advantages and disadvantages and the gaps in current knowledge; to introduce the HIS and active HIS.*

   This was achieved by

(a) presenting a detailed summary of past work relating to the suspension systems (Chapter 2)

(b) presenting a brief summary of the control algorithms (Chapter 2)

(c) revealing the areas that need to be further explored (Chapter 2)

(d) introducing the HIS and active HIS schematically (Chapter 2).

2. *To validate that the vehicle with the HIS performs better than the vehicle with anti-roll bars in road holding ability with modal analysis, simulations and experiments.*

   This was achieved by

   (a) using a seven-DOF, full car model and applying Newton's second law to derive the equations of motion (Chapter 3)

   (b) integrating HIS system and anti-roll bars with the vehicle model (Chapter 3)

   (c) carrying out the model analysis and comparing the stiffness change caused by the HIS and anti-roll bars in different motion modes (Chapter 3)

   (d) conducting the tyre load comparison of the three types of vehicle configuration under different road excitations in MATLAB (Chapter 3)

   (e) implementing the tests to verify the modal analysis and simulation results (Chapter 3).

3. *To experimentally validate the feasibility of the proposed novel active HIS at the whole-car level and practically apply different control methods in the active HIS to improve the performance of the roll motion control.*

This was achieved by

(a) using a four-DOF, roll-plane, half-car model and applying Newton's second law to derive the equations of motion (Chapter 4)

(b) using a experimentally estimated active HIS model obtained in previous research and integrating with the half car model (Chapter 4)

(c) designing an output feedback H∞ controller with presenting the weighing function of the H∞ controller (Chapter 4)

(d) conducting the experiment with bumpy ground excitation on the four-post test rig and obtaining feedback signals with LVDT (Chapter 4)

(e) developing the LQR controller with the obtained system model and conducting the simulations of the roll motion control (Chapter 5)

(f) applying the model independent control algorithms, fuzzy control and fuzzy PID control, to the active HIS and implementing the obtained controller in simulations and tests (Chapter 5)

(g) comparing the simulation and experimental results of the LQR, fuzzy and fuzzy PID control (Chapter 5).

4. *To develop a more sophisticated system model including the pressure and flow of the hydraulic system for (1) more accurate description of the whole system of the active HIS equipped vehicle; (2) more reliable simulation study; (3) better anti-roll performance with the model-based control algorithms.*

   This was achieved by

(a) using fluid dynamics and applying Newton's second law to derive the equations of motion of the active HIS (Chapter 6)

(b) integrating the obtained new model with the half-car model (Chapter 6)

(c) tuning the model parameter to produce accurate response (Chapter 6).

5. *To verify the new model and the performance of the controller based on the new model.*

   This was achieved by

   (a) verifying the new model through charging different pressures into the chambers of the hydraulic cylinder in both simulations and experiments and comparing the response (Chapter 6)

   (b) developing and applying model-based controllers in the new model and conducting the simulations (Chapter 6)

   (c) comparing the control performance of the H∞ controller in the old and new models (Chapter 6).

6. *To apply the delay-dependent control algorithm to reduce the effect of the system time delay.*

   This was achieved by

   (a) formulating the H∞ problem for suspension systems (Chapter 7)

   (b) designing a delay-dependent H∞ state feedback controller (Chapter 7)

   (c) applying the controller to the vehicle roll motion control (Chapter 7).

8.3 Suggestions for future work

A number of avenues exist for further research work on the active HIS. Some areas that have arisen during this thesis are as follows.

1. There may be some benefit to retune PID parameters of the fuzzy-PID controller and reconstruct the rule base. To verify the performance, experimentally tuning this controller is also needed. For fuzzy controllers, more inputs are significant to capture the dynamic characteristics of the system fully for improving the performance. Thus, the constructions of the rule base are necessary to be extended. It also could be considered to employ the adaptive T-S Fuzzy, and fuzzy type-II controllers to optimise the control performance. The T-S fuzzy has the capability to address the non-linearities of the system by estimating model's parameters.

2. In the present study, the experimental implementation is constrained by the limited feedback signals. The controllers with one or two feedback signals such as the output feedback H∞ controller and fuzzy controller are implemented in the experiments, but the tests of full state feedback H∞ and LOR controllers, which need the pressure and flow of the fluid system as feedback, have not been conducted. Thus, more feedback signals are required for multi-input controllers. The other method to address this problem is adding a proper state observer or a Kalman filter to the controller.

3. Further verification of the new model of the active HIS is required for the long-term investigation of the system. More experiments for exploring the static and dynamic

characteristics of the active HIS could be implemented so that a large enough database of the empirical data is available when any modification or addition of the model needs to be verified. This database will significantly reduce the time of any changes in the model and tedious lab experiments.

4. The new model of the active HIS could be developed to a full car level. The half car model leads to some errors that the performance of the two cylinders on each side are seen to be better than in the real performance of the active HIS. Hence, the mathematical model is required to be developed to a full-car level with all four actuators. The dynamics of the vehicle can be then explored to a larger extent. Also, a full car model can reveal some hidden problems with the active HIS model or current controllers and provide a more accurate and realistic system model for further work.

5. There is a clear need to further investigate the control of other motion modes or the switched control with more motion modes in the laboratory environment or by road tests. The roll-plane active HIS can evolve to a reconfigurable active HIS with switching control in the roll, bounce and pitch modes. The control strategy and controller design of the switched control (as in Du [134]) are considered theoretically. However, the controller validation and the experimental implementation are worth investigating.

6. A platform to simulate lateral excitations of a vehicle can be developed so that a force to represent the lateral acceleration of the vehicle body caused by sharp turning or cornering can be accurately generated by the test rig. The tests with lateral excitations can be conducted if the lateral excitation is developed.

Appendix A

A.1 State variables and inputs

The state variable of the half-car and DDAS model are given as:

$$\mathbf{x}_{car} = \begin{bmatrix} \theta & Z_s & Z_{u1} & Z_{u2} & \dot{\theta} & \dot{Z}_s & \dot{Z}_{u1} & \dot{Z}_{u2} \end{bmatrix}^T \tag{A.1}$$

$$\mathbf{x}_{HIS} = \begin{bmatrix} P_1 & P_3 & P_5 & P_7 & q_1 & q_3 & q_5 & q_7 & P_2 & P_4 \end{bmatrix}^T \tag{A.2}$$

The state vector of the whole system can be found by combining the state vectors of the half-car model and the HIS model:

$$\mathbf{x}_{system} = \begin{bmatrix} \mathbf{x}_{HIS} \\ \mathbf{x}_{car} \end{bmatrix}_{18\times 1} \tag{A.3}$$

The inputs of the DDAS system and the half-car models are (input of the half-car model is also known as disturbance:

$$\mathbf{u}_{HIS} = \begin{bmatrix} P_{c1} & P_{c2} \end{bmatrix}^T \tag{A.4}$$

$$\mathbf{u}_{car} = \begin{bmatrix} Z_{g1} & Z_{g2} \end{bmatrix}^T \tag{A.5}$$

Similarly to the state vector, the input vector can be assembled by putting the input vectors of both HIS system and half-car as followed.

$$\mathbf{u} = \begin{bmatrix} \mathbf{u}_{HIS} \\ \mathbf{u}_{car} \end{bmatrix}^T \tag{A.6}$$

A.2 Half-car 4-DOF model

Following the obtained state vector, half-car characteristic matrices:

$$\mathbf{M}=\begin{bmatrix} I & 0 & 0 & 0 \\ 0 & m_s & 0 & 0 \\ 0 & 0 & m_u & 0 \\ 0 & 0 & 0 & m_u \end{bmatrix} \qquad \mathbf{C}=\begin{bmatrix} 2l^2c_s & 0 & -lc_s & lc_s \\ 0 & 2c_s & -c_s & -c_s \\ -lc_s & -c_s & c_s & 0 \\ lc_s & -c_s & 0 & c_s \end{bmatrix}$$
$$\mathbf{K}=\begin{bmatrix} 2l^2k_s & 0 & -lk_s & lk_s \\ 0 & 2k_s & -k_s & -k_s \\ -lk_s & -k_s & k_s+k_t & 0 \\ lk_s & -k_s & 0 & k_s+k_t \end{bmatrix} \tag{A.7}$$

The half-car model can be built by this combination of the above matrices as below

$$\mathbf{A}_{car}=\begin{bmatrix} \mathbf{0} & \mathbf{I} \\ -\mathbf{M}^{-1}\mathbf{K} & -\mathbf{M}^{-1}\mathbf{C} \end{bmatrix}_{8\times 8} \tag{A.8}$$

Coupling matrix of half-car model with the HIS system, as derived from equations from section 10.1

$$\mathbf{A}_{car-couple}=\begin{bmatrix} \frac{lA_{pd}}{d} & -\frac{lA_{pd}}{d} & -\frac{lA_{pd}}{d} & \frac{lA_{pd}}{d} \\ -\frac{A_{pd}}{m_s} & \frac{A_{pu}}{m_s} & -\frac{A_{pd}}{m_s} & \frac{A_{pu}}{m_s} \\ \frac{A_{pd}}{m_u} & -\frac{A_{pu}}{m_u} & 0 & 0 \\ 0 & 0 & \frac{A_{pd}}{m_u} & -\frac{A_{pu}}{m_u} \end{bmatrix} \tag{A.9}$$

A.3. HIS system model

Equations of the pressure in actuator chambers shown in section 10.2 can be put down in matrix form as matrix $\mathbf{A}_{piston}$ and $\mathbf{A}_{piston\text{-}couple}$ which respectively represent its behaviour and the chassis's influence on the HIS system itself.

$$\mathbf{A}_{piston} = \begin{bmatrix} 0 & 0 & 0 & 0 & \frac{E}{sA_{pd}} & 0 & 0 & 0 & 0 & 0 \\ 0 & 0 & 0 & 0 & 0 & \frac{E}{sA_{pd}} & 0 & 0 & 0 & 0 \\ 0 & 0 & 0 & 0 & 0 & 0 & \frac{E}{sA_{pd}} & 0 & 0 & 0 \\ 0 & 0 & 0 & 0 & 0 & 0 & 0 & \frac{E}{sA_{pd}} & 0 & 0 \end{bmatrix} \tag{A.10}$$

$$\mathbf{A}_{piston-couple} = \begin{bmatrix} -\frac{El}{s} & \frac{E}{s} & -\frac{E}{s} & 0 \\ \frac{El}{s} & -\frac{E}{s} & \frac{E}{s} & 0 \\ \frac{El}{s} & \frac{E}{s} & 0 & -\frac{E}{s} \\ -\frac{El}{s} & \frac{E}{s} & 0 & \frac{E}{s} \end{bmatrix} \tag{A.11}$$

Similarly, the equations of fluid flow and valve pressure derived in section 10.2 are expressed in matrix form as below.

$$\mathbf{A}_{valve} = \begin{bmatrix} 0 & 0 & 0 & 0 & -\frac{E}{LA_L} & 0 & 0 & -\frac{E}{LA_L} & -\frac{EG}{LA_L} & 0 \\ 0 & 0 & 0 & 0 & 0 & -\frac{E}{LA_L} & -\frac{E}{LA_L} & 0 & 0 & -\frac{EG}{LA_L} \end{bmatrix} \tag{A.12}$$

$$\mathbf{A}_{flow}=\begin{bmatrix} -\frac{1}{L\rho} & 0 & 0 & 0 & -k & 0 & 0 & 0 & \frac{1}{L\rho} & 0 \\ 0 & -\frac{1}{L\rho} & 0 & 0 & 0 & -k & 0 & 0 & 0 & \frac{1}{L\rho} \\ 0 & 0 & -\frac{1}{L\rho} & 0 & 0 & 0 & -k & 0 & 0 & \frac{1}{L\rho} \\ 0 & 0 & 0 & -\frac{1}{L\rho} & 0 & 0 & 0 & -k & \frac{1}{L\rho} & 0 \end{bmatrix} \quad \text{(A.13)}$$

The **A** matrix of the HIS system can be assembled in the following form

$$\mathbf{A}_{HIS}=\begin{bmatrix} \mathbf{A}_{piston} \\ \mathbf{A}_{flow} \\ \mathbf{A}_{valve} \end{bmatrix} \quad \text{(A.14)}$$

According to Equation (6.19), combining the HIS' **A** matrix, the half-car's **A** matrix and coupling matrices, the **A** matrix of the whole system can be obtained as

$$\mathbf{A}=\begin{bmatrix} \mathbf{A}_{HIS} & \mathbf{0} & \mathbf{A}_{piston-couple} \\ \mathbf{0} & \mathbf{0} & \mathbf{0} \\ \mathbf{A}_{car-couple} & \mathbf{0} & \mathbf{A}_{car} \end{bmatrix}_{18\times 18} \quad \text{(A.15)}$$

In accordance to the derived input vector, input matrices **B** of both half-car and HIS models are as followed:

$$\mathbf{B}_{HIS}=\begin{bmatrix} 0 & 0 & 0 & 0 & 0 & 0 & 0 & 0 & \frac{EG}{AL_L} & 0 \\ 0 & 0 & 0 & 0 & 0 & 0 & 0 & 0 & 0 & \frac{EG}{AL_L} \end{bmatrix}^T \quad \text{(A.16)}$$

$$\mathbf{B}_{car} = \begin{bmatrix} 0 & 0 & 0 & 0 & 0 & 0 & 0 & 0 & \dfrac{k_t}{m_u} & 0 \\ 0 & 0 & 0 & 0 & 0 & 0 & 0 & 0 & 0 & \dfrac{k_t}{m_u} \end{bmatrix}^T \tag{A.17}$$

Combining the above **B** matrices yields the input matrix of the whole system, given as

$$\mathbf{B} = \begin{bmatrix} \mathbf{B}_{HIS} & \mathbf{0} \\ \mathbf{0} & \mathbf{B}_{car} \end{bmatrix}_{18\times 4} \tag{A.18}$$

The system's model is completed upon assembling all matrices together as followed.

$$\dot{\mathbf{x}} = \mathbf{A}\mathbf{x} + \mathbf{B}\mathbf{u} \tag{A.19}$$

$$\begin{bmatrix} \dot{\mathbf{x}}_{HIS} \\ \dot{\mathbf{x}}_{car} \end{bmatrix} = \begin{bmatrix} \mathbf{A}_{HIS} & 0 & \mathbf{A}_{piston-couple} \\ 0 & 0 & 0 \\ \mathbf{A}_{car-couple} & 0 & \mathbf{A}_{car} \end{bmatrix}_{18\times 18} \begin{bmatrix} \mathbf{x}_{HIS} \\ \mathbf{x}_{car} \end{bmatrix} + \begin{bmatrix} \mathbf{B}_{HIS} & \mathbf{0} \\ \mathbf{0} & \mathbf{B}_{car} \end{bmatrix} \begin{bmatrix} \mathbf{u}_{HIS} \\ \mathbf{u}_{car} \end{bmatrix} \tag{A.20}$$

References

[1] National Highway Traffic Safety Administration, "Initiative to address the mitigation of vehicle rollover " Docket No. NHTSA-2003-14622-1, 2003.

[2] Young, D., Grzebieta, R., McIntosh, A., Bambach, M., et al., "Diving versus roof intrusion: a review of rollover injury causation," International Journal of Crashworthiness **12**(6): 609-628, 2007.

[3] Yamashita, M., Fujimori, K., Hayakawa, K., and Kimura, H., "Application of H< sub>∞</sub> control to active suspension systems," Automatica **30**(11): 1717-1729, 1994.

[4] Smith, M. and Walker, G., "Interconnected vehicle suspension," Proceedings of the Institution of Mechanical Engineers, Part D: Journal of Automobile Engineering **219**(3): 295-307, 2005.

[5] Yokoya, Y., Kizu, R., Kawaguchi, H., Ohashi, K., et al., "Integrated control system between active control suspension and four wheel steering for the 1989 Celica," SAE paper **901748**, 1990.

[6] Lijima, T., Akatsu, Y., Takahashi, K., and Murakami, H., "Development of a Hydraulic Active Suspension," SAE TECHNICAL PAPER SERIES, 1993.

[7] Zhang, N., *Active Suspension*, 2008: Australian Patent PCT/Au2008-000720.

[8] Eckermann, E., "World history of the automobile," Training **2012**: 11-19, 2001.

[9] Cao, D., Song, X., and Ahmadian, M., "Editors' perspectives: road vehicle suspension design,dynamics, and control," Vehicle System Dynamics **49**(1–2): 3–28, 2011.

[10] Zhang, N., Smith, W.A., and Jeyakumaran, J., "Hydraulically interconnected vehicle suspension: background and modelling," Vehicle System Dynamics: International Journal of Vehicle Mechanics and Mobility **48**(1): 17-40, 2010.

[11] Sharp, R.S. and Crolla, D.A., "Road Vehicle Suspension System Design - a review," Vehicle System Dynamics: International Journal of Vehicle Mechanics and Mobility **16**(3): 167 - 192, 1987.

[12] Mcelroy, J.J., *AIR-SPRINGS AND THE MEASUREMENT OF RIDING-QUALITY*, 1924, SAE Technical Paper.

[13] Warner, J.A., *Riding-qualities research*, 1924, SAE Technical Paper.

[14] Winkelmann, O., *Handling requirements*, 1961, SAE Technical Paper.

[15] Dillman, O. and Collier, E., *Building stability into the modern automobile*, 1953, SAE Technical Paper.

[16] Smith, W., *An investigation into the dynamics of vehicles with hydraulically interconnected suspensions*, 2009, University of Technology, Sydney.

[17] Smith, W.A. and Zhang, N., "Recent developments in passive interconnected vehicle suspension," Frontiers of Mechanical Engineering in China **5**(1): 1-18, 2010.

[18] Hawley, J.B., *Shock Absorber and the Like For Vehicles*, 1927: US

[19] Pevsner, J.M., "Equalizing types of suspension," Automobile Eng. : 10-16, 1957.

[20] Moulton, A. and Best, A. "Rubber springs and inter-connected suspension systems." Proceedings of Engineering Design Show Conference. 1970.

[21] Moulton, A. and Best, A., *Hydragas suspension*, 1979.

[22] Liu, P., Rakheja, S., and Ahmed, A.K.W., "Properties of an Interconnected Hydro-Pneumatic Suspension System," TRANSACTIONS- CANADIAN SOCIETY FOR MECHANICAL ENGINEERING **19**(4): 383-396, 1995.

[23] Liu, P., Rakheja, S., and Ahmed, A. "An analytical study of an interconnected vehicle suspension." ASME International Mechanical Engineering Congress and Exposition. San Francisco. 1995.

[24] Wilde, J.R., Heydinger, G.J., Guenther, D.A., Mallin, T., et al., "Experimental evaluation of fishhook maneuver performance of a kinetic suspension system," SAE paper 2005-01-0392, , 2005.

[25] Fontdecaba, J., "Integral suspension system for motor vehicles based on passive component," SAE Technical Paper Series **2002-01-3105**, 2002.

[26] Ortiz, M., "Principles of interconnected suspensions," RaceCar Engineering **7**(7-8), 1997.

[27] Zapletal, E., *Balanced suspension*, 2000, SAE Technical Paper.

[28] Zapletal, E., "Balanced Suspension," SAE paper 2000-01-3572, 2000.

[29] Mavroudakis, B. and Eberhard, P. "Mode decoupling in vehicle suspensions applied to race cars." III European Conference on Computational Mechanics: Solids, Structures and Coupled Problems in Engineering. Lisbon. 2006.

[30] Cao, D., Rakheja, S., and Su, C.-Y., "Comparison of roll properties of hydraulically and pneumatically interconnected suspensions for heavy vehicles," SAE paper 2005-01-3593, 2005.

[31] Cao, D., Rakheja, S., and Su, C.-Y., "A Generalized Model of a Class of Interconnected Hydro-Pneumatic Suspensions and Analysis of Pitch Properties," ASME Conference Proceedings **2006**(47675): 137-146, 2006.

[32] Cao, D., Rakheja, S., and Su, C.-Y., "Pitch attitude control and braking performance analysis of heavy vehicles with interconnected suspensions, ," SAE J. Commercial Veh. **116 (2)** 119–127, 2007.

[33] Cao, D., Rakheja, S., and Su, C.Y., "Pitch plane analysis of a twin-gas-chamber strut suspension," Proceedings of the Institution of Mechanical Engineers, Part D: Journal of Automobile Engineering **222**(8): 1313-1335, 2008.

[34] Cao, D., Rakheja, S., and Su, C.-Y., *Property analysis of an X-coupled suspension for sport utility vehicles*, 2008, SAE Technical Paper.

[35] Cao, D., Rakheja, S., and Su, C.-Y., "Roll- and pitch-plane-coupled hydro-pneumatic suspension. Part 2: dynamic response analyses," Vehicle System Dynamics: International Journal of Vehicle Mechanics and Mobility **48**(4): 507 - 528, 2010.

[36] Cao, D., Rakheja, S., and Su, C.Y., "Dynamic analyses of heavy vehicle with pitch-interconnected suspensions," International Journal of Heavy Vehicle Systems **15**(2-4): 272-308, 2008.

[37] Wilde, J.R., Heydinger, G.J., and Guenther, D.A., "ADAMS simulation of ride and handling performance of kinetic suspension system," SAE paper 2006-01-1972, , 2006.

[38] Garrott, W.R., Howe, J.G., and Forkenbrock, G., *Results from NHTSA's experimental examination of selected maneuvers that may induce on-road untripped, light vehicle rollover*, 2001, SAE Technical Paper.

[39] Forkenbrock, G.J., Garrott, W.R., Heitz, M., and O'Harra, B.C., *An experimental examination of J-turn and fishhook maneuvers that may induce on-road, untripped, light vehicle rollover*, 2003, SAE Technical Paper.

[40] Smith, W.A., Zhang, N., and Hu, W., "Hydraulically interconnected vehicle suspension: handling performance," Vehicle System Dynamics: International Journal of Vehicle Mechanics and Mobility, 2010.

[41] Smith, W.A., Zhang, N., and Jeyakumaran, J., "Hydraulically interconnected vehicle suspension: theoretical and experimental ride analysis," Vehicle System Dynamics: International Journal of Vehicle Mechanics and Mobility **48**(1): 41-64, 2010.

[42] Wang, L., Zhang, N., and Du, H., "Experimental Investigation of a Hydraulically Interconnected Suspension in Vehicle Dynamics and Stability Control," SAE International Journal of Passenger Cars- Mechanical Systems **5** (2): 759-768, 2012.

[43] Crosby, M. and Karnopp, D.C., "The active damper—a new concept for shock and vibration control," Shock and Vibration Bulletin **43**(4): 119-133, 1973.

[44] Crosby, M. and Karnopp, D., *System for controlling the transmission of energy between spaced members*, 1974, Google Patents.

[45] Elbeheiry, E.M., Karnopp, D.C., Elaraby, M.E., and Abdelraaouf, A.M., "Advanced Ground Vehicle Suspension Systems - A Classified Bibliography," Vehicle System Dynamics: International Journal of Vehicle Mechanics and Mobility **24**(3): 231 - 258, 1995.

[46] Ivers, D.E. and Miller, L.R., "Semi-active suspension technology. An evolutionary view," ASME, NEW YORK, NY,(USA). **40**: 327-346, 1991.

[47] AHMADIAN, #160, Mehdi, SIMON, et al., "Can semiactive dampers with skyhook control improve roll stability of passenger vehicles?," 2004, New York, NY, ETATS-UNIS: Society of Automotive Engineers. 6.

[48] Hrovat, D., "Survey of Advanced Suspension Developments and Related Optimal Control Applications," Automatica **33**(10): 1781-1817, 1997.

[49] Morman, K. and Giannopoulos, F., "Recent advances in the analytical and computational aspects of modeling active and passive vehicle suspensions," Computational Methods in Ground Transportation Vehicles **50**: 75-1, 1982.

[50] Bender, E., Paul, I., and Karnopp, D., "On the optimization of vehicle suspensions using random process theory," 1967.

[51] Karnopp, D.C. and Trikha, A.K., "Comparative study of optimization techniques for shock and vibration isolation," Journal of Engineering for Industry **91**: 1128, 1969.

[52] Healey, A. "Digital processing of measured vibration data for automobile ride evaluation." ASME AMD V24 1977: Passenger Vibration in Transportation Vehicles, presented at Design Eng Conf, Chicago, Illinois, September 26-28, 1977. 1977.

[53] Barak, P., "On a ride control algorithm for heave, pitch and roll motions of a motor vehicle," 1985.

[54] Chalasani, R., "Ride performance potential of active suspension system—Part II: comprehensive analysis based on a full-car model," ASME Monograph: 205-234, 1986.

[55] Barak, P. and Hrovat, D. "Application of the LQG approach to design of an automotive suspension for three dimensional vehicle models." Proc. Int. Conf. on Advanced Suspensions. 1988.

[56] Williams, R.A., "Automotive active suspensions - Part 1: basic principles," Proceedings of the Institution of Mechanical Engineers Part D-Journal of Automobile Engineering **211**(6): 415-426, 1997.

[57] Williams, R.A., "Automotive active suspensions Part 2: Practical considerations," Proceedings of the Institution of Mechanical Engineers Part D-Journal of Automobile Engineering **211**(6): 427-444, 1997.

[58] Sharp, R.S. and Peng, H., "Vehicle dynamics applications of optimal control theory," Vehicle System Dynamics **49**(7): 1073-1111, 2011.

[59] Bose, "Bose suspension system," **2013**(20 March): http://worldwide.bose.com/axa/en_au/web/suspension_system/page.html,

[60] Prokop, G. and Sharp, R.S., "Performance Enhancement of Limited-Bandwidth Active Automotive Suspensions by Road Preview," Iee Proceedings-Control Theory and Applications **142**(2): 140-148, 1995.

[61] Koch, G., Fritsch, O., and Lohmann, B., "Potential of low bandwidth active suspension control with continuously variable damper," Control Engineering Practice **18**(11): 1251-1262, 2010.

[62] Ei-Demerdash, S.M. and Crolla, D.A., "Hydro-pneumatic Slow-active Suspension with Preview Control," Vehicle System Dynamics: International Journal of Vehicle Mechanics and Mobility **25**(5): 369 - 386, 1996.

[63] Pilbeam, C. and Sharp, R.S., "Performance Potential and Power Consumption of Slow-Active Suspension Systems with Preview," Vehicle System Dynamics: International Journal of Vehicle Mechanics and Mobility **25**(3): 169 - 183, 1996.

[64] Rosam, N. and Darling, J., "Development and simulation of a novel roll control system for the Interconnected Hydragas(R) suspension," Vehicle System Dynamics **27**(1): 1-18, 1997.

[65] Wang, L., Zhang, N., and Du, H., *Design and Experimental Investigation of Demand Dependent Active Suspension for Vehicle Rollover Control*, in *48th IEEE Conference on Decision and Control*2009: Shanghai, P.R. China, .

[66] Lovins, A.B. and Cramer, D.R., "Hypercars((R)), hydrogen, and the automotive transition," International Journal of Vehicle Design **35**(1-2): 50-85, 2004.

[67] Docquier, N., Poncelet, A., Delannoy, M., and Fisette, P., "Multiphysics modelling of multibody systems: application to car semi-active suspensions," Vehicle System Dynamics: International Journal of Vehicle Mechanics and Mobility **48**(12): 1439 - 1460, 2010.

[68] Newton, B., "New Nissan Patrol bigger, more luxurious," **2010**(5 April): http://smh.drive.com.au/motor-news/nes-nissan-patrol-bigger-more-luxurious-20100215-nzwt.html,

[69] Rosam, N. and Darling, J., "Development and Simulation of a Novel Roll Control System for the Interconnected Hydragas® Suspension," Vehicle System Dynamics: International Journal of Vehicle Mechanics and Mobility **27**(1): 1 - 18, 1997.

[70] Rideout, G. and Anderson, R.J., *Experimental testing and mathematical modeling of the interconnected hydragas suspension system*, 2003, SAE Technical Paper.

[71] Tanahashi, H., Shindo, K., Nogami, T., and Oonuma, T., *Toyota electronic modulated air suspension for the 1986 Soarer*, 1987, SAE Technical Paper.

[72] Audi, "Audi Glossary-Dynamic Ride Control (DRC)," **2013**: http://www.audiusa.com/us/brand/ec/tools/advice/glossary/dynamic_ride_control.browser.html,

[73] Sampson, D.J.M., McKevitt, G., and Cebon, D., "The development of an active roll control system for heavy vehicles," Vehicle System Dynamics **33**: 704-715, 1999.

[74] Sampson, D.J.M. and Cebon, D., "Active roll control of single unit heavy road vehicles," Vehicle System Dynamics **40**(4): 229-270, 2003.

[75] Lin, R.C., Cebon, D., and Cole, D.J., "An Investigation of Active Roll Control of Heavy Road Vehicles," Vehicle System Dynamics **23**: 308-321, 1994.

[76] Miege, A.J.P. and Cebon, D., "Optimal roll control of an articulated vehicle: theory and model validation," Vehicle System Dynamics **43**(12): 867-893, 2005.

[77] Stone, E.J. and Cebon, D., "Control of semi-active anti-roll systems on heavy vehicles," Vehicle System Dynamics **48**(10): 1215-1243, 2010.

[78] Ahmad, F.b., Hudha, K., and Jamaluddin, H., "Gain scheduling PID control with pitch moment rejection for reducing vehicle dive and squat," International journal of vehicle safety **4**(1): 45-83, 2009.

[79] Shun, L., "an, Yu Xian-li, Yao Yong-ming, et al. Vehi-cle optimization-intelligence integrated control active suspension system based on pitch angle optimization," Journal of Jilin University (Engineering and Technology Edition) **40**(Sup 1): 17-23, 2010.

[80] Bennett, S., "A brief history of automatic control," IEEE Control Systems Magazine **16**(3): 17-25, 1996.

[81] Minorsky, N., "Directional stability of automatically steered bodies," Journal of ASNE **42**(2): 280-309, 1922.

[82] Nyquist, H., "Regeneration theory," Bell system technical journal **11**(1): 126-147, 1932.

[83] Athans, M. and Kendrick, D., "Control theory and economics: A survey, forecast, and speculations," Automatic Control, IEEE Transactions on **19**(5): 518-524, 1974.

[84] Kalman, R., "On the general theory of control systems," IRE Transactions on Automatic Control **4**(3): 110-110, 1959.

[85] Åström, K.J. and Eykhoff, P., "System identification—a survey," Automatica **7**(2): 123-162, 1971.

[86] Astrom, K.J., "Adaptive control around 1960," Control Systems, IEEE **16**(3): 44-49, 1996.

[87] Bryson Jr, E., "Optimal control-1950 to 1985," Control Systems, IEEE **16**(3): 26-33, 1996.

[88] Waltz, M. and Fu, K., "A heuristic approach to reinforcement learning control systems," Automatic Control, IEEE Transactions on **10**(4): 390-398, 1965.

[89] Fu, K.S. and McMurtry, G.J., "A study of stochastic automata as models of adaptive and learning controllers," 1965: Purdue University School of Electrical Engineering.

[90] Fu, K.S. and McLaren, R.W., "An application of stochastic automata to the synthesis of learning systems," 1965: School of Electrical Engineering, Purdue University.

[91] Zadeh, L.A., "Fuzzy sets," Information and control **8**(3): 338-353, 1965.

[92] Precup, R.-E. and Hellendoorn, H., "A survey on industrial applications of fuzzy control," Computers in Industry **62**(3): 213-226, 2011.

[93] Thompson, A., "Design of active suspensions," Proceedings of the Institution of Mechanical Engineers **185**(1): 553-563, 1970.

[94] Yoshimura, T., Nakaminami, K., Kurimoto, M., and Hino, J., "Active suspension of passenger cars using linear and fuzzy-logic controls," Control Engineering Practice **7**(1): 41-47, 1999.

[95] Al-Holou, N., Lahdhiri, T., Joo, D.S., Weaver, J., et al., "Sliding mode neural network inference fuzzy logic control for active suspension systems," Fuzzy Systems, IEEE Transactions on **10**(2): 234-246, 2002.

[96] Taghirad, H.D. and Esmailzadeh, E., "Automobile passenger comfort assured through LQG/LQR active suspension," Journal of vibration and control **4**(5): 603-618, 1998.

[97] Kruczek, A. and Stribrsky, A. "H∞ Control of Automotive Active Suspension with Linear Motor." Proccedings of the 3rd IFAC Symposium on Mechatronic Systems. 2004.

[98] Gordon, T., Marsh, C., and Wu, Q., "Stochastic optimal control of active vehicle suspensions using learning automata," Proceedings of the Institution of Mechanical Engineers, Part I: Journal of Systems and Control Engineering **207**(3): 143-152, 1993.

[99] Lin, J.S. and Kanellakopoulos, I., "Nonlinear design of active suspensions," Control Systems, IEEE **17**(3): 45-59, 1997.

[100] Hac, A. "Optimal linear preview control of active vehicle suspension." Decision and Control, 1990., Proceedings of the 29th IEEE Conference on. 1990.

[101] Poussot-Vassal, C., Spelta, C., Sename, O., Savaresi, S.M., et al., "Survey and performance evaluation on some automotive semi-active suspension control methods: A comparative study on a single-corner model," Annual Reviews in Control **36**(1): 148-160, 2012.

[102] Karnopp, D., Crosby, M.J., and Harwood, R., "Vibration control using semi-active force generators," Journal of Manufacturing Science and Engineering **96**(2): 619-626, 1974.

[103] Koo, J.-H., Ahmadian, M., Setareh, M., and Murray, T., "In search of suitable control methods for semi-active tuned vibration absorbers," Journal of vibration and control **10**(2): 163-174, 2004.

[104] Simon, D.E. and Ahmadian, M., "On the Design of an Intelligent Suspension for Controlling Passenger Vehicle Roll Stability," ASME Conference Proceedings **2002**(36290): 263-272, 2002.

[105] Anderson, B.D. and Moore, J.B., "Optimal control: linear quadratic methods." Vol. 1. 1990: Prentice Hall Englewood Cliffs, NJ.

[106] Yamashita, M., Fujimori, K., Uhlik, C., Kawatani, R., et al. "< e1> H</e1>< sub>∞</sub> control of an automotive active suspension." Decision and Control, 1990., Proceedings of the 29th IEEE Conference on. 1990.

[107] Lauwerys, C., Swevers, J., and Sas, P., "Robust linear control of an active suspension on a quarter car test-rig," Control Engineering Practice **13**(5): 577-586, 2005.

[108] Du, H. and Zhang, N., "Constrained H∞ control of active suspension for a half-car model with a time delay in control," Proceedings of the Institution of Mechanical Engineers, Part D: Journal of Automobile Engineering **222**(5): 665-684, 2008.

[109] Hayakawa, K., Matsumoto, K., Yamashita, M., Suzuki, Y., et al., "Robust H< sup>∞</sup>-output feedback control of decoupled automobile active suspension systems," Automatic Control, IEEE Transactions on **44**(2): 392-396, 1999.

[110] Wang, J., Wilson, D.A., Xu, W., and Crolla, D.A. "Active Suspension Control to Improve Vehicl0e Ride and Steady-State Handling." Decision and Control, 2005 and 2005 European Control Conference. CDC-ECC'05. 44th IEEE Conference on. 2005.

[111] Xu, G., Zhang, N., and Roser, H.M., "Roll and pitch independently tuned interconnected suspension: modelling and dynamic analysis," Vehicle System Dynamics: 1-20, 2015.

[112] Davis, R.I. and Patil, P.B., *Electrically powered active suspension for a vehicle*, 1991, Google Patents.

[113] Raidel, J.E., *Air spring suspension system with parallelogram stabilized axle and anti-roll control*, 1982, Google Patents.

[114] Pascarella, R.J., *Controlled stabilizer bar attachment apparatus for improved suspension articulation*, 1996, Google Patents.

[115] Wang, L., Xu, G., Zhang, N., and Roser, H., *Experimental Comparison of Anti-Roll Bar with Hydraulically Interconnected Suspension in Articulation Mode*, 2013, SAE Technical Paper.

[116] Rauh, J. and Ammon, D., "System dynamics of electrified vehicles: some facts, thoughts, and challenges," Vehicle System Dynamics **49**(7): 1005-1020, 2011.

[117] Ferreira1, J.A., Almeida, F.G.d., and Quintas, M.R., "Semi-empirical model for a hydraulic servo-solenoid valve," Proceedings of the Institution of Mechanical Engineers, Part I: Journal of Systems and Control Engineering, 2002.

[118] Zhang, N., Wang, L., and Du, H., *Modeling of a New Active Suspension for Roll Control*, in *13th Asia Pacific Vibration Conference*2009: University of Canterbury, New Zealand.

[119] Doyle, J.C., Wall, J.E., and Stein, G. "Performance and robustness analysis for structured uncertainty." Decision and Control, 1982 21st IEEE Conference on. 1982.

[120] Heiing, B. and Heißing, B., "Chassis Handbook: Fundamentals, Driving Dynamics, Components, Mechatronics, Perspectives," 2011: Vieweg+Teubner.

[121] Motor Trend, "The Bose Electronic Suspension, now in prototype testing, is stunning and simple," http://www.motortrend.com/features/editorial/112_0501_ bosesuspension/viewall.html, January.2005.

[122] Du, H. and Zhang, N. "Fuzzy control for nonlinear uncertain electrohydraulic active suspensions with input constraint." IEEE transactions on fuzzy systems. 2009.

[123] Chen, H.Y. and Huang, S.J., "Model-free adaptive sliding controller for automotive active suspensions," Journal of the Chinese Society of Mechanical Engineers **29**(1): 21-26, 2008.

[124] Doyle, J.C., Glover, K., Khargonekar, P.P., and Francis, B., "State-space solutions to standard H 2 and H∞ control problems," Automatic Control, IEEE Transactions on **34**(8): 831-847, 1989.

[125] Gahinet, P., "Explicit controller formulas for LMI-based H∞ synthesis," Automatica **32**(7): 1007-1014, 1996.

[126] Gahinet, P., Nemirovskii, A., Laub, A.J., and Chilali, M., "The LMI Control Toolbox User's Guide," 1995.

[127] Lee, J.H., Kim, S.W., and Kwon, W.H., "Memoryless H∞ controllers for state delayed systems," IEEE Transactions on Automatic Control **39**(1): 159-162, 1994.

[128] Niculescu, S.-I., "H∞ memoryless control with an α-stability constraint for time-delay systems: an LMI approach," Automatic Control, IEEE Transactions on **43**(5): 739-743, 1998.

[129] Jeung, E.T., Kim, J.H., and Park, H.B., "Robust controller design for uncertain systems with time delays: LMI approach," Automatica **32**(8): 1229-1231, 1996.

[130] Hu, H., Dowell, E., and Virgin, L., "Stability estimation of high dimensional vibrating systems under state delay feedback control," Journal of Sound and Vibration **214**(3): 497-511, 1998.

[131] Li, H., Niculescu, S.-I., Dugard, L., and Dion, J.-M. "Robust ℋ∞ control of uncertain linear time-delay systems: a linear matrix inequality approach. I." Decision and Control, 1996., Proceedings of the 35th IEEE Conference on. 1996.

[132] Du, H. and Zhang, N., "H[infinity] control of active vehicle suspensions with actuator time delay," JOURNAL OF SOUND AND VIBRATION **301**(1-2): 236-252, 2007.

[133] Vahidi, A. and Eskandarian, A., "Predictive time-delay control of vehicle suspensions," Journal of vibration and control **7**(8): 1195-1211, 2001.

[134] Du, H., Zhang, N., and Wang, L., "Switched Control of Vehicle Suspension Based on Motion-Mode Detection," 2012.